UNIVERSITY OF BELGRADE
FACULTY OF PHYSICS

Srdjan Stavrić

FIRST-PRINCIPLES STUDY OF THE STRUCTURAL AND ELECTRONIC PROPERTIES OF METALS ADSORBED ON TWO-DIMENSIONAL MATERIALS

Doctoral Dissertation

Belgrade, 2019.

UNIVERZITET U BEOGRADU
FIZIČKI FAKULTET

Srđan Stavrić

AB-INITIO ISTRAŽIVANJE STRUKTURNIH I ELEKTRONSKIH OSOBINA METALA ADSORBOVANIH NA DVODIMENZIONALNIM MATERIJALIMA

doktorska disertacija

Beograd, 2019.

Mentor: dr Željko Šljivančanin, naučni savetnik
Instituta za nuklearne nauke "Vinča"

Članovi komisije: dr Tatjana Vuković, vanredni profesor

Fizičkog fakulteta Univerziteta u Beogradu

dr Ivanka Milošević, redovni profesor

Fizičkog fakulteta Univerziteta u Beogradu

dr Željko Šljivančanin, naučni savetnik

Instituta za nuklearne nauke "Vinča"

Datum odbrane: _____

Zahvalnica

Doktorska teza koja je pred vama izrađena je u Laboratoriji za teorijsku fiziku i fiziku kondenzovane materije Instituta za nuklearne nauke "Vinča". Ovom prilikom želim da ukažem na one bez čije pomoći ovaj rad ne bi ugledao svetlost dana. Hronološki, najpre zahvaljujem profesorima Bogosavu Ristiću i Mladenu Šljivoviću – prvom jer sam uz njegovu pomoć načinio prve fizičarske korake a drugom jer me je na put fizike vratio u vreme lutanja, kada se po mojoj glavi motala opskurna ideja da postanem inženjer. Zatim zahvaljujem svom mentoru dr Željku Šljivančaninu, koji je od jednog studenta napravio istraživača, kao i dragom kolegi dr Zoranu S. Popoviću jer mi je svojim sugestijama često ukazivao da fizika ume da iznedri sasvim drugačije rezultate od onih koje očekujemo, nedopuštajući da me lažni optimizam ikada zavara. Na kraju zahvalnost dugujem mom prijatelju Đorđu Rakiću, koji je pročitao i ispravio veliki deo ovog rukopisa demonstrirajući da nije zalud toliko vreme proveo na Redditu. Sve greške i pogreške na koje ćete (vrlo verovatno) naići tokom čitanja ovog štiva, kako pravopisne i gramatičke tako i one koje se tiču fizike, isključivo su moja zasluga.

Ab initio istraživanje strukturnih i elektronskih osobina metala adsorbovanih na dvodimenzionalnim materijalima

SAŽETAK

Tokom poslednjih petnaest godina, svedoci smo izuzetnih istraživačkih napora usmerenih ka primeni neobičnih osobina dvodimenzionalnih (2D) materijala u razvoju naredne generacije nanoelektronskih komponenti. Napredak ovih tehnologija počiva na sveobuhvatnom razumevanju osnovnih fizičkih mehanizama koji određuju efikasnost napravljenih uređaja u kojima su spojevi između metala i 2D materiajala nezaobilazni. U ovoj tezi smo istraživali adsorpciju metala na novoj klasi 2D materijala koristeći metod zasnovan na osnovnim principima kvantne mehanike, sa posebnim naglaskom na strukturnim i elektronskim osobinama obrazovanih nanostruktura. Primenjeni numerički metod temelji se na teoriji funkcionala gustine (*density functional theory* – DFT), koja omogućava izračunavanje fižickih osobina atoma, molekula i kristala koristeći elektronsku gustinu.

Odabravši litijum, kalcijum i titanijum kao predstavnike različitih klasa metala, ispitivali smo njihovu adsorpciju na grafenu. Morfologija rasta adsorbovanih metala suštinski zavisi od prirode međusobne interakcije adsorbata. Izrazito privlačna interakcija dovodi do obrazovanja trodimenzionalnih (3D) struktura, dok slaba privlačna ili snažna odbojna interakcija pogoduju formiranju 2D struktura. Rezultati ovog istraživanja poslužili su kao osnova za ispitivanje adsorpcije litijuma na širokom skupu 2D kristala, koje je iznedrilo jasnu sliku vezivanja litijuma za površinu 2D kristala zasnovanu na transferu naelektrisanja sa metala na površinu. Pored toga, pokazano je da se sposobnost litijuma i kalcijuma da predaju elektrone površini može upotrebiti kao okidač strukturnog faznog prelaza u jednosloju disulfida molibdena (MoS_2). Ustanovljeno je da je prekrivenost MoS_2 litijumom neophodna za ovaj fazni prelaz dvaput veća nego u slučaju kada je na njegovoj površini adsorbovan kalcijum.

KLJUČNE REČI: grafen, 2D materijali, jednosloj MoS_2, DFT, adsorpcija metala, transfer naelektrisanja, litijum-jonske baterije
NAUČNA OBLAST: Fizika
UŽA NAUČNA OBLAST: Fizika kondenzovanog stanja
UDK BROJ: 538.9(043.3)

First-principles study of the structural and electronic properties of metals adsorbed on two-dimensional materials

SUMMARY

The last fifteen years witnessed unprecedented research efforts aimed at exploiting the peculiar properties of two-dimensional (2D) materials in the next generation of nanoelectronic devices. The successful development of these technologies requires thorough understanding of the fundamental physical mechanisms governing the functionalities of fabricated components, where junctions between metals and 2D materials are indispensable. In this thesis, the adsorption of metals on a new class of 2D materials is studied by means of the first-principles calculations, with special emphasis on the structural and electronic properties of formed nanostructures. The employed computational method is based on density functional theory (DFT) that uses the electron density rather than the many-body wavefunction to compute the ground-state properties of atoms, molecules, and crystals.

Choosing lithium, calcium, and titanium as representatives of different classes of metals, we studied their adsorption on graphene. The growth morphology is highly dependent on the nature of adsorbate-adsorbate interaction. In cases where the interaction is strongly attractive, the formation of 3D structures is favored, while the weak attractive or strongly repulsive interaction facilitate the formation of 2D structures. The outcome of this study served as a solid basis for further research on the adsorption of lithium on a large set of other 2D crystals, where the general trends in binding are successfully explained by a simple charge transfer. Once again, lithium's ability to donate electrons to the substrate is exploited to trigger the structural phase transition in molybdenum disulfide monolayer (MoS_2). The Li coverage required to induce the phase transition is determined, whereas it is found that the same effect can be achieved using half as many calcium atoms.

KEYWORDS: graphene, 2D materials, monolayer MoS_2, DFT, metal adsorption, charge transfer, Li-ion batteries
SCIENTIFIC FIELD: Physics
SCIENTIFIC DISCIPLINE: Condensed matter physics
UDC NUMBER: 538.9(043.3)

Contents

Introduction

"Begin at the beginning," the King said, very gravely, "and go on till you come to the end: then stop." , (Lewis Carroll, *Alice in Wonderland*).

During the last decade, among the fastest growing internet communities is the one called *The Flat Earth Society*, which gathers the members from all around the globe. Though I sincerely doubt that two physicists believe our planet is like a giant pancake, their dream of flat or, more precisely, *two-dimensional* (2D) world, when it finally came true, gained to Andre Geim and Konstantin Novoselov the Nobel Prize in Physics. Discovery of *graphene* [1], a single free-standing atomic layer of carbon, successfully ended the long-lasting pursuit for *2D crystals*, while the demonstrations of rich physics hidden in this wonder material have motivated the search for its relatives. In the light of these discoveries, the year of 2004 is now considered *annus mirabilis* that started a whole new era in the materials science.

Since then, more than a hundred of 2D crystals are synthesized with a large diversity in mechanical, electronic, optical, and magnetic properties that opened the immense possibilities and attracted a great deal of attention from both physicists and engineers. Like graphene, which was obtained for the first time from thin films of graphite by a simple duck-tape method, the majority of 2D materials are isolated from their three-dimensional (3D) counterparts. The layered structure of graphite and similar 3D materials enables such a method to work in practice, as they are built out of many individual 2D layers that are loosely connected by weak *van der Waals* (vdW) forces. Furthermore, these forces are responsible for the mechanical stability of the so-called *van der Waals heterostructures*, novel materials which did not exist prior to discovery of 2D crystals and have been successfully synthesized in laboratories by stacking layers of different 2D crystals like LEGO blocks on the nanoscale [2].

The well-known Moore's law [3] states that the number of transistors in a dense integrated circuit doubles every two years. This clever observation, as it is realized by Gordon Moore more than 50 years ago, may be one of the indications that the

evolutionary path of our current electronic technology is narrowing and approaching an end due to quantum-mechanical limitations of silicon at the atomic scale. Therefore, an alternative approach is required and the eyes of many are on novel 2D crystals. Fortunately, a recent breakthrough in the scalable fabrication of 2D crystals is pushing them towards the new stage in nanotechnology [4].

The possibility to produce large quantities of various 2D materials prompted a new interest in their application in electronics. For example, a large family of *transition metal dichalcogenides* (TMDs) holds a yet untapped potential, as it is demonstrated that a nanometer thick semiconducting TMD can adsorb $5-10\%$ incident sunlight, which is an order of magnitude higher than that of standard semiconductors such as GaAs and Si [5]. The aforementioned superiority allows for the construction of solar cells made of MoS_2/graphene and MoS_2/WS_2 bilayers with power conversion efficiencies $1-3$ orders of magnitude higher than that of the best ultra-thin solar cells on the market. Another interesting application of 2D materials is in the electro-mechanical devices for ultra-fast electronics, which exploits the connection between the structural and electronic properties of materials. It is experimentally demonstrated that strain, shear, twisting and bending can be efficiently used to modify the electronic structure of 2D crystal in a desired way, and these parameters are controlled more easily in 2D as compared to 3D systems [6, 7, 8].

To succeed in a rational design of electronic devices, one needs to deeply understand the properties of the individual materials they are made of. Given that there is an interplay between the structure of 2D crystal and its electronic properties, computer modeling is extremely useful at every stage in the development of future electronic devices. Joined forces of quantum-mechanical numerical methods and the power of modern computers resulted in the computational tools that can give insights into the electronic structure of realistic materials. Bearing in mind that the macroscopic samples contain large number ($\sim 10^{23}$) of interacting electrons and nuclei whose physical properties are governed by the Schrödinger equation, one needs to find a roundabout solution to the problem of interacting many-body quantum system. An approach of Walter Kohn and co-workers based on *the electron density* yielded *density functional theory* (DFT), which made possible the calculations of the electronic structure of atoms, molecules, and solids by solving the effectively one-particle equations [9, 10]. Being principally a ground-state theory, DFT enables the computation of many properties such as the equilibrium crystal structure, cohesive energy, charge density, magnetic order, static dielectric and magnetic susceptibilities, just to name a few.

An efficient integration of 2D functional materials into the 3D systems remains a major challenge, as the hidden issues deteriorate device performance and limit circuit design. The contact resistivity of metal on graphene and related 2D materials deserves special attention [11, 12]. Careful reconsideration of the physical models explaining the behavior of these junctions must include the atomic scale description of the interaction between metals and 2D materials. Depending on the growth mode of metal adatoms, when deposited on graphene they can form either smooth ultra-thin films or 3D nanoclusters, with markedly different metallic contacts. Motivated by this problem, we employed DFT to study the microscopic mechanisms responsible for the initial stages of growth of three different metals, namely lithium, calcium, and titanium, on graphene. Tendency towards planar or 3D growth is rationalized based on the atomic-scale description of the interaction between metal adatoms, as well as adsorption geometries of their small clusters. In addition to the characterization of 2D growth mode of Li driven by the long-range electrostatic Li-Li repulsion, we provide an explanation for markedly different 3D growth mode of Ti. Furthermore, we report on the formation of ultra-stable 2D calcium structure on graphene that can not only functionalize this 2D crystal but also cause the three-fold increase in the adhesion in bilayer graphene.

The exponential growth in the number of consumer electronic devices such as mobile phones and notebooks has promoted the efficient energy storage into the one of the most important problems of today. Layered structure and peculiar electronic properties of 2D materials foster the concept of utilizing them as main components of *lithium-ion batteries* (LIBs). We studied the adsorption of lithium on fifteen 2D crystals with versatile structural and electronic properties. The correlation, revealed by DFT calculations, between the strength of Li binding and the position of the lowest unoccupied electronic states in 2D crystals served as a criterion for the division of 2D crystals into two classes. When adsorbed on the majority of considered 2D crystals, valence electron of Li is transferred and spread across a surface, while the binding energy is roughly determined by the position of the *conduction band minimum* (CBM). On the other hand, carbides of Group XIV elements carry out localized charge transfer between Li and the substrate. This gives rise to their capability to accommodate densely packed Li structures with nearly constant binding energy over range of coverages, which may be of importance in the construction of LIBs that are based on these materials.

The fabrication of the first single-layer MoS_2 transistor [13] demonstrated the efficient use of this 2D semiconductor as a channel material for field-effect transistors (FETs). Moreover, when MoS_2 is double-gated, high levels of doping also allow the

observation of metal-insulator transition in the same sheet of monolayer MoS_2 due to strong electron-electron interaction. It is already known from literature that the structural phase transition in TMDs can be achieved via the intercalation with alkaline metals, while the electron charge transfer from intercalants to the surface is indicated as the basic physical mechanism that triggers the structural change [14, 15]. This encouraged us to further study the lithium and calcium adsorption on MoS_2, while the comparison of the electronic properties of Li- and Ca-covered MoS_2 revealed differences in binding pictures of these two metals on MoS_2. Also, we identified the coverages needed to induce this phase transition.

This thesis is organized as follows: after the Introduction we describe the foundations of density functional theory in Chapter 1. Chapter 2 is devoted to the description of different numerical methodologies applied in electronic structure calculations, including *the projector augmented wave* (PAW) method [16]. This method is the pillar of GPAW code [17] used for the majority of calculations in this thesis. After that we present the results on the metal adsorption of graphene (Chapter 4) as well as the lithium adsorption on different 2D crystals (Chapter 5). The structural phase transitions in 2D semiconductor MoS_2 triggered by the adsorption of lithium and calcium, studied in Chapter 6, will finally bring us to Conclusions.

Chapter 1

Density functional theory

The many-body problem in condensed matter physics is a formidable one. Though hamiltonian for systems of interacting particles can often be written down in just a few lines, its eigenvalue problem is rarely analytically solvable. Realistic materials, containing a large number of nuclei and electrons interacting with each other are the archetypal examples of such systems. For practical purposes one can look for numerical solutions of the Schrödinger equation, but even with careful use of symmetry and power of modern supercomputers they can be found for systems encompassing no more than a few electrons.[1] The aforementioned problem draws attention to the urgent need for alternative approaches in the calculations of electronic properties of realistic materials.

This chapter is devoted to *density functional theory* (DFT), which provides an efficient way to describe all the ground state physical properties of the many-body system with the use of just one scalar field – the ground state particle density.

1.1 Schrödinger equation for interacting electrons and nuclei

The systems which are the subject of interest in condensed matter physics are comprised of two types of particles – electrons and nuclei. The basic interaction is electrostatic or Coulomb – two electrons at positions $\mathbf{r}$ and $\mathbf{r}'$ repel one another and potential energy of this interaction is $e^2/|\mathbf{r}-\mathbf{r}'|$. The same stands for nuclei of charge $Z_I e$ and $Z_J e$ at positions $\mathbf{R}_I$ and $\mathbf{R}_J$ whose potential energy of Coulomb repulsion is $Z_I Z_J e^2/|\mathbf{R}_I - \mathbf{R}_J|$. On the other hand, electrons and nuclei are attracted to each other and the potential energy of interaction is $-Z_I e^2/|\mathbf{r}-\mathbf{R}_I|$. If we add kinetic energy operators of particles, we can write down a complete hamiltonian of

[1] Storing an 8 electron wavefunction in $6 \times 6 \times 6$ grid requires $\sim 10^{10}$ GB!

the system,

$$\begin{aligned}\hat{H} = &- \frac{\hbar^2}{2m_e}\sum_i \nabla_i^2 - \sum_{i,I}\frac{Z_I e^2}{|\mathbf{r}_i - \mathbf{R}_I|} + \frac{1}{2}\sum_{i\neq j}\frac{e^2}{|\mathbf{r}_i - \mathbf{r}_j|} \\ &- \sum_I \frac{\hbar^2}{2M_I}\nabla_I^2 + \frac{1}{2}\sum_{I\neq J}\frac{Z_I Z_J e^2}{|\mathbf{R}_I - \mathbf{R}_J|},\end{aligned} \tag{1.1}$$

where quantities related to electrons (nuclei) are written by lower (upper) case letters. The kinetic energy of ions is several orders of magnitude smaller compared to the kinetic energy of electrons. If we neglect the kinetic energy of ions, we come to the *adiabatic* (or *Born-Oppenheimer*) *approximation* (Appendix A), which provides a procedure to separate nuclear and electronic degrees of freedom. It is a fair starting point for many purposes, e.g. the calculations of lattice vibration modes in most solids [18] or a good basis for perturbation theory in electron-phonon interactions, which are crucial for transport properties of metals. Bearing in mind that nuclei are now immobile, we shall treat their contribution to the motion of electrons as *an external field* and positions of nuclei as *parameters* of the hamiltonian. If we adopt Hartree atomic units, where $\hbar = e = m_e = 4\pi\epsilon_0 = 1$, then we can stress out the most general form of hamiltonian for such a system,

$$\hat{H} = \sum_i \Big(-\frac{1}{2}\nabla_i^2 + V_{\text{ext}}(\mathbf{r}_i)\Big) + \frac{1}{2}\sum_{i\neq j}\frac{1}{|\mathbf{r}_i - \mathbf{r}_j|} + E_{II}. \tag{1.2}$$

The first term in (1.2) is the kinetic energy operator for the electrons $\hat{T} = \sum_i -\frac{1}{2}\nabla_i^2$, the second $\hat{V}_{\text{ext}} = \sum_{i,I} V_I(|\mathbf{r}_i - \mathbf{R}_I|) = \sum_i V_{\text{ext}}(\mathbf{r}_i)$ is the external potential acting on electrons due to the presence of nuclei [2], $\hat{V}_{\text{int}} = \frac{1}{2}\sum_{i\neq j} 1/|\mathbf{r}_i - \mathbf{r}_j|$ is the electron-electron interaction and the final term E_{II} is the electrostatic potential energy of nuclei interacting with one another.

Time-dependent Schrödinger equation,

$$\mathrm{i}\frac{\partial\Psi(\{\mathbf{r}\sigma\};t)}{\partial t} = \hat{H}\Psi(\{\mathbf{r}\sigma\};t), \tag{1.3}$$

is the fundamental equation determining the evolution of a non-relativistic quantum system. In equation (1.3) a set of all the spatial coordinates and spins is labeled with $\{\mathbf{r}\sigma\} = (\mathbf{r}_1\sigma_1, \mathbf{r}_2\sigma_2, \ldots, \mathbf{r}_N\sigma_N)$ and N is a total number of particles. If we label with k a complete set of quantum numbers describing an eigenstate of $\hat{H}$ with energy E_k, then the corresponding wavefunction can be written as

[2] We will focus on the external potential acting on electrons due to the nuclei only, but we will leave open the possibility for another external potential to be added later. There are some issues which are out of the scope of this thesis when including extra terms in the external potential. For example, the problem of the external electric field in the spatially periodic systems is a famous one [19, 20]. In this case, there is no true ground state of the system as the potential $V(x) = Ex$ is unbounded. This is an obstacle as DFT is primarily a ground state theory.

$\Psi_k(\{\mathbf{r}\sigma\};t) = \Psi_k(\{\mathbf{r}\sigma\})\mathrm{e}^{-\mathrm{i}E_k t}$. Written in this way, the time is separated from the spatial coordinates (and spins) and the squared modulus of the wavefunction $|\Psi_k|^2$ is time-independent. Furthermore, the expectation value of any observable $\hat{O}$ in an eigenstate of $\hat{H}$ is time-independent, and a suitable expression involves an integral over all spatial coordinates and spins

$$\langle\hat{O}\rangle \stackrel{\mathrm{def}}{=} \frac{\langle\Psi|\hat{O}|\Psi\rangle}{\langle\Psi|\Psi\rangle}. \tag{1.4}$$

From now on, let us focus on an N-electron system in a time-independent external field emerging from fixed nuclei. This system is conservative, thus its eigenproblem is governed by a time-independent Schrödinger equation

$$\hat{H}\Psi_k(\{\mathbf{r}\sigma\}) = E_k\Psi_k(\{\mathbf{r}\sigma\}). \tag{1.5}$$

Electrons are fermions so they obey the Pauli exclusion principle, hence the wavefunction must be antisymmetric under the exchange of the indices of any two electrons

$$\begin{aligned}&\Psi(\mathbf{r}_1\sigma_1,\ldots,\mathbf{r}_i\sigma_i,\ldots,\mathbf{r}_j\sigma_j,\ldots,\mathbf{r}_N\sigma_N) = \\ &-\Psi(\mathbf{r}_1\sigma_1,\ldots,\mathbf{r}_j\sigma_j,\ldots,\mathbf{r}_i\sigma_i,\ldots,\mathbf{r}_N\sigma_N).\end{aligned} \tag{1.6}$$

There are $N!$ distinct permutations of indices $i,j \in \{1,2,\ldots,N\}$ with the same value of $|\Psi|^2$, therefore $N!|\Psi(\mathbf{r}_1\sigma_1,...,\mathbf{r}_N\sigma_N)|^2\,\mathrm{d}^3\mathbf{r}_1\ldots\mathrm{d}^3\mathbf{r}_N$ is the probability to find *any* electron with spin σ_1 [3] in the volume element $\mathrm{d}^3\mathbf{r}_1$. Because the total probability is normalized to 1, this leads to

$$\frac{1}{N!}\sum_{\sigma_1,\ldots,\sigma_N}\int\mathrm{d}^3\mathbf{r}_1\ldots\int\mathrm{d}^3\mathbf{r}_N\,N!\;|\Psi(\mathbf{r}_1\sigma_1,\ldots,\mathbf{r}_N\sigma_N)|^2 = \langle\Psi\,|\,\Psi\rangle = 1. \tag{1.7}$$

Now we will proceed towards defining *the electron spin density* $n^\sigma(\mathbf{r})$. Firstly, we shall notice that $n_\sigma(\mathbf{r})\mathrm{d}^3\mathbf{r}$ is the probability of finding an electron with spin σ in a volume element $\mathrm{d}^3\mathbf{r}$ at $\mathbf{r}$. Accordingly, we find $n^\sigma(\mathbf{r})$ by integrating over the spatial coordinates and spins of the rest of $N-1$ electrons,

$$\begin{aligned}n_\sigma(\mathbf{r}) &= \frac{1}{(N-1)!}\sum_{\sigma_2,\ldots,\sigma_N}\int\mathrm{d}^3\mathbf{r}_2\ldots\int\mathrm{d}^3\mathbf{r}_N\,N!\;|\Psi(\mathbf{r}\sigma,\ldots,\mathbf{r}_N\sigma_N)|^2 \\ &= N\sum_{\sigma_2,\ldots,\sigma_N}\int\mathrm{d}^3\mathbf{r}_2\ldots\int\mathrm{d}^3\mathbf{r}_N\,|\Psi(\mathbf{r}\sigma,\ldots,\mathbf{r}_N\sigma_N)|^2 = \langle\Psi\,|\,\hat{n}_\sigma(\mathbf{r})\,|\,\Psi\rangle\,.\end{aligned} \tag{1.8}$$

A consequence of the equations (1.7) and (1.8) is that $n_\sigma(\mathbf{r})\mathrm{d}^3\mathbf{r}$ is the number of electrons with spin σ in the volume element $\mathrm{d}^3\mathbf{r}$ as its integral over the volume

[3] If not stated otherwise, we will use the term *spin of the electron* to refer to its projection on the z-axis, that is $\sigma = \pm\frac{1}{2}$.

of the sistem and sum over spins is equal to the total number of electrons, i.e. $\sum_\sigma \int \mathrm{d}^3\mathbf{r}\, n_\sigma(\mathbf{r}) = N$.

In equation (1.8) we defined *a spin density operator*,

$$\hat{n}_\sigma(\mathbf{r}) = \sum_i \delta(\mathbf{r} - \mathbf{r}_i)\delta_{\sigma\sigma_i}, \tag{1.9}$$

where $\delta(\mathbf{r} - \mathbf{r}_i)$ is the Dirac delta function and $\delta_{\sigma\sigma_i}$ is the Kronecker symbol. The expectation value of operator $\hat{n}_\sigma(\mathbf{r})$ in the state $\Psi(\{\mathbf{r}_i\sigma_i\})$ is nothing other than the electron spin density $n_\sigma(\mathbf{r})$ in this state. Furthermore, expectation value of external potential is

$$\langle\hat{V}_{\mathrm{ext}}\rangle = \langle\Psi|\sum_i V_{\mathrm{ext}}(\mathbf{r}_i)|\Psi\rangle = \int \mathrm{d}^3\mathbf{r}\, n(\mathbf{r})V_{\mathrm{ext}}(\mathbf{r}), \tag{1.10}$$

where $n(\mathbf{r}) = \sum_\sigma n^\sigma(\mathbf{r})$ is *the electron density*. In a similar manner the operator expectation value in state $|\Psi\rangle$ is expressed by using the electron density $n(\mathbf{r})$ in the same state, i.e. as *a functional* of the electron density. This is the idea we will continue to follow in the next sections.

1.1.1 Variational principle

Schrödinger equation can be solved directly – for a known hamiltonian, one can calculate the eigenstates and the corresponding eigenvectors via the diagonalization procedure in a chosen basis. As mentioned in the previous section, this approach is suitable for only a few simple quantum systems. A restatement of the problem can be found with the aid of *Rayleigh-Ritz variational principle*.

■ **Rayleigh-Ritz theorem:** Let us suppose that hamiltonian $\hat{H}$ has a purely discrete spectrum. Let the *energy functional* be defined as follows

$$E(|\Psi\rangle) \stackrel{\mathrm{def}}{=} \frac{\langle\Psi|\hat{H}|\Psi\rangle}{\langle\Psi\,|\,\Psi\rangle}. \tag{1.11}$$

Then the stationary points of $E(|\Psi\rangle)$ are the eigenvectors of $\hat{H}$, while the stationary values are eigenvalues of $\hat{H}$.

Proof. The variation of (1.11) together with the stationary condition $\delta E(|\Psi\rangle) = 0$ leads to $\langle\delta\Psi|(\hat{H} - E(|\Psi\rangle))|\Psi\rangle + \langle\Psi|(\hat{H} - E(|\Psi\rangle))|\delta\Psi\rangle = 0$. Because vectors, $|\Psi\rangle$, and functionals, $\langle\Psi|$, can be varied independently, both terms in this equation must vanish. Since $\langle\Psi|(\hat{H} - E(|\Psi\rangle))|\delta\Psi\rangle = 0$ must hold for any possible $|\delta\Psi\rangle$, this can be fulfilled if and only if $|\Psi\rangle$ satisfies the time-independent Schrödinger equation, that is $(\hat{H} - E(|\Psi\rangle))\,|\Psi\rangle = 0$. □

The most profound consequence of the theorem is that the ground state energy is less than or equal to the value of the energy functional in any state, i.e. $E_0 \leq E(|\Psi\rangle), \forall\, |\Psi\rangle \in \mathcal{S}$, where $\mathcal{S}$ is the full state space of the system. To find the ground state energy, one needs to solve the variational problem of the energy functional over the entire state space. Stated in this way, it is nothing more but an equivalent reformulation of the original eigenproblem, thus it brings no advantage to solving it. Instead of the entire state space S, we should choose only its part $\mathcal{T} \subset \mathcal{S}$, called *the trial set*. With the variational method we find the stationary points within $\mathcal{T}$ and the best approximation for the ground state $|\Psi_0\rangle$ is that function $|\Phi_0\rangle \in \mathcal{T}$ which minimizes $E(|\Psi\rangle)$ over $\mathcal{T}$. For example, by restricting $\mathcal{T}$ to Slater determinants of plane waves one recovers *the Hartree-Fock approximation* (HFA)[21, 22, 23]. One of the great advantages of DFT in comparison to the HFA is the inclusion of the electron correlation effects.

1.1.2 Hellman-Feynman theorem

In the first part of Section 1.1 we mentioned that, in adiabatic approximation, the hamiltonian depends parametrically upon positions of nuclei $\{\mathbf{R}\}$. In cases like this, when hamiltonian depends upon some parameter, *the Hellman-Feynman theorem* provides an expression for the force conjugate to this parameter. Suppose that the hamiltonian $\hat{H}_\lambda$ depends upon a parameter (or a set of parameters) λ, then the energy functional of the system is defined as $E_\lambda = \langle\Psi_\lambda|\hat{H}_\lambda|\Psi_\lambda\rangle$, where it is assumed that $|\Psi_\lambda\rangle$ is a normalized variational solution. Differentiating E_λ yields

$$\frac{\mathrm{d}E_\lambda}{\mathrm{d}\lambda} = \frac{\mathrm{d}}{\mathrm{d}\lambda'}\big\langle\Psi_{\lambda'}|\hat{H}_\lambda|\Psi_{\lambda'}\big\rangle\Big|_{\lambda=\lambda'} + \big\langle\Psi_\lambda|\frac{\partial\hat{H}_\lambda}{\partial\lambda}|\Psi_\lambda\big\rangle. \tag{1.12}$$

The first term of (1.12) vanishes by variational principle, and the second term gives the Hellman-Feynman theorem,

$$\frac{\mathrm{d}E_\lambda}{\mathrm{d}\lambda} = \big\langle\Psi_\lambda|\frac{\partial\hat{H}_\lambda}{\partial\lambda}|\Psi_\lambda\big\rangle. \tag{1.13}$$

This theorem provides the gradient of the path which minimizes energy on the given energy surface. It is also crucial for understanding the concept of exchange-correlation functional. To point out its importance, let us derive one of the profound implications, that is the expression for forces acting on nuclei in an electron-nuclear system [24]. In hamiltonian (1.2) terms that depend explicitly upon nuclear positions $\{\mathbf{R}\}$ are $\hat{V}_{\mathrm{ext}}$ and E_{II}. With the help of (1.10), we can find the force acting on a nucleus I by varying the energy with nuclear position $\mathbf{R}_I$ while keeping the positions

of other nuclei fixed,

$$\begin{aligned}\mathbf{F}_I = -\frac{\partial E}{\partial \mathbf{R}_I} &= -\langle\Psi|\frac{\partial \hat{H}}{\partial \mathbf{R}_I}|\Psi\rangle = -\langle\Psi|\frac{\partial \hat{V}_{\text{ext}}}{\partial \mathbf{R}_I} + \frac{\partial E_{II}}{\partial \mathbf{R}_I}|\Psi\rangle \\ &= \int \mathrm{d}^3\mathbf{r}\, n(\mathbf{r})\frac{Z_I(\mathbf{r}-\mathbf{R}_I)}{|\mathbf{r}-\mathbf{R}_I|^3} + \sum_{I\neq J}\frac{Z_I Z_J(\mathbf{R}_I-\mathbf{R}_J)}{|\mathbf{R}_I-\mathbf{R}_J|^3}.\end{aligned} \tag{1.14}$$

Here $n(\mathbf{r})$ is the unperturbed ground state electron density for a particular nuclear configuration $\{\mathbf{R}\}$. It is now clear that (1.14) gives the electrostatic force on nucleus I as it is just an electric field at $\mathbf{R}_I$ due to the presence of electrons and other nuclei times the charge of this nucleus Z_I. In other words, even though kinetic energy of electrons and electron-electron interaction change as the nuclei move, their contribution to the electrostatic force acting on the nuclei cancel out. We must be careful here because it is not always possible to express forces acting on nuclei solely in terms of the electron density. The most typical example stems from the core electrons – when calculating the force on a given nucleus, it is more natural to move the corresponding core electron density along with the nucleus instead of keeping it fixed as it is required by the force theorem. For further discussion, we refer to [25].

1.2 Hohenberg-Kohn theorems

The origins DFT can be found in the original works of Thomas [26] and Fermi [27] way back in 1927., however, modern formulation as an exact quantum theory for the ground state of the many-body systems is due to the work of Hohenberg and Kohn [9]. Their approach is suitable for any system of interacting particles in an external potential including any problem of electrons and fixed nuclei. In this section we will formulate and prove two general theorems which are governing the very foundation of DFT and stress out their most important consequences which will be used latter in this section for a proper definition of energy functional of a quantum many-body system with hamiltonian (1.2).

- ■ **Theorem 1:** For any quantum system of interacting particles in an external potential $V_{\text{ext}}(\mathbf{r})$, the ground state density of particles $n_0(\mathbf{r})$ uniquely determines, except for a constant, this external potential $V_{\text{ext}}(\mathbf{r})$.

- ♠ **Comment on Theorem 1:** All the terms in hamiltonian, except the external potential $V_{\text{ext}}(\mathbf{r})$, are system-independent, i.e. they are the same for all the systems of its kind. Therefore, if $V_{\text{ext}}(\mathbf{r})$ is known then it follows that wavefunctions for all states are determined. Thus all properties of the many-body systems are, in principle, determined by the ground state particle density.

Proof of the Theorem 1. Proof of the theorem is simple and illustrative. Contrary to its prediction, suppose that there exist two different external potentials $V_{\text{ext}}(\mathbf{r})$ and $V'_{\text{ext}}(\mathbf{r})$ which differ by more than a constant but generate the same ground state density $n_0(\mathbf{r})$. These potentials lead to two different hamiltonians, $\hat{H}$ and $\hat{H}'$, whose ground states $|\Psi_0\rangle$ and $|\Psi'_0\rangle$ are different. Since $|\Psi'_0\rangle$ is not the ground state of $\hat{H}$, it follows from the variational principle that

$$E_0 = \langle\Psi_0|\hat{H}|\Psi_0\rangle < \langle\Psi'_0|\hat{H}|\Psi'_0\rangle\,. \tag{1.15}$$

The strict inequality holds if the ground state is non-degenerate, which we will assume for the sake of simplicity [4]. The last term in (1.15) can be written as

$$\begin{aligned}\langle\Psi'_0|\hat{H}|\Psi'_0\rangle &= \langle\Psi'_0|\hat{H}'|\Psi'_0\rangle + \langle\Psi'_0|\hat{H} - \hat{H}'|\Psi'_0\rangle \\ &= E'_0 + \int \mathrm{d}^3\mathbf{r}\,[V_{\text{ext}}(\mathbf{r}) - V'_{\text{ext}}(\mathbf{r})]n_0(\mathbf{r}),\end{aligned} \tag{1.16}$$

and from (1.15) follows

$$E_0 < E'_0 + \int \mathrm{d}^3\mathbf{r}\,[V_{\text{ext}}(\mathbf{r}) - V'_{\text{ext}}(\mathbf{r})]n_0(\mathbf{r}). \tag{1.17}$$

Changing the roles of E'_0 and E_0 and repeating the last few steps yields

$$E'_0 < E_0 + \int \mathrm{d}^3\mathbf{r}\,[V'_{\text{ext}}(\mathbf{r}) - V_{\text{ext}}(\mathbf{r})]n_0(\mathbf{r}). \tag{1.18}$$

Now if we add (1.17) and (1.18) together we arrive at a contradiction $E_0 + E'_0 < E_0 + E'_0$. We conclude that our assumption does not hold and there don't exist two potentials which differ by more than a constant and yield the same ground state density $n_0(\mathbf{r})$. Therefore the density uniquely determines the external potential up to a constant. □

Theorem 1 validates the particle density as a basic variable for the description of the many-body system's properties. The next step is to connect the ground state energy of the system to its particle density. This is achieved by the defining the energy of a system as a functional of the density within the second Hohenberg-Kohn theorem.

■ **Theorem 2:** For any quantum system of interacting particles in an external potential $V_{\text{ext}}(\mathbf{r})$, a *universal functional* for the energy $E[n]$ which depends solely on density $n(\mathbf{r})$ can be defined such that the exact ground state energy of a system is a global minimum of $E[n]$. For any given $V_{\text{ext}}(\mathbf{r})$, a density which minimizes $E[n]$ is the exact ground state density $n_0(\mathbf{r})$.

[4] The assumption of non-degenerate ground state comes from the original work of Hohenberg and Kohn and does not decrease the generality of the theorem. Thorough discussion on degenerate ground states is given in [28], p. 18-21.

♠ **Comment on Theorem 2:** If $E[n]$ is known than one can get ground state energy and density via variational principle. The excited states, though known in principle as stated in the comment following the Theorem 1, must be determined by other means. DFT is genuinely the theory of *the ground state* of the many-body quantum systems.

Since we are interested in the electronic structure of realistic materials, we should focus on the systems described by hamiltonian (1.2). The Theorem 2 can be generalized and thus its validity expanded, but that discussion is out of the scope of this thesis. In Subsection 1.1.1 we concluded that the quality of the approximation for the exact ground state wavefunction is limited by the particular choice of the trial set $\mathcal{T}$ over which the energy is minimized. If $\mathcal{T}$ is strictly confined to the wavefunctions which yield the same electron density $n(\mathbf{r})$ (and that is the only constraint), then the wavefunction $\Psi_0 \in \mathcal{T}$ which minimizes the energy is *the exact* ground state of the system whose ground state density is $n(\mathbf{r})$.[5] Since all the properties of the system, by the statements of the Theorems 1 and 2, are given if we know the ground state electronic density, then one can define *the total energy functional*[6] as follows

$$\begin{aligned} E_{\mathrm{HK}}[n] &= \langle \Psi_0[n] | \hat{T} + \hat{V}_{\mathrm{int}} + \hat{V}_{\mathrm{ext}} + E_{II} | \Psi_0[n] \rangle \\ &= T[n] + E_{\mathrm{int}}[n] + \int \mathrm{d}^3\mathbf{r}\, n(\mathbf{r}) V_{\mathrm{ext}}(\mathbf{r}) + E_{II} \\ &\equiv F_{\mathrm{HK}}[n] + \int \mathrm{d}^3\mathbf{r}\, n(\mathbf{r}) V_{\mathrm{ext}}(\mathbf{r}) + E_{II}, \end{aligned} \tag{1.19}$$

where we have used (1.10) in the second line.

$\hat{T}$ is the kinetic energy operator for electrons, $\hat{V}_{\mathrm{int}}$ is the operator of electron-electron interaction, $\hat{V}_{\mathrm{ext}}$ is the external field generated by nuclei (and any other spin-independent external fields) and E_{II}[7] is the nucleus-nucleus interaction energy. In the last line of (1.19) we have defined the functional $F_{\mathrm{HK}} \stackrel{\mathrm{def}}{=} T[n] + E_{\mathrm{int}}[n]$ which includes all internal energies, kinetic and potential, of the interacting electron system. F_{HK} is universal, i.e. it depends on the electronic density only, and not on the external potential. Now we can easily prove *Theorem 2.*

Proof of the Theorem 2. Consider an electronic system with the ground state density $n_0(\mathbf{r})$ corresponding to an external potential $V_{\mathrm{ext}}(\mathbf{r})$. A ground state energy of

[5] Not every scalar field $f(\mathbf{r}) : \mathbb{R}^3 \mapsto \mathbb{R}$ represents a density of the many-electron system. One of the limitations of this particular choice is that the energy functional, defined in this way, must be generated by some external potential. This is called *V-representability* and the conditions for such choice to be made is not known in general [28].

[6] This is the total energy functional as defined in the original work of Hohenberg and Kohn [9]. There is also an alternative *constrained search formulation* of Levy and Lieb which is to some extent more instructive and clarifies the physical meaning of the energy functional [29].

[7] There is no "hat" above this term because it is not an operator acting on the state space of electrons, i.e. it does not explicitly depend on the electronic coordinates.

the system is the value of the functional E_{HK} for the ground state density $n_0(\mathbf{r})$ and by variational principle it is the expectation value of the hamiltonian in the ground state $|\Psi_0\rangle$,

$$E_0 = E_{\mathrm{HK}}[n_0] = \langle\Psi_0|\hat{H}|\Psi_0\rangle\,. \tag{1.20}$$

Another density $n'(\mathbf{r})$ necessarily corresponds to a different state $|\Psi'\rangle$ and the energy in that state is higher than in the ground state

$$E_0 = \langle\Psi_0|\hat{H}|\Psi_0\rangle < \langle\Psi'|\hat{H}|\Psi'\rangle = E_{\mathrm{HK}}[n'] \tag{1.21}$$

Thus we deduce that the value of the total energy functional $E_{\mathrm{HK}}[n]$ for any other density is higher than the value in the ground state density, that is the ground state energy of the system. □

Despite the strong statement of Theorem 2, there is no procedure on how to construct external potential for a known ground state density. The energy functional $E_{\mathrm{HK}}[n]$, in general, is not known. Next section is devoted to the roundabout solution to this problem.

1.3 Kohn-Sham ansatz

The basic idea behind the approach of Kohn and Sham [10] stems from the mean-field approximation – replacing the system of interacting electrons in an external potential by *the auxiliary* system of non-interacting electrons in the effective one-particle potential. The connection between the two is the ground state density, which must be the same for both systems. *Kohn-Sham ansatz* (KS) [8] is based upon two assumptions:

1. The exact ground state density of the interacting many-electron system can be represented by the density of the auxiliary system of non-interacting electrons.

2. The auxiliary hamiltonian contains two terms - the usual kinetic operator and an effective *local* potential $V_{\mathrm{eff}}(\mathbf{r})$ acting on an electron at point $\mathbf{r}$.

The first assumption is known as *the non-interacting V-representability* and, to the best of our knowledge, there is no rigorous proof of its validity. Nonetheless, we will proceed with this assumption.[9] The assumed locality of $V_{\mathrm{eff}}(\mathbf{r})$ in the second assumption is not crucial to the KS ansatz but it is exceedingly useful. The schematic representation of the KS ansatz is given in Fig. 1.1. Despite the assumption that $\hat{V}_{\mathrm{ext}}$

[8] *ansatz* - the word is from German and it means "educated guess to be later verified".
[9] We follow the rationale that it's easier to ask for forgiveness than to get a permission.

Figure 1.1: Schematic representation of Kohn-Sham ansatz. Quantities of the interacting (non-interacting) system are given on the left (right). The connection between the two is provided by the arrow with the KS label above it. The notation HK_0 is used to emphasize that HK theorems are applied to a non-interacting system. The many-body wavefunctions of the interacting system are labeled with large Ψ and the one-particle Kohn-Sham orbitals are labeled with the small letters ψ (the scheme is taken from [25]).

$$
\begin{array}{ccccccc}
V_{\mathrm{ext}}(\mathbf{r}) & \overset{\mathrm{HK}}{\Longleftarrow} & n_0(\mathbf{r}) & \overset{\mathrm{KS}}{\Longleftrightarrow} & n_0(\mathbf{r}) & \overset{\mathrm{HK}_0}{\Longrightarrow} & V_{\mathrm{KS}}(\mathbf{r}) \\
\Downarrow & & \Uparrow & & \Uparrow & & \Downarrow \\
\Psi_i(\{\mathbf{r}\}) & \Longrightarrow & \Psi_0(\{\mathbf{r}\}) & & \psi_{i=1,N_e}(\mathbf{r}) & \Longleftarrow & \psi_i(\mathbf{r})
\end{array}
$$

does not depend on spin, the spin dependency of $V_{\mathrm{eff}}(\mathbf{r})$ is necessary for the correct ground state density for each spin. Thus it should be written as $V^{\sigma}_{\mathrm{eff}}(\mathbf{r})$ to emphasize that the effective potential is different for spin-up and spin-down electrons. For the sake of simplicity, we will abandon the spin dependence of $V^{\sigma}_{\mathrm{eff}}(\mathbf{r})$, but we will discuss it when necessary. Now, let us write the hamiltonian for the auxiliary independent-particle system. By the assumptions of the KS ansatz we have

$$\hat{H}_{\mathrm{aux}} = -\frac{1}{2}\nabla^2 + V_{\mathrm{eff}}(\mathbf{r}). \tag{1.22}$$

Currently, an exact form of $V_{\mathrm{eff}}(\mathbf{r})$ is not specified. The potential which yields the ground state density of the independent particle system (and, by means of KS ansatz, of the interacting system) will be found through the variational procedure which can be performed only if the expression (1.22) holds for a broader range of effective potentials. In that sense $V_{\mathrm{eff}}(\mathbf{r})$ is a set or a family of potentials.

If the system contains N independent electrons, its ground state is a Slater determinant of the N lowest lying orbitals $\psi_i(\mathbf{r})$, and the ground state density is just the sum of the squared moduli of occupied orbitals

$$n(\mathbf{r}) = \sum_{i=1}^{N} |\psi_i(\mathbf{r})|^2 = \sum_{i}^{\mathrm{occ.}} |\psi_i(\mathbf{r})|^2. \tag{1.23}$$

Kinetic energy of the independent particles is given by [10]

$$T_s = -\frac{1}{2}\sum_{i=1}^{N} \langle \psi_i | \nabla^2 | \psi_i \rangle = \frac{1}{2}\sum_{i=1}^{N} |\nabla \psi_i|^2. \tag{1.24}$$

[10] After partial integration, the first term which is of the form $(\psi^*(\mathbf{r})\nabla\psi(\mathbf{r}))|_S$ (S is the surface of the system) vanishes as either $\psi|_S$ or $\nabla\psi|_S$ must vanish at the system's border. Note that the kinetic energy of independent particles is labeled with "s" subscript to distinguish it from the kinetic energy $T[n]$ of the interacting many-electron system.

The classical Coulomb interaction energy of the electron density $n(\mathbf{r})$ with itself, the so-called *Hartree term*, is defined as follows

$$E_{\mathrm{H}} = \frac{1}{2} \int \mathrm{d}^3\mathbf{r}\, \mathrm{d}^3\mathbf{r}'\, \frac{n(\mathbf{r})n(\mathbf{r}')}{|\mathbf{r} - \mathbf{r}'|}. \tag{1.25}$$

Now let us write the expression for the total energy within KS approach and find its connection to the total energy (1.19) of the interacting many-body system

$$E_{\mathrm{KS}}[n] = T_s[n] + \int \mathrm{d}^3\mathbf{r}\, n(\mathbf{r}) V_{\mathrm{ext}}(\mathbf{r}) + E_{\mathrm{H}}[n] + E_{II} + E_{\mathrm{xc}}[n]. \tag{1.26}$$

There are few remarks about the last expression. First, we assumed that the system is electroneutral and thus the sum including the terms V_{ext}, E_{H} and E_{II} forms a neutral grouping, which is important when dealing with the infinite spatially periodic systems with long-range Coulomb interaction.[11] Secondly, the kinetic energy of the independent-particle system T_s is expressed in (1.24) as a functional of the orbitals, though by application of the Hohenberg-Kohn theorems it must be a unique functional of the density $n(\mathbf{r})$. This condition is fulfilled as the ground state density uniquely determines all the wavefunctions of the independent particle system and the kinetic energy is just the sum of the squares of the wavefunctions' moduli, thus it is uniquely determined. Lastly, by the condition that the total energy of the auxiliary system must be equal to the total energy of the fully interacting one, and comparing (1.26) to (1.19) we find the expression for the term which includes all the many-body effects of exchange and correlation,

$$\begin{aligned} E_{\mathrm{xc}}[n] &= F_{\mathrm{HK}}[n] - (T_s[n] + E_{\mathrm{H}}[n]) \\ &= \langle \hat{T} \rangle - T_s[n] + \langle \hat{V}_{\mathrm{int}} \rangle - E_{\mathrm{H}}[n]. \end{aligned} \tag{1.27}$$

The last expression is the definition of the *exchange-correlation* (XC) *functional* within the Kohn-Sham approach. The last line of (1.27) reveals that E_{xc} is the difference between the kinetic and internal energy of the true interacting many-electron systems and their analogs, fictitious independent-particle systems. More details on this topic can be found in Section 1.4.

The connection between the two systems is thus fully established, and if the universal functional $E_{\mathrm{xc}}[n]$ were known then the ground state energy (and density) could be found by varying $E_{\mathrm{KS}}[n]$ with respect to either the density $n(\mathbf{r})$ or the effective potential $V_{\mathrm{eff}}(\mathbf{r})$. Next subsection is devoted to the variation of $E_{\mathrm{KS}}[n]$ and the derivation and solution of the Kohn-Sham equations which are governing this procedure.

[11] See, for example, App. F of [25].

1.3.1 The Kohn-Sham variational equations

The Kohn-Sham equations are the Euler-Lagrange equations corresponding to the variation of the energy functional $E_{\rm KS}[n]$ with respect to orbitals. If we have an arbitrary functional of density $\Omega[n]$ then its *variational derivative* is defined as follows

$$\delta\Omega[n] \stackrel{\rm def}{=} \Omega[n+\delta n] - \Omega[n] = \int {\rm d}^3\mathbf{r}\, \frac{\delta\Omega}{\delta n(\mathbf{r})}\delta n(\mathbf{r}). \tag{1.28}$$

All the terms in (1.26) except the kinetic energy $T_s[n]$ depend explicitly on the electronic density, and the electronic density together with $T_s[n]$ are explicitly expressed as a functional of the orbitals. Hence, one can vary $E_{\rm KS}$ with respect to the orbitals and use the chain rule to derive the variational equation

$$\frac{\delta E_{\rm KS}}{\delta\psi_i^*(\mathbf{r})} = \frac{\delta T_s}{\delta\psi_i^*(\mathbf{r})} + \left[\frac{\delta E_{\rm ext}}{\delta n(\mathbf{r})} + \frac{\delta E_{\rm H}}{\delta n(\mathbf{r})} + \frac{\delta E_{\rm xc}}{\delta n(\mathbf{r})}\right]\frac{\delta n(\mathbf{r})}{\delta\psi_i^*(\mathbf{r})}. \tag{1.29}$$

Since the orbitals are orthonormal, $\langle\psi_i|\psi_j\rangle = \delta_{ij}$, the variational derivative of $n(\mathbf{r})$ with respect to orbitals can be easily found from (1.23)

$$\frac{\delta n(\mathbf{r})}{\delta\psi_i^*(\mathbf{r})} = \psi_i(\mathbf{r}), \tag{1.30}$$

and of T_s from (1.24)

$$\begin{aligned}\frac{\delta T_s}{\delta\psi_i^*(\mathbf{r})} &= -\frac{1}{2}\sum_{j=1}^{N}\int {\rm d}^3\mathbf{r}'\, \frac{\delta\psi_j^*(\mathbf{r}')}{\delta\psi_i^*(\mathbf{r})}\nabla^2\psi_j(\mathbf{r}'),\\ &= -\frac{1}{2}\int {\rm d}^3\mathbf{r}'\, \delta(\mathbf{r}-\mathbf{r}')\nabla^2\psi_i(\mathbf{r}') = -\frac{1}{2}\nabla^2\psi_i(\mathbf{r}).\end{aligned} \tag{1.31}$$

By means of the variational principle, the expression (1.29) must be equal to zero. Hence, adding the constraint of orthonormalization of the wavefunctions through the Lagrange multiplier method, we have

$$\frac{\delta}{\delta\psi_i^*(\mathbf{r})}\left\{E_{\rm KS}[n] - \sum_{j=1}^{N}\varepsilon_j\Big[\big\langle\psi_j|\psi_j\big\rangle - 1\Big]\right\} = 0, \tag{1.32}$$

which results in *the Kohn-Sham equations*

$$\Big[-\frac{1}{2}\nabla^2 + V_{\rm KS}(\mathbf{r})\Big]\psi_i(\mathbf{r}) = \varepsilon_i\psi_i(\mathbf{r}). \tag{1.33}$$

The expression (1.33) is the eigenproblem of the auxiliary hamiltonian $\hat{H}_{\rm KS}$, whose eigenvalues are the so-called *Kohn-Sham energies*, and the corresponding eigenfunctions are known as *the Kohn-Sham orbitals*. We have also defined the *Kohn-Sham potential*,

$$V_{\rm KS}(\mathbf{r}) = V_{\rm ext}(\mathbf{r}) + \frac{\delta E_{\rm H}}{\delta n(\mathbf{r})} + \frac{\delta E_{\rm xc}}{\delta n(\mathbf{r})} \equiv V_{\rm ext}(\mathbf{r}) + V_{\rm H}(\mathbf{r}) + V_{\rm xc}(\mathbf{r}). \tag{1.34}$$

where $V_{\rm H}(\mathbf{r}) = \int \mathrm{d}^3\mathbf{r}' n(\mathbf{r}')/|\mathbf{r}-\mathbf{r}'|$ is *the Hartree potential* and $V_{\rm xc}(\mathbf{r}) = \frac{\delta E_{\rm xc}}{\delta n(\mathbf{r})}$ is the *exchange-correlation* (XC) *potential*. Equations (1.33) and (1.34) are equivalent to the variational problem. They have the form of independent-particle equations with the effective potential $V_{\rm KS}(\mathbf{r})$ which must be determined self-consistently with the corresponding density. From the Hohenberg-Kohn theorems it follows that the ground state density uniquely determines the Kohn-Sham potential from the set of potentials, that is $V_{\rm eff}(\mathbf{r})|_{n_0(\mathbf{r})} = V_{\rm KS}(\mathbf{r})$. If one would have the exact form of $E_{\rm xc}[n]$, then (1.33) and (1.34) would lead to the ground state density and energy of the system of independent particles and, by means of the KS ansatz, to the true ground state density and energy of the interacting many-electron system. When dealing with the spin-polarized systems, one needs to solve the Kohn-Sham equations for each spin, and due to $V_{\rm eff}^{\uparrow}(\mathbf{r}) \neq V_{\rm eff}^{\downarrow}(\mathbf{r})$ the spin-up spectrum will differ from the spin-down spectrum.

KS equations must be solved by means of the iterative *self-consistent field method* (SCF). The standard procedure is as follows: the input density $n_{\rm in}^{(m)}(\mathbf{r})$ of the m-th cycle generates the effective potential $V_{\rm eff}^{(m)}(\mathbf{r})$ for which one solves the KS equations (1.33) to obtain the eigenvalues $\{\varepsilon_i^{(m)}\}$ and orbitals $\{\psi_i^{(m)}\}$. Calculated orbitals yield the output density $n_{\rm out}^{(m)}(\mathbf{r}) = \sum_i^{\rm occ.} |\psi_i^{(m)}|^2$ of the m-th cycle which is used for the construction of the input density for the $(m+1)$-th cycle. The procedure is repeated until the self-consistency is reached, i.e. until the input and the output density differ less than the predefined value. Full SCF KS scheme is depicted in Fig. 1.2.

The total energy of the system $E_{\rm tot}[n]$ can be calculated for any density, as it is needed for the iterative procedure. Hence, let us derive the expression for the total energy within the KS approach in terms of density and eigenvalues. For the assumed effective potential $V_{\rm eff}(\mathbf{r})$ and the corresponding density, from (1.24) and (1.33) one gets

$$\begin{aligned} T_s[n] &\equiv \sum_i^{\rm occ.} \int \mathrm{d}^3\mathbf{r}\, \psi_i^*(\mathbf{r}) \left(-\frac{1}{2}\nabla^2\right) \psi_i(\mathbf{r}), \\ &= \sum_i^{\rm occ.} \int \mathrm{d}^3\mathbf{r} [\varepsilon_i - V_{\rm eff}(\mathbf{r})] \psi_i^*(\mathbf{r})\psi_i(\mathbf{r}) = \sum_i^{\rm occ.} \varepsilon_i - \int \mathrm{d}^3\mathbf{r}\, n(\mathbf{r}) V_{\rm eff}(\mathbf{r}). \end{aligned} \tag{1.35}$$

Together with (1.26), it yields

$$E_{\rm tot}[n] = \sum_i^{\rm occ.} \varepsilon_i - \int \mathrm{d}^3\mathbf{r}\, n(\mathbf{r}) V_{\rm eff}(\mathbf{r}) + \int \mathrm{d}^3\mathbf{r}\, n(\mathbf{r}) V_{\rm ext}(\mathbf{r}) + E_{\rm H}[n] + E_{\rm xc}[n] + E_{II}, \tag{1.36}$$

or equivalently, employing the definition (1.34) for $V_{\rm xc}(\mathbf{r})$

$$E_{\rm tot}[n] = \sum_i^{\rm occ.} \varepsilon_i - \frac{1}{2}\int \mathrm{d}^3\mathbf{r}\, n(\mathbf{r}) V_{\rm H}(\mathbf{r}) + E_{\rm xc}[n] - \int \mathrm{d}^3\mathbf{r}\, n(\mathbf{r}) V_{\rm xc}(\mathbf{r}) + E_{II}. \tag{1.37}$$

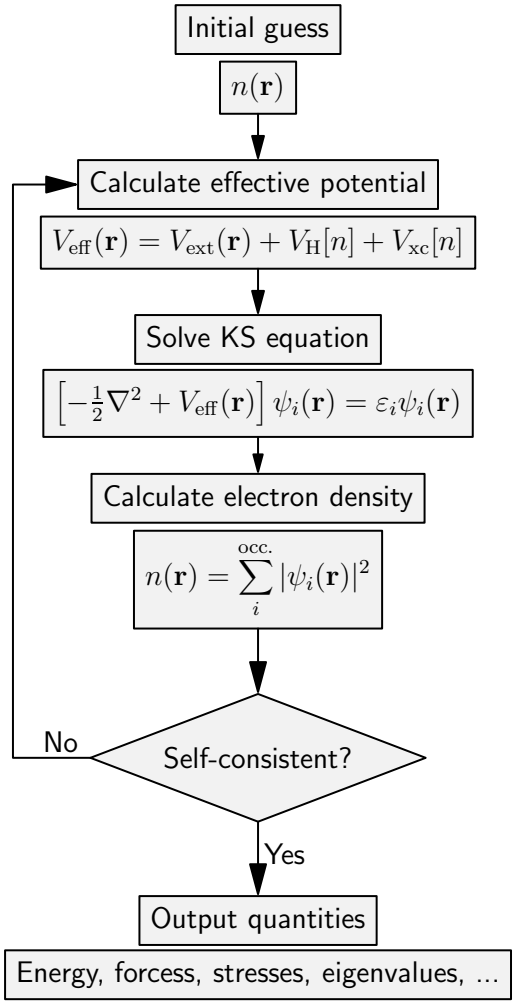

Figure 1.2: Schematic representation of the self-consistent method for solution of Kohn-Sham equations.

At this point, we need to provide a feasible approximation for $E_{\text{xc}}[n]$. Roughly, by their construction, there are two types of XC functionals:

- *non-empirical*, which are constructed to satisfy the known exact conditions (such as *sum rules*[30]) and usually have systematic failures (and successes!) so their reliability for calculations of basic physical properties (lattice constants, cohesive energies, band gaps etc.) can often be predicted. These functionals are mostly used in condensed matter physics and will be used in this thesis as well;

- *(semi-)empirical*, whose parameters are fitted to experimental data obtained for the extensive sets of atoms and molecules[31] or data generated by other first-principle methods, e.g. wavefunction-based methods.[12] The aim of these

[12]These are usually refered to as post-Hartree-Fock methods [32]. They are considered highly

functionals is to best reproduce a set of reference values. Hence, they are specialized for particular tasks and their usability is confined to the types of data used for their construction.

There are plenty of developed functionals of both kinds and the number is still growing. Bearing in mind the variety of XC functionals, we will devote the next section to the non-empirical XC functionals which are used for calculations in this thesis.

1.4 Exchange-correlation functionals

One of the great advantages of the Kohn-Sham approach lies in the expression for the total energy functional – it separates the independent particle kinetic energy $T_s[n]$ and the long-range $E_{\mathrm{H}}[n]$ from the term which encompasses all the many-body effects, that is the exchange-correlation energy $E_{\mathrm{xc}}[n]$. This convenience gives the possibility for the $E_{\mathrm{xc}}[n]$ to be reasonably approximated as a (semi-)local functional of the density.

1.4.1 Local density approximation (LDA)

There would be no practical use of DFT if it's not for the workable approximations for $E_{\mathrm{xc}}[n]$. The basic idea behind *the local density approximation* (LDA) comes from the properties of the interacting homogeneous electron gas, for which many aspects were known at the time when DFT was proposed as a new method for the electronic structure calculations. Generally, the true XC potential $V_{\mathrm{xc}}[n(\mathbf{r})]$ at point $\mathbf{r}$ depends not only on the local density $n(\mathbf{r})$ but also on the density at all other points $\mathbf{r}'$ in the system. If we ignore all the non-locality of $V_{\mathrm{xc}}[n(\mathbf{r})]$ and thus assume that it depends only on the local density $n(\mathbf{r})$, $E_{\mathrm{xc}}[n]$ can be written as

$$E_{\mathrm{xc}}^{\mathrm{LDA}}[n] = \int \mathrm{d}^3\mathbf{r}\, \epsilon_{\mathrm{xc}}[n] n(\mathbf{r}), \tag{1.38}$$

where $\epsilon_{\mathrm{xc}}[n] = \epsilon_{\mathrm{x}}[n] + \epsilon_{\mathrm{c}}[n]$ is the exchange-correlation energy per particle of the *homogeneous electron gas*. Stated in this form, it is just the usual *function* of density n. That is, within LDA we assume that at every point $\mathbf{r}$ the exchange-correlation energy per particle $\epsilon_{\mathrm{xc}}[n]$ is equal to that of the interacting homogeneous electron gas with density $n(\mathbf{r}) = n$. It is an extremely useful approach for systems with reasonably slowly varying spatial density $n(\mathbf{r})$, and it has been the most popular approximation in condensed matter physics for decades.

accurate, but computational cost undermines their usability.

From (1.38), the exchange-correlation potential $V_{\mathrm{xc}}[n(\mathbf{r})]$ defined in (1.34) becomes

$$V_{\mathrm{xc}}^{\mathrm{LDA}}(\mathbf{r}) = \frac{\delta E_{\mathrm{xc}}^{\mathrm{LDA}}}{\delta n(\mathbf{r})} = \epsilon_{\mathrm{xc}}[n(\mathbf{r})] + n(\mathbf{r})\frac{\mathrm{d}\epsilon_{\mathrm{xc}}[n(\mathbf{r})]}{\mathrm{d}n(\mathbf{r})} \tag{1.39}$$

Recalling the equation (1.37) we get the simple expression for total energy within LDA

$$E_{\mathrm{tot}}^{\mathrm{LDA}}[n] = \sum_{i}^{\mathrm{occ.}} \varepsilon_i - \frac{1}{2}\int \mathrm{d}^3\mathbf{r}\, n(\mathbf{r}) V_{\mathrm{H}}(\mathbf{r}) - \int \mathrm{d}^3\mathbf{r}\, n(\mathbf{r})\frac{\mathrm{d}\epsilon_{\mathrm{xc}}[n(\mathbf{r})]}{\mathrm{d}n(\mathbf{r})} n(\mathbf{r}) + E_{II}. \tag{1.40}$$

Usually ϵ_{xc} is expressed as a function of the dimensionless parameter r_s, called the *Wigner-Seitz radius*, which is the mean radius of the sphere that can be assigned to each electron in the system, so that the system volume is just the sum of the volumes of all these spheres. Similarly to density, it is a function of the spatial coordinates and it is defined by

$$r_s(\mathbf{r}) = \left(\frac{4\pi n(\mathbf{r})}{3}\right)^{-1/3}. \tag{1.41}$$

In LDA, the expression for exchange energy per particle is exact – as we are dealing with the homogeneous gas, so too can ϵ_{x} be calculated exactly within the HFA. Indeed, if we assume that we have interacting electrons in the uniform positive background, the HFA gives the dispersion relation for electrons,

$$\begin{aligned} \varepsilon(\mathbf{k}) &= \frac{1}{2}k^2 - \frac{k_F}{\pi} f(k/k_F), \\ f(x) &= 1 + \frac{1-x^2}{2x}\ln\left|\frac{1+x}{1-x}\right|, \end{aligned} \tag{1.42}$$

where $k_F = (2\varepsilon_F)^{1/2}$ is the Fermi wavevector. Integrating the expression (1.42) for all $k < k_F$ yields the total ground state energy of the system per electron

$$\epsilon_0 = \frac{1.105}{r_s^2} - \frac{0.458}{r_s}. \tag{1.43}$$

The first term in (1.43) is the kinetic energy and the second term is the exchange energy per particle of the homogeneous electron gas.[13] Therefore, in Hartree atomic units the exchange energy per particle of unpolarized homogeneous electron gas is

$$\epsilon_{\mathrm{x}}(r_s) = -\frac{0.458}{r_s} \tag{1.44}$$

Contrary to the exchange energy, no general form of correlation energy is known exactly, but the low-density ($r_s \gg 1$) and high-density ($r_s \ll 1$) limits can be

[13]For the complete derivation of the exchange energy within HFA, interested reader should look in [33], p. 334-336, while the thorough treatment of the homogeneous electron gas can be found in [25].

calculated analytically. In the low-density limit the electrostatic potential energy dominates the kinetic energy and electrons form a *Wigner lattice*[14] [34]. Though density in this case is not strictly uniform as electrons sit at the lattice points, we can still use the expression for the correlation energy of this system to estimate ϵ_c at low densities. In the high-density limit, the kinetic energy is the dominant one and thus the *random-phase approximation* (RPA) becomes exact[35]. The limiting factor is that real metals have $r_s \sim 2-6$, therefore neither of the limits can be used for the correlation energy of real systems. Usually, one needs to develop an interpolation scheme that joins the low- and high-density limits of ϵ_c. One of the most popular forms is by Perdew and Zunger [36], who have parametrized the numerical results obtained by Ceperley and Alder [37] with Monte Carlo calculations,

$$\epsilon_c(r_s) = \begin{cases} -0.1423/(1 + 1.0529\sqrt{r_s} + 0.3334 r_s) & \text{for } r_s \geq 1, \\ -0.0480 + 0.0311 \ln r_s - 0.0116 r_s + 0.0020 r_s \ln r_s & \text{for } r_s \leq 1. \end{cases}$$

LDA is, due to its simplicity and reasonably good results, still in use in condensed matter physics, but its popularity steeply declined with the development of the XC functionals which systematically include gradients of the density. The aim of the next section is to give a short description of the functionals of this kind.

1.4.2 Generalized gradient approximation (GGA)

The success of LDA has motivated further development of various functionals outside of the local approximation. The first step beyond LDA is to include the magnitude of the gradient of the density $|\nabla n|$ as well as the density itself at each point. This idea of *gradient expansion approximation* (GEA) was proposed already in the original work of Kohn and Sham [10], but the efforts in the following years led to no consistent improvement. On the contrary, the results obtained with GEA is often worse compared to LDA, and moreover GEA violates sum rules and some other relevant conditions [38]. One of the issues with GEA is that gradients in real materials are so large that the expansion breaks down.

For the reasons stated above, a variety of forms have been proposed for functionals that are dependent on the gradient of the density, but preserve the desired properties for large gradients. They have the common name *generalized gradient approximation* (GGA), and the exchange-correlation energy within GGA have a

[14] It is a *bcc* lattice in 3D, a triangular lattice in 2D and evenly spaced lattice in 1D.

general form

$$E_{\rm xc}^{\rm GGA}[n^\uparrow, n^\downarrow] = \int {\rm d}^3\mathbf{r}\, n(\mathbf{r})\epsilon_{\rm xc}(n^\uparrow, n^\downarrow, |\nabla n^\uparrow|, |\nabla n^\downarrow|, \ldots) = \\ = \int {\rm d}^3\mathbf{r}\, n(\mathbf{r})\epsilon_{\rm x}^{\rm hom}(n) F_{\rm xc}(n^\uparrow, n^\downarrow, |\nabla n^\uparrow|, |\nabla n^\downarrow|, \ldots) \tag{1.45}$$

where $F_{\rm xc}$ is dimensionless and $\epsilon_{\rm x}^{\rm hom}$ is the exchange energy of unpolarized electron gas given by (1.44). $E_{\rm xc}$ is expressed in terms of spin densities as most of the GGA functionals are given in the spin-polarized form. Nevertheless, it is easy to show the validity of the *spin-scaling relation*

$$E_{\rm x}[n^\uparrow, n^\downarrow] = \frac{1}{2}[E_{\rm x}[2n^\uparrow] + E_{\rm x}[2n^\downarrow]] \tag{1.46}$$

where $E_{\rm x}[n]$ is the exchange energy for an unpolarized gas of density $n(\mathbf{r})$. This is a great simplification, as we need to consider only the function $F_{\rm x}(n, |\nabla n|)$ for the spin-unpolarized system. The standard way to express this function is in terms of dimensionless reduced density of m-th order

$$s_m \stackrel{\rm def}{=} \frac{|\nabla^m n|}{(2k_F)^m n} = \frac{|\nabla^m n|}{2^m (3\pi^2)^{m/3} n^{(1+m/3)}}. \tag{1.47}$$

Recalling that $k_F = 3(2\pi/3)^{1/3} r_s^{-1}$, s_m is proportional to the mth-order fractional variation in density normalized to the parameter r_s.

The expansion of $F_{\rm x}$ up to the second-order terms has been calculated analytically [39, 40],

$$F_{\rm x} = 1 + \frac{10}{81} s_1^2 + \frac{146}{2025} s_2^2 + \ldots, \tag{1.48}$$

and moreover,

$$s_1 \equiv s = \frac{|\nabla n|}{2k_F n} = \frac{|\nabla r_s|}{2(2\pi/3)^{1/3} r_s}. \tag{1.49}$$

There are numerous forms for $F_{\rm x}(n, s)$, where $s = s_1$. We will give the parametrization of Perdew, Burke and Ernzerhof, the so-called PBE functional [41]. It is among the most popular GGA functionals and it has a conservative philosophy of GGA construction as it tries to retain all the correct features of LDA, while adding others. Thus, it is a systematical improvement over LDA and this is the main reason why we have used it for the majority of our calculations. The PBE functional of exchange is given by a simple form, chosen to satisfy $F_{\rm x}(0) = 1$ (and thus recover the local approximation) and to be constant at large s,

$$F_{\rm x}(s) = 1 + \kappa - \frac{\kappa}{1 + \mu s^2/\kappa}. \tag{1.50}$$

The value of $\kappa = 0.804$ is chosen to satisfy the Lieb-Oxford bound which provides the lower limit for XC energy

$$E_{\mathrm{xc}}[n] \geq 2.273 E_{\mathrm{x}}^{\mathrm{LDA}}[n]. \tag{1.51}$$

The value of $\mu = 0.21951$ recovers the linear response form of the LDA, i.e. it is chosen to cancel the term from the correlation. At first glance it is a strange choice, but it is made purposely and with this value of μ the results obtained with PBE functional agree very well with quantum Monte Carlo calculations.

As with LDA, the correlation part of XC functional is a more problematic one. It is expressed in terms of *spin polarization*, which is defined by

$$\zeta(\mathbf{r}) = \frac{n^{\uparrow}(\mathbf{r}) - n^{\downarrow}(\mathbf{r})}{n(\mathbf{r})}. \tag{1.52}$$

The form is chosen to satisfy several conditions, and can be expressed by

$$E_{\mathrm{c}}^{\mathrm{GGA-PBE}}[n^{\uparrow}, n^{\downarrow}] = \int \mathrm{d}^3\mathbf{r}\, n[\epsilon_{\mathrm{c}}^{\mathrm{hom}}(r_s, \zeta) + H(r_s, \zeta, t)] \tag{1.53}$$

where t is dimensionless gradient $t = |\nabla n|/(2\phi k_{TF} n)$, $k_{TF} = 0.815 k_F r_s^{1/2}$ is the Thomas-Fermi screening wavevector, $\phi = ((1+\zeta)^{2/3} + (1-\zeta)^{2/3})/2$ and

$$H(r_s, \zeta, t) = \gamma\phi^3 \ln\Big(1 + \frac{\beta}{\gamma} t^2 \frac{1 + At^2}{1 + At^2 + A^2 t^4}\Big), \tag{1.54}$$

where $\beta = 0.066725$ and $\gamma = 0.031091$. Finally, the function A is given by

$$A = \frac{\beta}{\gamma}\left[\exp\left(-\frac{\epsilon_{\mathrm{c}}^{\mathrm{hom}}}{\gamma\phi^3}\right) - 1\right]^{-1} \tag{1.55}$$

For a detailed description of the methodology behind the construction of PBE functional in the words of its creator we refer to [30].

To conclude this Chapter, we give some information about the improvement which GGA functionals bring over LDA. Properties such as bond dissociation energies are calculated to a high precision within GGA, with errors of the order of $\leq 10\%$, while the LDA may overestimate it by as much as 100%. With modern GGA XC functionals, atomic and molecular quantities can be calculated with nearly chemical accuracy. Before GGA this was only possible using the *configuration-interaction (CI)* schemes in which the true many-body wavefunction is expanded in some small set of Slater determinants composed of suitable atomic basis functions. As it is a wavefunction-based method, it is computationally expensive, thus GGA brought a great speedup in such calculations. Moreover, the GGA gives better results for bulk moduli of solids with an error of around 10%, compared to the typical error of 20%

of the LDA, and the PBE XC potential is only slightly more complicated than in the LDA, but it is still *multiplicative* potential, thus leading to simple single-particle equations with no extra computational cost. A cautionary note is that there is no guarantee that the GGA will be better than LDA for some specific calculation, but for calculations of quantities relevant for this thesis PBE is widely considered as a superior choice.

Chapter 2

Methods in electronic structure calculations

In order to describe the ground-state electronic properties, in Chapter 1 we have dealt with density functional theory, which provides an elegant way to replace the realistic system of interacting electrons with the effectively one-particle problem. To calculate the desired physical quantities, one needs to solve the Kohn-Sham equation in a chosen basis, thus obtaining the eigenvalues and eigenfunctions.[1] The choice of a suitable basis set is system specific, i.e. the basis set suitable for molecules usually is improper for solids. As we are interested in physical properties of the spatially periodic systems, this chapter is organized as follows: in the first part of the chapter we will explain the basics of electronic structure calculations of crystals, while the second part will be devoted to the general method for determination of electronic structure and the one used for calculations in this thesis – the projector augmented wave method.

2.1 Basics of electronic structure calculation

In practice, every DFT calculation starts with the preparation of the input files which contain the types of atoms that constitute the system together with their positions. Thus, we shall begin our discussion with the definition of crystal structure in real and reciprocal space and continue with its connection with the Fourier transform and plane wave basis set – the simplest basis set suitable for practical solution of the Schrödinger equation for electrons in crystals.

[1] In this chapter we discuss the solution of the time independent one-particle Schrödinger equation for electrons in crystals. Every conclusion drawn from this discussion stands also for the Kohn-Sham equation, as it is by its structure the Schrödinger-like one-particle equation.

2.1.1 Crystal structure and the Fourier transform

Crystal is defined as a highly ordered periodic structure completely specified by

- *the Bravais lattice* (BL) – a set of points in space, all of them connected by translation vectors $\mathbf{T}(n_1, n_2, n_3) = n_1\mathbf{a}_1 + n_2\mathbf{a}_2 + n_3\mathbf{a}_3$, where $n_i \in \mathbb{Z}$;
- *the basis* – the structural motif which is repeated along the lattice vectors, specified by types $A_1, A_2, \ldots, A_\nu$ and the positions $\{\mathbf{d}_1, \mathbf{d}_2, \ldots, \mathbf{d}_\nu\}$ of atoms attached to the crystal points.[2]

Three non-coplanar vectors $\{\mathbf{a}_1, \mathbf{a}_2, \mathbf{a}_3\}$ are called *primitive vectors*, and the parallelepiped formed by them is called *primitive cell*. Because of the underlined spatial periodicity, all the $\mathbf{r}$-dependent functions describing electronic properties (such as electron density) must be also periodic in space in the same way. Therefore, a general function defined in all the volume of the crystal Ω obeys strict conditions $f(\mathbf{r} + \mathbf{T}(n_1, n_2, n_3)) = f(\mathbf{r})$ for any combination of integers n_i. Such a periodic function can be represented by Fourier transform in terms of Fourier components at wavevectors $\mathbf{q}$ defined in a *reciprocal space*,

$$f(\mathbf{q}) = \frac{1}{\Omega}\int_\Omega \mathrm{d}^3\mathbf{r} f(\mathbf{r})\mathrm{e}^{\mathrm{i}\mathbf{q}\cdot\mathbf{r}}. \tag{2.1}$$

Due to spatial periodicity of the function $f(\mathbf{r})$, each Fourier component must satisfy Born-Von Karmen periodic boundary conditions in each of the dimensions, i.e. if $N_{\mathrm{cell}} = N_1 \times N_2 \times N_3$ is the number of cells in a crystal it must be fulfilled $\mathrm{e}^{\mathrm{i}\mathbf{q}\cdot N_i\mathbf{a}_i} = 1$ for $i = 1, 2, 3$. In other words, $\mathbf{q}$ is restricted to the set of vectors satisfying $\mathbf{q}\cdot\mathbf{a}_i = (2\pi \times \mathit{integer})/N_i$ for each of the primitive vectors $\mathbf{a}_i$. Thus, for functions with periodicity of the crystal lattice, every Fourier component must satisfy

$$\begin{aligned} f(\mathbf{q}) &= \frac{1}{\Omega}\sum_{n_1,n_2,n_3}\int_{\Omega_{\mathrm{cell}}} \mathrm{d}^3\mathbf{r} f(\mathbf{r})\mathrm{e}^{\mathrm{i}\mathbf{q}\cdot(\mathbf{r}+\mathbf{T}(n_1,n_2,n_3))} \\ &= \frac{1}{N_{\mathrm{cell}}}\sum_{n_1,n_2,n_3}\mathrm{e}^{\mathrm{i}\mathbf{q}\cdot\mathbf{T}(n_1,n_2,n_3)}\frac{1}{\Omega_{\mathrm{cell}}}\times\int_{\Omega_{\mathrm{cell}}}\mathrm{d}^3\mathbf{r} f(\mathbf{r})\mathrm{e}^{\mathrm{i}\mathbf{q}\cdot\mathbf{r}}, \end{aligned} \tag{2.2}$$

where $\Omega = N_{\mathrm{cell}}\Omega_{\mathrm{cell}}$. The sum over all lattice points in the last line of (2.2) vanishes for all $\mathbf{q}$ except those for which $\mathbf{q}\cdot\mathbf{T}(n_1, n_2, n_3) = 2\pi \times \mathit{integer}$ for *all* translations $\mathbf{T}$. Since $\mathbf{T}(n_1, n_2, n_3)$ is a sum of integer multiples of the primitive translations $\mathbf{a}_i$, it follows that $\mathbf{q}\cdot\mathbf{a}_i = 2\pi \times \mathit{integer}$. The set of vectors $\mathbf{q}$ in the reciprocal space that satisfy this condition is called *reciprocal lattice*. If we define three primitive vectors

[2] The term *basis*, referring to the structural motif of the crystal, should not be confused with the plane wave basis which we will use for the solution of the Schrödinger equation.

$\mathbf{b}_i$ of the reciprocal lattice, i.e. vectors that satisfy the conditions $\mathbf{a}_i \cdot \mathbf{b}_j = 2\pi\delta_{ij}$, we can represent vectors of the reciprocal lattice in this basis as $\mathbf{G}(m_1, m_2, m_3) = m_1\mathbf{b}_1 + m_2\mathbf{b}_2 + m_3\mathbf{b}_3$ where $m_i \in \mathbb{Z}$. Non-zero Fourier components are then given by $f(\mathbf{G}) = \frac{1}{\Omega_{\text{cell}}} \int_{\Omega_{\text{cell}}} \mathrm{d}^3\mathbf{r}\, f(\mathbf{r}) \mathrm{e}^{\mathrm{i}\mathbf{G}\cdot\mathbf{r}}$, where $\mathbf{G}$ are vectors of the reciprocal lattice. This is a great simplification which allows us to run calculations within an elementary cell only and obtain the function in the whole crystal by periodic extension.

2.1.2 Schrödinger equation in a plane wave basis

The independent particle Schrödinger equation for electrons in the effective periodic potential $V_{\text{eff}}(\mathbf{r} + \mathbf{T}(n_1, n_2, n_3)) = V_{\text{eff}}(\mathbf{r})$ is

$$\hat{H}_{\text{eff}}(\mathbf{r})\psi_i(\mathbf{r}) = \left[-\frac{1}{2}\nabla^2 + V_{\text{eff}}(\mathbf{r}) \right] \psi_i(\mathbf{r}) = \varepsilon_i \psi_i(\mathbf{r}). \tag{2.3}$$

In crystals it is convenient to require that the wavefunctions obtained as a solution to (2.3) are normalized within the volume of the crystal Ω. As any periodic function can be expanded in the complete set of Fourier components, wavefunction that is the solution to (2.3) can be written as

$$\psi_i(\mathbf{r}) = \sum_{\mathbf{q}} c_{i,\mathbf{q}} \times \frac{1}{\sqrt{\Omega}} \mathrm{e}^{\mathrm{i}\mathbf{q}\cdot\mathbf{r}} \equiv \sum_{\mathbf{q}} c_{i,\mathbf{q}} \left|\mathbf{q}\right\rangle, \tag{2.4}$$

where $c_{i,\mathbf{q}}$ are the expansion coefficients of the wavefunction in the basis of orthonormal plane waves $|\mathbf{q}\rangle$ satisfying $\langle \mathbf{q}'|\mathbf{q}\rangle = \frac{1}{\Omega}\int_\Omega \mathrm{d}^3\mathbf{r}\, \mathrm{e}^{-\mathrm{i}(\mathbf{q}'-\mathbf{q})\cdot\mathbf{r}} = \delta_{\mathbf{q},\mathbf{q}'}$. Using the orthonormality conditions and inserting (2.4) into (2.3), multiplying from the left by $\langle \mathbf{q}'|$ and integrating in the real space lead us to the Schrödinger equation in Fourier space,

$$\sum_{\mathbf{q}} \langle \mathbf{q}'|\hat{H}_{\text{eff}}|\mathbf{q}\rangle\, c_{i,\mathbf{q}} = \varepsilon_i c_{i,\mathbf{q}}. \tag{2.5}$$

The matrix elements of the kinetic energy operator are simply

$$\langle \mathbf{q}'| -\frac{1}{2}\nabla^2 |\mathbf{q}\rangle = \frac{1}{2}|q|^2 \delta_{\mathbf{q},\mathbf{q}'}. \tag{2.6}$$

Potential $V_{\text{eff}}(\mathbf{r})$, due to its periodicity, can be represented in a plane wave basis as $V_{\text{eff}}(\mathbf{r}) = \sum_m V_{\text{eff}}(\mathbf{G}_m)\mathrm{e}^{\mathrm{i}\mathbf{G}_m\cdot\mathbf{r}}$, where $\mathbf{G}_m$ are the reciprocal lattice vectors and $V_{\text{eff}}(\mathbf{G}_m)$ is the Fourier component of the potential. Thus, the matrix elements of the potential

$$\langle \mathbf{q}'|V_{\text{eff}}|\mathbf{q}\rangle = \sum_m V_{\text{eff}}(\mathbf{G}_m)\delta_{\mathbf{q}'-\mathbf{q},\mathbf{G}_m}, \tag{2.7}$$

are non-zero only if $\mathbf{q}$ and $\mathbf{q}'$ differ by some reciprocal lattice vector $\mathbf{G}_m$.

Now we came to the point - if we define $\mathbf{q} = \mathbf{k} + \mathbf{G}_m$ and $\mathbf{q}' = \mathbf{k} + \mathbf{G}_{m'}$ (which differ by a reciprocal lattice vector $\mathbf{G}_{m''} = \mathbf{G}_m - \mathbf{G}_{m'}$) the Schrödinger equation for any given $\mathbf{k}$ within the reciprocal cell can be written as the matrix equation,

$$\sum_{m'} H_{mm'}(\mathbf{k}) c_{i,m'}(\mathbf{k}) = \varepsilon_i(\mathbf{k}) c_{i,m}(\mathbf{k}), \tag{2.8}$$

where

$$H_{mm'}(\mathbf{k}) = \langle \mathbf{k} + \mathbf{G}_m | \hat{H}_{\text{eff}} | \mathbf{k} + \mathbf{G}_{m'} \rangle = \frac{1}{2} |\mathbf{k} + \mathbf{G}_m|^2 \delta_{mm'} + V_{\text{eff}}(\mathbf{G}_m - \mathbf{G}_{m'}). \tag{2.9}$$

In (2.8) we labeled with $i = 1, 2, \ldots$ distinct eigenvalues and eigenfunctions. For the complete solution of the Schrödinger equation (2.3) we need to solve the matrix equation (2.8) for every k-point in the reciprocal cell. More details about the importance of the operations in k-space[3] can be found in the following subsections.

2.1.3 The Bloch theorem and electron bands

The concept of electron bands in crystals can be formulated with the help of a simple but profound *Bloch theorem* [42]. The connection between Bloch theorem and Fourier transform and the role of k-space in the electronic structure calculations is explained in this subsection.

Each eigenfunction of the Schrödinger equation (2.8) labeled with index i for a given $\mathbf{k}$ can be written as a linear combination of plane waves with wavevectors restricted to $\mathbf{q} = \mathbf{k} + \mathbf{G}_m$, i.e.

$$\psi_{i,\mathbf{k}}(\mathbf{r}) = \sum_m c_{i,m}(\mathbf{k}) \times \frac{1}{\sqrt{\Omega}} \mathrm{e}^{\mathrm{i}(\mathbf{k}+\mathbf{G}_m)\cdot\mathbf{r}} \equiv \mathrm{e}^{\mathrm{i}\mathbf{k}\cdot\mathbf{r}} \frac{1}{\sqrt{N_{\text{cell}}}} u_{i,\mathbf{k}}(\mathbf{r}), \tag{2.10}$$

where

$$u_{i,\mathbf{k}}(\mathbf{r}) = \frac{1}{\sqrt{\Omega_{\text{cell}}}} \sum_m c_{i,m}(\mathbf{k}) \mathrm{e}^{\mathrm{i}\mathbf{G}_m\cdot\mathbf{r}}, \tag{2.11}$$

are functions with the periodicity of Bravais lattice, $u_{i,\mathbf{k}}(\mathbf{r} + \mathbf{T}(n_1, n_2, n_3)) = u_{i,\mathbf{k}}(\mathbf{r})$ for any translation through lattice vector $\mathbf{T}(n_1, n_2, n_3)$. The Bloch theorem, given in (2.10), states that any eigenfunction is a product of $\mathrm{e}^{\mathrm{i}\mathbf{k}\cdot\mathbf{r}}$ and a periodic function with the periodicity of a crystal lattice. For $\psi_{i,\mathbf{k}}(\mathbf{r})$ to be orthonormal over the volume of the crystal Ω, $u_{i,\mathbf{k}}(\mathbf{r})$ must be orthonormal in one primitive cell

$$\frac{1}{\Omega_{\text{cell}}} \int_{\Omega_{\text{cell}}} \mathrm{d}^3\mathbf{r}\, u^*_{i,\mathbf{k}}(\mathbf{r}) u_{i',\mathbf{k}}(\mathbf{r}) = \sum_m c^*_{i,m}(\mathbf{k}) c_{i',m}(\mathbf{k}) = \mathbf{c}_i(\mathbf{k})^T \cdot \mathbf{c}_{i'}(\mathbf{k}) = \delta_{ii'}. \tag{2.12}$$

In (2.10) the states of electron in a periodic potential are labeled with index i and wavevector $\mathbf{k}$. The possibility to label different states by a well-defined $\mathbf{k}$ means

[3] The terms reciprocal space, k-space and Fourier space are used synonymously.

that $\mathbf{k}$ is a conserved quantity, but since it is indistinguishable from any wavevector $\mathbf{k}' = \mathbf{k} + \mathbf{G}$ where $\mathbf{G}$ is a vector of the reciprocal cell, we can only say that $\mathbf{k}$ is conserved modulo addition of any reciprocal lattice vector. Hence, analogous to the momentum in free space, the conserved quantity in crystals is called *crystal momentum*.

Due to Born-Von Karmen boundary conditions, the number of allowed wavevectors in a primitive cell is equal to the number of cells in the crystal. In macroscopic samples, this number is so large ($\sim 10^{23}$) that we don't need to bother about whether a particular k-point is allowed or not. Hence, in the limit of large volume Ω the k-points become dense continuum and consequently $\varepsilon_i(\mathbf{k})$ become continuous *bands*, labeled with a band index i. Finally, at each $\mathbf{k}$ there is a discrete set of eigenstates labeled with band index which may be found by diagonalizing the hamiltonian (2.9) in the basis of discrete Fourier components $\mathbf{k} + \mathbf{G}_m$, $m = 1, 2, \ldots$.

2.1.4 Integration of functions over the Brillouin zone

In order to solve (2.8) we need to give the answers to a few questions:

- how to choose the reciprocal cell, as the choice is not unique?
- how to use the symmetry of the crystal to reduce the calculations?
- how to divide the chosen reciprocal cell into a grid of k-points?

First, let us define *the Wigner-Seitz cell* as a region of space around lattice point that is closer to that point than to any other. It can be constructed by bisecting with perpendicular planes the vectors joining this lattice point with its nearest neighbors. Since there is nothing in the definition of the Wigner-Seits cell that refers to any particular choice of primitive vectors, this cell will maintain the full symmetry of the Bravais lattice. This brings us to the concept of *the first Brillouin zone* (BZ), which is the Wigner-Seits cell of the reciprocal lattice. It is unique among primitive cells because its boundaries are the bisecting planes of the $\mathbf{G}$ vectors where Bragg scattering occurs. Inside the BZ there are no such boundaries, thus the bands must be continuous and analytical inside the zone.

The full symmetry group of a BL – *the space group* – is composed of (1) the translations $\mathbf{T}(n_1, n_2, n_3)$ through lattice vectors and (2) *the point group* $\{R_n; n = 1, \ldots N_{\mathrm{PG}}\}$, i.e. a group of operations that are leaving at least one lattice point fixed – rotations, inversions, reflections and their combinations. Every symmetry operation of BL can be constructed by a successive applications of the operations of these two kinds. Crystal structures whose space group is a semi-direct product of the translational subgroup with the point group are called *symmorphic*, and we shall

largely confine our attention to the crystals of this kind.[4] By application of point group symmetry operators, the calculations can be magnificently reduced since all information can be found from states with $\mathbf{k}$ in *the irreducible Brillouin zone* (IBZ) [45]. The values of functions for the rest of k-points in the BZ can be reconstructed from their values inside IBZ with the point group symmetry operations. The action of symmetry operators R_n on the wavefunction can be stated as

$$R_n\psi_{i,\mathbf{k}}(\mathbf{r}) = \psi_{i,R_n\mathbf{k}}(R_n\mathbf{r}) = \psi_{i,\mathbf{k}}(\mathbf{r}); \quad \text{or} \quad \psi_{i,R_n^{-1}\mathbf{k}}(\mathbf{r}) = \psi_{i,\mathbf{k}}(R_n\mathbf{r}). \tag{2.13}$$

If $R_n^{-1}\mathbf{k}$ leads to a distinguishable k-point, then (2.13) shows that the states at $R_n^{-1}\mathbf{k}$ can be generated from those at $\mathbf{k}$ and the corresponding eigenvalues must be equal, $\varepsilon_i(R_n^{-1}\mathbf{k}) = \varepsilon_i(\mathbf{k})$. In all crystals BZ can always be reduced by at least a factor of 2 using relation of states at $\mathbf{k}$ and $-\mathbf{k}$. For example, simple cubic crystal has 48 point symmetry operations and its IBZ is just 1/48 the total BZ. The larger the point group, the greater the reduction of calculations.

For many quantities describing electronic structure of materials, such as total energy, electron density and number of electrons in bands, density of states (DOS) etc., it is necessary to sum (integrate) over $\mathbf{k}$ throughout the BZ. Hence, to find some intrinsic property of a crystal to which we refer as "per unit cell", we need to sum over values of $\mathbf{k}$ and divide the result with the number of values N_k. For a general function $f_i(\mathbf{k})$ the average value per cell becomes

$$\bar{f}_i = \frac{1}{N_k}\sum_{\mathbf{k}} f_i(\mathbf{k}) \to \frac{\Omega_{\text{cell}}}{(2\pi)^3}\int_{\text{BZ}} \mathrm{d}^3\mathbf{k}\, f_i(\mathbf{k}), \tag{2.14}$$

where $(2\pi)^3/\Omega_{\text{cell}}$ is the volume of the BZ [5], where we replaced the sum with an integral as the k-points are dense enough in the limit of large crystal volume to validate this conversion.

Integration over the full BZ can be reduced to the integration over only the IBZ with the help of symmetry. If we define *the weight* $w_{\mathbf{k}}$ to be the number of k-points in full BZ related by symmetry operations to the given k-point in IBZ (including the point in the IBZ) divided by the total number N_k of k-points in BZ, the sum in (2.14) becomes equivalent to

$$\bar{f}_i = \sum_{\mathbf{k}}^{\text{IBZ}} w_{\mathbf{k}} f_i(\mathbf{k}). \tag{2.15}$$

[4] However, as a general crystal structure is composed of a BL and a basis, in cases when dimensions of the basis are in a special relation to the primitive vectors there exist additional *non-symmorphic* operations which are taking the structure into itself, namely: *screw axes* and *glide planes*. For the pedagogical treatment of the group theory in solid state physics we refer to the textbooks [33, 43] and [44] for truly interested reader.

[5] For 2D crystals it is $(2\pi)^2/S_{\text{cell}}$.

Quantities such as electron density can always be written as

$$n(\mathbf{r}) = \frac{1}{N_k}\sum_{\mathbf{k}} n_{\mathbf{k}}(\mathbf{r}) = \frac{1}{N_{\mathrm{PG}}}\sum_{R_n}\sum_{\mathbf{k}}^{\mathrm{IBZ}} w_{\mathbf{k}} n_{\mathbf{k}}(R_n\mathbf{r}). \tag{2.16}$$

To calculate these quantities in k-space, one needs to accurately replace analytical integral in BZ with a sum on a chosen grid used in numerical integration.[6] This is a problem specific to the material under study and depends upon having sufficient points in regions where the integrand varies rapidly. In this respect, the key division of crystal structures is between *insulators* and *metals*.

Insulators have filled bands that can be integrated using only a few *special points* [46]. Since the integrand $f_i(\mathbf{k})$ is a function of $\psi_{i,\mathbf{k}}$ and $\varepsilon_i(\mathbf{k})$ and for insulators the sum (2.14) is over filled bands, it is a smoothly varying periodic function of $\mathbf{k}$. Therefore, it can be expanded in Fourier components

$$f_i(\mathbf{k}) = \sum_{\mathbf{T}} f_i(\mathbf{T})\mathrm{e}^{\mathrm{i}\mathbf{k}\cdot\mathbf{T}}, \tag{2.17}$$

where $\mathbf{T}$ are the lattice vectors. The most important point is that the contribution of the rapidly varying terms at large $\mathbf{T}$ decreases exponentially, so that the infinite sum (2.17) can be truncated to a finite sum. Monkhorst and Pack [47] proposed a general method for the division of BZ into a uniform grid of points determined by a simple formula valid for any crystal,

$$\mathbf{k}_{n_1,n_2,n_3} = \sum_{i=1}^{3} \frac{2n_i - N_i - 1}{2N_i}\mathbf{b}_i, \tag{2.18}$$

where $\mathbf{b}_i$ are the primitive vectors of the reciprocal lattice and N_i are the dimensions of the grid. The larger the dimensions of the grid, the finer and more accurate are the sampling. If N_i are even, the set does not include the highest symmetry points, i.e. it misses the Γ point ($\mathbf{k} = 0$) and the points on the BZ boundary. Moreover, this grid has a nice property that it exactly integrates a periodic function that has Fourier components which extend only to $N_i\mathbf{a}_i$ in each direction.

On the contrary to insulators, metals present difficulties when integrating the states that are close to the Fermi surface, which plays a special roll in many of their properties, as the Fermi function shows sharp variation from unity to zero as a function of $\mathbf{k}$. In order to represent the Fermi surface *the tetrahedron method* is widely used [48]. In this method IBZ is divided into a set of tetrahedra whose corners are taken to be the grid points. This is a particularly convenient as the proper choice

[6] Number of grid points in BZ should not be confused with the number N_k of allowed values of k-points in the BZ.

of tetrahedra can fill all the space for any grid, e.g. an irregular grid that has more points near the Fermi surface and fewer of them far from the Fermi surface where high accuracy is not needed. Furthermore, with the arrangement of tetrahedra that avoids the misweighting of k-points, this method maps exactly to the special-points scheme of Monkhorst and Pack [49, 50]. Matrix elements and eigenvalues are obtained for the k-points on the corners of tetrahedra and the integration for each tetrahedron is performed analytically, after interpolating eigenvalues and matrix elements inside the tetrahedron. The tetrahedron method is improved by Blöchl [51] and it is widely implemented in DFT codes.

2.1.5 Calculation of electron density

As an example how the real space and the reciprocal space are intertwined in the electronic structure calculations, we shall briefly present the main procedures in the calculation of the electron density.

The electron density in a crystal can be written as

$$n(\mathbf{r}) = \frac{1}{N_k} \sum_{\mathbf{k},i} f(\varepsilon_i(\mathbf{k})) n_{i,\mathbf{k}}(\mathbf{r}), \tag{2.19}$$

where $n_{i,\mathbf{k}}(\mathbf{r}) = |\psi_{i,\mathbf{k}}(\mathbf{r})|^2$ and $f(\varepsilon_i(\mathbf{k}))$ is the Fermi function. For a plane wave basis, from (2.10) we get

$$n_{i,\mathbf{k}}(\mathbf{r}) = \frac{1}{\Omega} \sum_{m,m'} c^*_{i,m}(\mathbf{k}) c_{i,m'}(\mathbf{k}) \mathrm{e}^{\mathrm{i}(\mathbf{G}_{m'} - \mathbf{G}_m)\cdot\mathbf{r}}, \tag{2.20}$$

and

$$n_{i,\mathbf{k}}(\mathbf{G}) = \frac{1}{\Omega} \sum_{m} c^*_{i,m}(\mathbf{k}) c_{i,m''}(\mathbf{k}), \tag{2.21}$$

where m'' denotes the $\mathbf{G}$ vector for which $\mathbf{G}_{m''} = \mathbf{G}_m + \mathbf{G}$. As stated in the previous subsections, the point group symmetry operations R_n of the crystal can be used to find density in real $n(\mathbf{r})$ and reciprocal space $n(\mathbf{G})$ in terms of the k-points in the IBZ only.

The representation of electron density in Fourier space (2.21) is intuitively clear but to calculate it straightforwardly using (2.21) is far from efficient. This expression involves a double sum, i.e. a convolution in Fourier space that requires N_G^2 operations, where N_G is the number of $\mathbf{G}$ vectors needed to describe the density. For large systems this becomes particularly expensive. On the other hand, if the Bloch states are known in real space on a grid of N_R points, the density can be found as a square of this states in N_R operations. This procedure involves the usage of *fast Fourier transform* (FFT) to convert density from one space to another in $N \log N$

operations, where $N = N_R = N_G$. The density in real space $n(\mathbf{r})$ is needed to find potentials, e.g. $\epsilon_{\text{xc}}(\mathbf{r})$ and $V_{\text{xc}}(\mathbf{r})$, and $n(\mathbf{G})$ can be used for solving the Poisson equation in Fourier space, thus the expressions for density in both spaces are used at some point during calculations. Cautionary note for the calculation of density is that it requires Fourier components that extend twice as far in each direction as those needed for the wavefunction ψ as their relation is $n \propto |\psi|^2$. Also, the FFT requires a regular grid in the form of a parallelepiped, whereas the wavefunction cutoff is usually expressed as a sphere with $(1/2)|\mathbf{k}+\mathbf{G}|^2 < E_{\text{cutoff}}$. For that reasons the number of points in the FFT grid for density is roughly an order of magnitude larger than the number of $\mathbf{G}$ vectors in the basis of the wavefunction. Nevertheless, the FFT approach is much more efficient for large systems since the number of operations scale as $N \log N$.

As we stated in Chapter 1, within the DFT approach to electronic structure of materials one has to determine the ground state electron density, which is calculated by solving the KS equations self-consistently (see Fig. 1.2). During this procedure, the input density of the $(m+1)$-th cycle is constructed from the output density of the m-th cycle. Using solely the output density from the current interation as the input density for the next iteration would lead to numerical issues and violate the SCF procedure. Hence, the input density of the $(m+1)$-th iteration, $n_{\text{in}}^{(m+1)}(\mathbf{r})$, is constructed as a mixture of density $n_{\text{out}}^{(m)}(\mathbf{r})$ and $n_{\text{in}}^{(m)}(\mathbf{r})$. The simplest approach is *linear mixing* which estimates an improved density input $n_{\text{in}}^{(m+1)}(\mathbf{r})$ at step $(m+1)$ as a linear combination of $n_{\text{in}}^{(m)}(\mathbf{r})$ and $n_{\text{out}}^{(m)}(\mathbf{r})$ with fixed coefficients

$$n_{\text{in}}^{(m+1)}(\mathbf{r}) = \alpha n_{\text{out}}^{(m)}(\mathbf{r}) + (1-\alpha) n_{\text{in}}^{(m)}(\mathbf{r}) \tag{2.22}$$

where $\alpha \sim 0.01 - 0.1$.

More advanced methods use the Jacobian $\mathcal{J}$ (the second derivative matrix) of the system and build up the information upon it as the iterations proceed. One of the most popular methods is *the Broyden method* [52, 53, 54], which starts with the approximate form of the inverse Jacobian $\mathcal{J}^{-1}$ and improves it in each iteration by making the change in density for the next step be in a direction orthogonal to directions of the last couple (~ 10) iterations. The computational cost of Broyden method is similar to that of linear mixing, but the speedup of the iterative procedure is considerable. Self-consistence is achieved when the input and output densities differ less then some predefined value. Finally, the output density of the last iteration is the ground state electron density.

2.2 Numerical representation of wavefunction

The question of an accurate representation of one-particle wavefunctions is so profound that it has stimulated the development of completely different methodologies in the electronic structure calculations. This particular task is followed by various numerical difficulties, the origin of which lies in the different behavior of the wavefunctions in the diverse regions of the system.

In the *atomic regions* (near the nucleus) the kinetic energy of electrons is large, resulting in rapid oscillations of the wavefunctions and consequently for an accurate numerical representation fine grids are required. On the other hand, large kinetic energy makes the Schrödinger equation insensitive to the changes of chemical environment. Therefore, the wavefunction in the atomic region can be accurately represented by a small set of atomic-like orbitals. Electrons with well localized wavefunctions within this region are called *core* electrons.

The opposite situation is to be found in the region between the atoms – the so-called *interstitial* or *bonding region* – where the kinetic energy of electrons is small and the wavefunctions are smooth, but they respond strongly to the changes of chemical environment. In this region the wavefunctions can be represented with a comparably small plane wave basis set. Such behavior are characteristic for the *valence* wavefunctions, which are responsible for chemical bonds in molecules and the construction of the electronic bands in solids. Difference between the core and valence states are sketched in Fig. 2.1.

Thus, one needs to perceive the behavior of wavefunctions in both regions and construct the appropriate basis for their representation in practical calculations. Based on a question whether the calculations explicitly include all the electrons in the system, these methods can be divided into two groups:

- **all-electron methods**
- **pseudopotentials**

2.2.1 All-electron methods

All-electron methods explicitly include all electrons, core and valence, in the calculation of the electronic wavefunction and density. They are the most general numerical methods for the precise solution of the Schrödinger equation.

The basic idea behind these methods is to divide the electronic structure problem to properly represent the rapid oscillations of wavefunctions near each nucleus in the system as well as its smooth part in the bonding region. Therefore, the smooth functions are *augmented* near each nucleus by solving the Schrödinger equation in

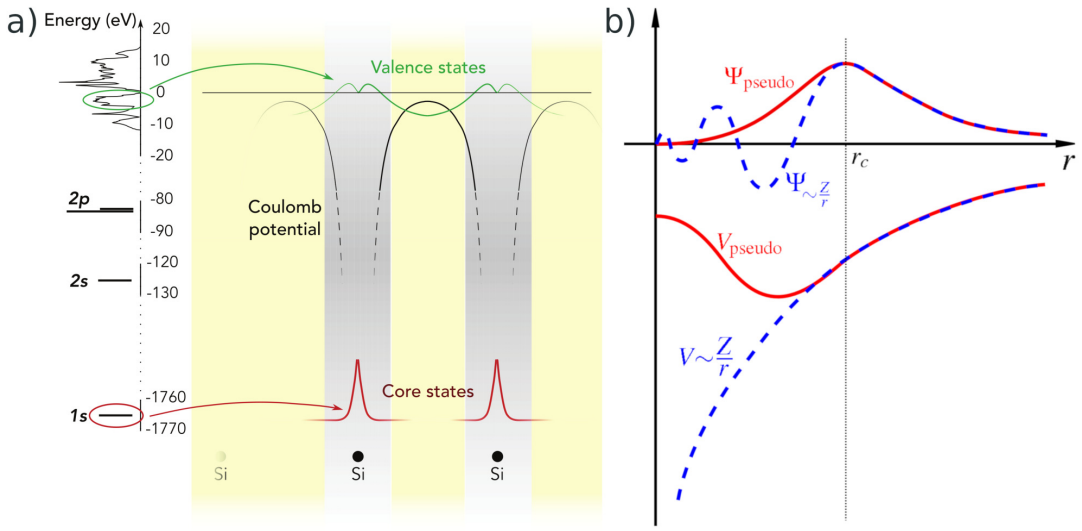

Figure 2.1: Electronic states in solid silicon. The valence states are delocalized over the crystal (green line) as the wavefunctions from neighboring atoms overlap. The lowest-energy 1*s* state (red) is at an energy two orders of magnitude lower than the valence states and is strongly localized near the nucleus, with no overlap between the atoms. The gray regions around the atoms indicate where the wavefunction, density and potential are smoothed in pseudized methods. From [55]. b) Comparison of a wavefunction in the Coulomb potential of the nucleus (blue) to the one in the pseudopotential (red). The real and the pseudo wavefunction and potentials match above a certain cutoff radius r_c (source: www.wikipedia.org/wiki/Pseudopotential).

the sphere at each energy and matching to the outer wavefunction. The idea of space division was originally proposed by Slater [56] for calculation of wavefunctions in a periodic potential. The resulting *augmented plane wave method* (APW) was later modified within Green's function formalism into *Korringa-Kohn-Rostocker method* (KKR) [57, 58]. They approached the electronic structure as a scattered-electron problem where an electron beam traveling through solid is represented as a plane wave. If for some energy the scattered waves interfere destructively a bound state has been determined. This approach can be translated to a basis set method with energy and potential dependent basis functions. Accordingly, a model potential had to be chosen: the so-called *muffin-tin potential* approximates the true potential by a constant in the interstitial region and by a spherically symmetric potential in the atomic regions. This lead to a *muffin-tin orbitals* (MTO) approach, which was initially proposed by Andersen [59] as a method suited to provide a satisfying interpretation of the electronic structure of solids (e.g. canonical bands) in terms of a minimal basis of orbitals, but it subsequently extended into a new methodology.

Augmented wave methods became practically applicable with an important modification due to Andersen [60], who showed that the energy-dependent basis set of

Slater's APW method can be mapped onto one with energy independent basis functions, by *linearizing* the partial waves for the atomic regions in energy. The APW equations are more difficult than the usual independent-particle equations that are linear in energy, such as (2.8), where all the eigenvalues and eigenvectors can be obtained with a single diagonalization.

The APW effective potential depends upon the logarithmic derivatives that are functions of energy $\varepsilon = \varepsilon_{i,k}$ which are not known in advance and must be calculated for each band separately. This requires the computationally demanding procedure of "root tracing" of the energy-dependent characteristic polynomial of the APW equation. Andersen's approach circumvent this procedure by the replacement of the original APW problem with the energy independent eigenvalue problem that can be solved with standard numerical techniques. Thus, the "L" method has been obtained, that make use of linearization of the equations around reference energies. The *linearized augmented plane wave method* (LAPW) is widely considered as the one that can provide the most precise solutions of the KS equations. Moreover, the results obtained with LAPW method serve as a golden standard for most of the DFT benchmark calculations, as well as for the construction of pseudopotentials.

2.2.2 Pseudopotentials

In the *pseudopotential* approach, only the valence electrons are explicitly included in the calculation and the repulsion of the core electrons is described with an effective potential together with the Coulomb attraction of the nucleus. Two main reasons have motivated the introduction of pseudopotentials: one is to avoid the explicit description of core electrons and the other is to eliminate the rapid oscillations of the wavefunction near the nucleus, which normally requires either complicated or large basis set (usually both).

We will describe the very basics of the algorithm for the construction of pseudopotentials. The first step is an all-electron atomic DFT calculation (usually in LDA) in spherical approximation for a chosen electronic configuration,

$$-\frac{1}{2}\frac{\mathrm{d}^2}{\mathrm{d}r^2} r\psi_{nl}(r) + \left[\frac{l(l+1)}{2r^2} + V_{\mathrm{eff}}(r) - \varepsilon_{nl}\right] r\psi_{nl}(r) = 0 \tag{2.23}$$

where $V_{\mathrm{eff}}(r) = -Z/r + V_{\mathrm{H}}([n];r) + V_{\mathrm{xc}}([n];r)$. After the inspection of determined eigenvalues and wavefunctions, one divides the electrons into core and valence (see Fig 2.1a) and choose the cutoff radius. The cutoff radius r_c can be different for each l and should be larger than the radial coordinate of the outermost node of the radial wavefunction. Then for each l, the pseudo wavefunction is constructed in a way that

it matches the all-electron wavefunction outside the cutoff radius r_c and be equal to some reasonable model function inside the core region, i.e.

$$\tilde{\psi}_l(r) = \begin{cases} f_l(r; \{\lambda_i\}) & \text{for} \quad r < r_c \\ \psi_l(r) & \text{for} \quad r > r_c. \end{cases}$$

The set of adjustable parameters $\{\lambda_i\}$ are obtained either by fitting to experimental data (atomic spectroscopic data for outer electrons, electron-atom cross sections etc.) or are determined *ab-initio* to mimic the valence properties calculated for the isolated atom. The freedom of choice for the function $f_l(r; \{\lambda_i\})$ is limited by the imposed conditions. The list of such requirements is given by Hamann, Schluter and Chiang (HSC) [61] for the construction of "good" ab-initio norm-conserving pseudopotential:

1. all-electron and pseudo valence eigenvalues agree for the chosen reference electron configuration;

2. all-electron and pseudo valence wavefunctions match beyond a chosen cutoff radius r_c;

3. the logarithmic derivatives of the all-electron and pseudo wavefunctions agree at r_c;

4. the integrated charge inside the core region for each pair of all-electron/pseudo wavefunctions agrees. This is the direct consequence of the norm-conservation;

5. the first derivative with respect to energy of the logarithmic derivatives of the all-electron and pseudo wavefunctions agrees at r_c.

Pseudo wavefunctions of silicon for two distinct electron configurations are presented in Fig. 2.2a.

The next step is the reconstruction of the potential which corresponds to the pseudo wavefunction, i.e. the so-called *inversion* of Schrödinger equation,

$$\tilde{V}_l^{\mathrm{scr}}(r) = \varepsilon_l - \frac{l(l+1)}{2r^2} + \frac{1}{2r\tilde{\psi}_l(r)} \frac{\mathrm{d}^2[r\tilde{\psi}_l(r)]}{\mathrm{d}r^2}. \tag{2.24}$$

This approach is always applicable if pseudo wavefunction is nodeless. The obtained pseudopotential is *screened*, i.e. it contains the Hartree and XC contribution of valence electrons. Thus, the final step is the removal of these contributions – the *unscreening* of pseudopotential,

$$\tilde{V}_l(r) = \tilde{V}_l^{scr}(r) - V_{\mathrm{H}}([\tilde{n}]; r) - V_{\mathrm{xc}}([\tilde{n}]; r). \tag{2.25}$$

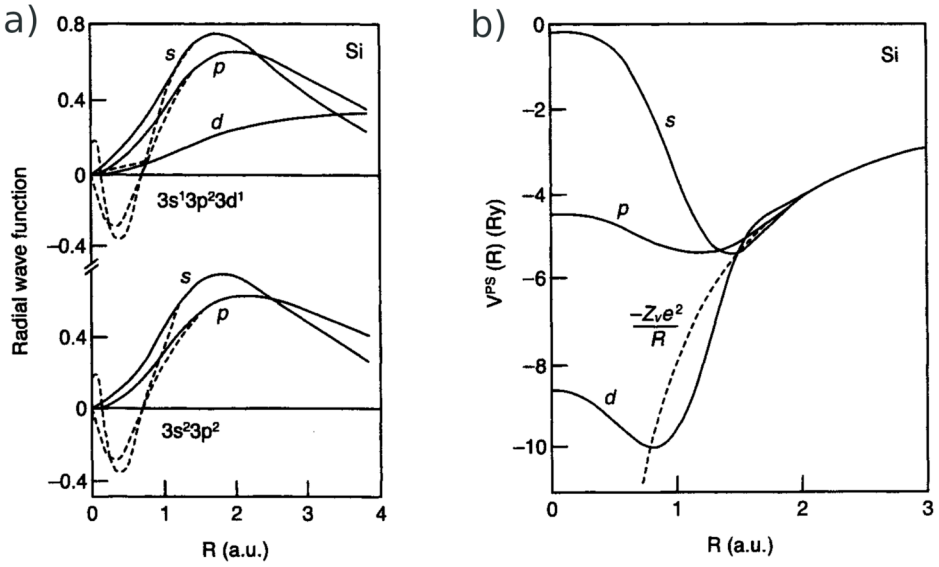

Figure 2.2: a) Comparison of the pseudo wavefunction (solid lines) and the corresponding all-electron wavefunctions (dashed lines) for the electron configurations $3s^2 3p^2$ and $3s^1 3p^2 3d^1$ of Si; b) nonlocal pseudopotential of Si for angular momentum $l = 0, 1, 2$, and the Couloumb potential of a point-like atomic core (dashed line) (from [62]) .

Pseudopotentials of silicon for angular momenta $l = 0, 1, 2$ are presented in Fig. 2.2b. For the thorough overview of different approaches in pseudopotential method we refer to [25] and references cited therein.

The calculations can be performed after the construction of desired pseudopotentials for all the different atoms in the system. The resulting valence wavefunctions are smooth enough to be well represented with a plane wave basis set. As the number of basis functions must be finite in practical calculations, the plane wave expansion of wavefunctions is truncated after some energy. The plane wave basis set is very inefficient in the description of strong oscillations of all-electron wavefunctions near the nucleus. Although computationally cheap, the pseudopotential method comes with a price – all the information on the electron density and wavefunctions in the core region is lost. This deficiency is overcame by the method described in the following section.

2.3 Projector augmented wave method

Two distinct methodologies, i.e. all-electron methods and pseudopotentials, can be combined into a unified electronic structure method – *the projector augmented wave method* (PAW) [63]. As most of the calculations in this thesis were done with GPAW

code based on the PAW method, we will dedicate the remainder of the chapter to this particular approach.

At the root of the PAW method lies a transformation that maps the *true wavefunctions* with their complete nodal structure onto *auxiliary wavefunctions* that are numerically convenient.[7] The goal is to have smooth auxiliary wavefunctions with a rapidly convergent plane wave expansion that will allow calculations similar to that of the pseudopotential approach. In the PAW method, auxiliary wavefunctions are used to construct the true wavefunctions from which one evaluates the total energy and other relevant physical quantities. To some extent, the PAW method is a missing link between APW methods and the pseudopotential method, and the latter can be derived from the PAW method with a suitable approximations [64].

2.3.1 PAW transformation operator

We begin this discussion by stressing out that within the PAW method the core and the valence wavefunctions have distinct treatment. To elaborate on the underlined differences, let us denote the true valence wavefunctions as $|\psi_i\rangle$ and the auxiliary wavefunctions with $|\tilde{\psi}_i\rangle$, where $i \equiv (i, \mathbf{k}, \sigma)$ is the composite label that contains the band index i, a k-point vector $\mathbf{k}$ and a spin index σ. The transformation $\mathcal{T}$ that maps auxiliary wavefunctions to the true valence wavefunctions is defined as

$$|\psi_i\rangle = \mathcal{T}\,|\tilde{\psi}_i\rangle\,, \tag{2.26}$$

and consequently the KS equations (1.33) are transformed as follows

$$\mathcal{T}^\dagger H \mathcal{T}\,|\tilde{\psi}_i\rangle = \mathcal{T}^\dagger \mathcal{T}\,|\tilde{\psi}_i\rangle\,\varepsilon_i. \tag{2.27}$$

The equation (2.27) is the same as (1.33) a Schrödinger-like equation, but for a transformed hamiltonian $\mathcal{T}^\dagger H \mathcal{T}$ and with an overlap operator $\mathcal{T}^\dagger \mathcal{T}$ on the right-hand side. The operator $\mathcal{T}$ has to modify the smooth auxiliary wavefunction in atomic regions, as we demand the true wavefunction to have a correct nodal structure. Therefore, it makes sense to write a transformation operator as identity plus the sum of atomic contributions,

$$\mathcal{T} = \mathbb{1} + \sum_R \mathcal{S}_R. \tag{2.28}$$

For every atom R in the system, the local term $\mathcal{S}_R$ adds the difference in the atomic region around that particular atom between the true and the auxiliary wavefunction.

[7] One should be careful about terminology here, as it has changed from the original work of Blöchl. By true wavefunction, we mean the true solution to the original KS equations (1.33) with no transformation of any kind involved. Thus, this would be an analogue to the all-electron wavefunction in the pseudopotential approach. Also, the name auxiliary wavefunction is used to make a distinction from the pseudo wavefunctions defined in the pseudopotential approach.

It is defined in terms of the so-called *partial waves*, which are the solutions $|\phi_{l_R}\rangle$ of the Schrödinger equation for the isolated atom R.

Partial waves $|\phi_{l_R}\rangle$ for the basis set inside the atomic sphere of the atom R, thus any valence wavefunction inside the atomic region R can be expressed as a linear combination of partial waves with yet unknown coefficients,

$$\psi(\mathbf{r}) = \sum_{l_R} \phi_{l_R}(\mathbf{r}) c_{l_R}, \quad \text{in the region } |\mathbf{r} - \mathbf{R}_R| < r_{c,R}. \tag{2.29}$$

The label $l_R \equiv ((lm), \alpha)_R$ refers to a site R and contains the angular momentum indices (lm) and an additional index α that differentiates the partial waves with the same angular momentum quantum numbers on the site R. It should be noted that the partial waves are not the bound states and consequently are not normalizable, unless we truncate them beyond a certain radius $r_{c,R}$. The results obtained with the PAW method do not depend on the sphere radius $r_{c,R}$ as long as the truncation is not done too close to the nucleus.

The core wavefunctions are treated separately, as they do not spread out of the corresponding atomic spheres. Thus the truncation radii $r_{c,R}$ for all the atoms must be chosen in a way that all the core states lie completely inside the atomic spheres. Furthermore, we will use *the frozen-core approximation* so that electron density and energy that correspond to the core states are the same as they are in the isolated atoms. We require that the transformation $\mathcal{T}$ produce only the wavefunctions that are orthogonal to the core states. Therefore, the set of atomic partial waves $|\phi_{i_R}\rangle$ includes only the valence wavefunctions that are orthogonal to the core wavefunctions of the atom R.

For each partial wave an auxiliary partial wave $|\tilde{\phi}_{l_R}\rangle$ is used in the definition of the local operator $\mathcal{S}_R$,

$$|\phi_{l_R}\rangle = (\mathbb{1} + \mathcal{S}_R)\,|\tilde{\phi}_{l_R}\rangle \quad \Leftrightarrow \quad \mathcal{S}_R\,|\tilde{\phi}_{l_R}\rangle = |\phi_{l_R}\rangle - |\tilde{\phi}_{l_R}\rangle\,. \tag{2.30}$$

Since the operator $\mathbb{1} + \mathcal{S}_R$ changes the wavefunctions only inside the region of atom R, we require that the partial waves are identical to their auxiliary counterpart beyond a certain radius $r_{c,R}$, i.e.

$$\phi_{l_R}(\mathbf{r}) = \tilde{\phi}_{l_R}(\mathbf{r}) \quad \text{for} \quad |\mathbf{r} - \mathbf{R}_R| > r_{c,R}. \tag{2.31}$$

As the transformation operator $\mathcal{T}$ must be applicable to an arbitrary auxiliary wavefunction and $\mathcal{T}$ is just a sum of the local transformations $\mathcal{S}_R$, the local expantion of the auxiliary wavefunction into the auxiliary partial waves can be written as

$$\tilde{\psi}(\mathbf{r}) = \sum_{l_R} \tilde{\phi}_{l_R}(\mathbf{r})\,\langle \tilde{p}_{l_R} | \tilde{\psi} \rangle \quad \text{for} \quad |\mathbf{r} - \mathbf{R}_R| < r_{c,R}. \tag{2.32}$$

The last equation is a definition of *the projector functions* $|\tilde{p}_{l_R}\rangle$ for the atom R. Furthermore, the equation (2.32) draws the conclusion that $\sum_{l_R} |\tilde{\phi}_{l_R}\rangle \langle\tilde{p}_{l_R}| = \mathbb{1}$, which is valid inside the atomic region R. This also implies that $\langle\tilde{p}_{l_R}|\tilde{\phi}_{m_R}\rangle = \delta_{l_R,m_R}$. Note that neither the projector functions nor the partial waves need to be orthogonal among themselves.

The action of $\mathcal{S}_R$ on an arbitrary auxiliary wavefunction can be expressed from equations (2.30) and (2.32) as

$$\mathcal{S}_R |\tilde{\psi}\rangle = \sum_{l_R} \mathcal{S}_R |\tilde{\phi}_{l_R}\rangle \langle\tilde{p}_{l_R}|\tilde{\psi}\rangle = \sum_{l_R} \big(|\phi_{l_R}\rangle - |\tilde{\phi}_{l_R}\rangle \big) \langle\tilde{p}_{l_R}|\tilde{\psi}\rangle \,. \tag{2.33}$$

The transformation operator is constructed as a sum of the contributions from all the atoms in the system, i.e.

$$\mathcal{T} = \mathbb{1} + \sum_R \sum_{l_R} (|\phi_{l_R}\rangle - |\tilde{\phi}_{l_R}\rangle) \langle\tilde{p}_{l_R}| \,. \tag{2.34}$$

The true valence wavefunction can be expressed as

$$|\psi\rangle = |\tilde{\psi}\rangle + \sum_R \sum_{l_R} (|\phi_{l_R}\rangle - |\tilde{\phi}_{l_R}\rangle) \langle\tilde{p}_{l_R}|\tilde{\psi}\rangle = |\tilde{\psi}\rangle + \sum_R \big(|\psi^1_R\rangle - |\tilde{\psi}^1_R\rangle \big), \tag{2.35}$$

where we defined the one-center expansions

$$\begin{aligned} |\psi^1_R\rangle &= \sum_{l_R} |\phi_{l_R}\rangle \langle\tilde{p}_{l_R}|\tilde{\psi}\rangle \,, \\ |\tilde{\psi}^1_R\rangle &= \sum_{l_R} |\tilde{\phi}_{l_R}\rangle \langle\tilde{p}_{l_R}|\tilde{\psi}\rangle \,. \end{aligned} \tag{2.36}$$

Let us elaborate on the expression (2.35) of the true valence wavefunction in the different regions of space:

- according to (2.31) in the *interstitial region* the partial waves are pairwise identical to their auxiliary counterparts so that the auxiliary wavefunction in this region is identical to the true valence wavefunction, $\psi(\mathbf{r}) = \tilde{\psi}(\mathbf{r})$.
- in the *augmentation region* (in any atomic region in the system) the true valence wavefunction is equal to its partial wave expansion in that particular region, i.e. $\psi(\mathbf{r}) = \psi^1_R(\mathbf{r})$ as the auxiliary wave function and its partial wave expansion are equal according to (2.32).

In practice the partial wave expansions are truncated. Thus, the identity (2.32) does not hold strictly and the consequence is that the plane waves (i.e. the basis for the expansion of the auxiliary wavefunction) also contribute to the true wavefunction in

the atomic region. In this way the missing terms in the partial wave expansion are recovered by plane waves.

The final note of this subsection is an answer to the question whether the transformation of the auxiliary wavefunction defined in (2.34) indeed provides the true wavefunction. The transformation should be thought of merely as a change of representation analogous to a change of coordinates [65]. Therefore, if the total energy functional is transformed consistently, its minimum will yield an auxiliary wavefunction that produces the correct true wavefunction.

2.3.2 Expectation values of operators

As we have defined the transformation itself in Subsection 2.3.1, the question arise how to calculate relevant physical quantities, i.e. the expectation values of corresponding operators. The expectation values can be determined either from the reconstructed true wavefunctions or directly from the auxiliary wavefunctions with the use of the transformed operator,

$$\begin{aligned} \langle A \rangle &= \sum_i f_i \langle \psi_i | A | \psi_i \rangle + \sum_{j=1}^{N_c} \langle \phi_j^c | A | \phi_j^c \rangle \\ &= \sum_i f_i \langle \tilde{\psi}_i | \mathcal{T}^\dagger A \mathcal{T} | \tilde{\psi}_i \rangle + \sum_{j=1}^{N_c} \langle \phi_j^c | A | \phi_j^c \rangle \,, \end{aligned} \tag{2.37}$$

where f_i are the occupation numbers of the valence states and N_c is the total number of core states in the system (thus this sum runs over all the atoms in the system). According to (2.35) we can decompose the matrix elements into their individual contributions as

$$\begin{aligned} \langle \psi | A | \psi \rangle &= \langle \tilde{\psi} + \sum_R \big(\psi_R^1 - \tilde{\psi}_R^1 \big) | A | \tilde{\psi} + \sum_{R'} \big(\psi_{R'}^1 - \tilde{\psi}_{R'}^1 \big) \rangle \\ &= \underbrace{\langle \tilde{\psi} | A | \tilde{\psi} \rangle + \sum_R \big(\langle \psi_R^1 | A | \psi_R^1 \rangle - \langle \tilde{\psi}_R^1 | A | \tilde{\psi}_R^1 \rangle \big)}_{\text{part 1}} \\ &+ \underbrace{\sum_R \big(\langle \psi_R^1 - \tilde{\psi}_R^1 | A | \tilde{\psi} - \tilde{\psi}_R^1 \rangle + h.c. \big)}_{\text{part 2}} \\ &+ \underbrace{\sum_{R \neq R'} \langle \psi_R^1 - \tilde{\psi}_R^1 | A | \psi_{R'}^1 - \tilde{\psi}_{R'}^1 \rangle}_{\text{part 3}} . \end{aligned} \tag{2.38}$$

Only the first part of (2.38) is evaluated explicitly while the second and the third part are neglected, because they vanish for sufficiently local operators as long as the

partial wave expansion is well converged. For the second part the argumentation for such approximation is as follows: the difference $\psi_R^1 - \tilde{\psi}_R^1$ vanishes per construction beyond some augmentation region, as the partial waves are pairwise identical beyond that region; the difference $\tilde{\psi} - \tilde{\psi}_R^1$ vanishes inside the augmentation region if the partial wave expansion is sufficiently converged; thus, in no region of space both functions $\psi_R^1 - \tilde{\psi}_R^1$ and $\tilde{\psi} - \tilde{\psi}_R^1$ are simultaneously nonzero. For the third part the conclusion is similar, as the differences $\psi_R^1 - \tilde{\psi}_R^1$ from different sites can not be nonzero in the same region of space. Therefore, the second and the third part of (2.38) can easily be neglected for operators such as the kinetic energy or the real space projection operator $|\mathbf{r}\rangle \langle \mathbf{r}|$ which produces the electron density. It should be noted that for truly nonlocal operators (such as the Hartree term) the second and the third part must be treated differently. For the expressions of the expectation values of nonlocal operators, calculation of forces, construction of partial waves and projector functions, local properties (projected density of states, local magnetic moments etc.) as well as the treatment of the external potentials in PAW and many other technical details required to make the method work in practice we refer to [66].[8]

Thus, neglecting the second and the third part of (2.38), using (2.35) and the first line of (2.37), we can express the expectation values of the local and semilocal operators as

$$\begin{aligned}
\langle A \rangle &= \sum_i f_i \big(\langle \tilde{\psi}_i | A | \tilde{\psi}_i \rangle + \langle \psi_i^1 | A | \psi_i^1 \rangle - \langle \tilde{\psi}_i^1 | A | \tilde{\psi}_i^1 \rangle \big) + \sum_{j=1}^{N_c} \langle \phi_j^c | A | \phi_j^c \rangle \\
&= \sum_i f_i \, \langle \tilde{\psi}_i | A | \tilde{\psi}_i \rangle + \sum_{j=1}^{N_c} \langle \tilde{\phi}_j^c | A | \tilde{\phi}_j^c \rangle \\
&+ \sum_R \Big(\sum_{l,l' \in R} D_{ll'} \, \langle \phi_l | A | \phi_{l'} \rangle + \sum_{j \in R}^{N_{c,R}} \langle \phi_j^c | A | \phi_j^c \rangle \Big) \\
&- \sum_R \Big(\sum_{l,l' \in R} D_{ll'} \, \langle \tilde{\phi}_l | A | \tilde{\phi}_{l'} \rangle + \sum_{j \in R}^{N_{c,R}} \langle \tilde{\phi}_j^c | A | \tilde{\phi}_j^c \rangle \Big),
\end{aligned} \tag{2.39}$$

where we used the notation $l, l' \in R$ to point out that the indices l and l' refer to the partial waves of the same site R (the notation l_R,l'_R would be cumbersome) and $N_{c,R}$ is the number of core states of the atom R. We have also introduced *the one-center*

[8] The paper of Rostgaard is a self-contained description of the basic theory of PAW method. The expressions and notation therein closely follow the implementation of PAW method in the GPAW code.

density matrix $D_{ll'}$, which is defined as

$$D_{ll'} = \sum_i f_i \langle \tilde{\psi}_i | \tilde{p}_l \rangle \langle \tilde{p}_{l'} | \tilde{\psi}_i \rangle = \sum_i \langle \tilde{p}_{l'} | \tilde{\psi}_i \rangle f_i \langle \tilde{\psi}_i | \tilde{p}_l \rangle . \tag{2.40}$$

The auxiliary core states $|\tilde{\phi}_j^c\rangle$ allow to incorporate the tails of the core wavefunctions into the plane wave part and thus assure that the partial wave contributions cancel strictly beyond the augmentation region. The auxiliary core states are identical to the true core states in the tales, but are a smooth continuation inside the atomic sphere.

The electron density is given by

$$\begin{aligned} n(\mathbf{r}) &= \tilde{n}(\mathbf{r}) + \sum_R \big(n_R^1(\mathbf{r}) - \tilde{n}_R^1(\mathbf{r}) \big), \\ \tilde{n}(\mathbf{r}) &= \sum_i f_i \tilde{\psi}_i^*(\mathbf{r}) \tilde{\psi}_i(\mathbf{r}) + \tilde{n}_c, \\ n_R^1(\mathbf{r}) &= \sum_{l,l' \in R} D_{ll'} \phi_{l'}^*(\mathbf{r}) \phi_l(\mathbf{r}) + n_{c,R}, \\ \tilde{n}_R^1(\mathbf{r}) &= \sum_{l,l' \in R} D_{ll'} \tilde{\phi}_{l'}^*(\mathbf{r}) \tilde{\phi}_l(\mathbf{r}) + \tilde{n}_{c,R}, \end{aligned} \tag{2.41}$$

where $n_{c,R}$ is the core density of the atom R and $\tilde{n}_{c,R}$ its auxiliary counterpart identical to the true core density in the interstitial region and a smooth continuation inside the augmentation region.

The bare electrostatic potential of nucleus is difficult to represent using delocalized basis sets, as its eigenvalues are slowly converging with the plane wave expansion. In a cases like this one can heal the undesirable behavior in the equations for the smooth functions by adding and subtracting a properly chosen operator B_R, localized in a single atomic region R. As a consequence of a strict localization of operator B_R, one can use the identity between the auxiliary wave function and its own partial wave expansion and express the expectation values of B_R as follows

$$0 = \langle \tilde{\psi}_i | B_R | \tilde{\psi}_i \rangle - \langle \tilde{\psi}_i^1 | B_R | \tilde{\psi}_i^1 \rangle . \tag{2.42}$$

By repeating this procedure for each atomic region the nuclear Coulomb singularity in the equations for the smooth functions can be completely removed, and what is left is the term that can be dealt with in the radial equations about each nucleus.

2.3.3 Total energy

The main goal of PAW method is to provide the numerical background for practical calculations within DFT, where the total energy is one of the most important

quantities. Similar to wavefunctions, the total energy of the system can be written as a sum of three terms

$$E = \tilde{E} + \sum_R (E^1_R - \tilde{E}^1_R), \tag{2.43}$$

and we shall explain in detail every term separately.

The plane wave part $\tilde{E}$ involves only smooth functions and is evaluated on equispaced grids in real and reciprocal space. This is computationally the most demanding part, and the calculation is similar to the pseudopotential approach. Recalling the Kohn-Sham expression (1.26) for total energy, the smooth part of the total energy can be written as follows

$$\begin{aligned}\tilde{E} = &\sum_i \langle\tilde{\psi}_i| - \frac{1}{2}\nabla^2|\tilde{\psi}_i\rangle + \frac{1}{2}\int \mathrm{d}^3\mathbf{r}\int \mathrm{d}^3\mathbf{r}'\frac{\big(\tilde{n}(\mathbf{r}) + \tilde{Z}(\mathbf{r})\big)\big(\tilde{n}(\mathbf{r}') + \tilde{Z}(\mathbf{r}')\big)}{|\mathbf{r}-\mathbf{r}'|} \\ &+ \int \mathrm{d}^3\mathbf{r}\,\tilde{n}(\mathbf{r})\epsilon_{\mathrm{xc}}(\mathbf{r};[\tilde{n}]) + \int \mathrm{d}^3\mathbf{r}\,\bar{v}(\mathbf{r})\tilde{n}(\mathbf{r}).\end{aligned} \tag{2.44}$$

The term $\tilde{Z}(\mathbf{r})$ is an angular dependent core-like density that will be described after we give the expressions for the second and third part of total energy. The second part of total energy is the sum of terms

$$\begin{aligned}E^1_R = &\sum_{l,l'\in R} D_{ll'}\,\langle\phi_{l'}| - \frac{1}{2}\nabla^2|\phi_l\rangle + \sum_{j\in R}^{N_{c,R}} \langle\phi^c_j| - \frac{1}{2}\nabla^2|\phi^c_j\rangle \\ &+ \frac{1}{2}\int \mathrm{d}^3\mathbf{r}\int \mathrm{d}^3\mathbf{r}'\frac{\big(\tilde{n}^1(\mathbf{r}) + Z(\mathbf{r})\big)\big(\tilde{n}^1(\mathbf{r}') + Z(\mathbf{r}')\big)}{|\mathbf{r}-\mathbf{r}'|} \\ &+ \int \mathrm{d}^3\mathbf{r}\,n^1(\mathbf{r})\epsilon_{\mathrm{xc}}(\mathbf{r};[n^1]),\end{aligned} \tag{2.45}$$

and the third part is similarly

$$\begin{aligned}\tilde{E}^1_R = &\sum_{l,l'\in R} \langle\tilde{\phi}_{l'}|\frac{1}{2}\nabla^2|\tilde{\phi}_l\rangle \\ &+ \frac{1}{2}\int \mathrm{d}^3\mathbf{r}\int \mathrm{d}^3\mathbf{r}'\frac{\big(\tilde{n}^1(\mathbf{r}) + \tilde{Z}(\mathbf{r})\big)\big(\tilde{n}^1(\mathbf{r}') + \tilde{Z}(\mathbf{r}')\big)}{|\mathbf{r}-\mathbf{r}'|} \\ &+ \int \mathrm{d}^3\mathbf{r}\,\tilde{n}^1(\mathbf{r})\epsilon_{\mathrm{xc}}(\mathbf{r};[\tilde{n}^1]) + \int \mathrm{d}^3\mathbf{r}\,\bar{v}(\mathbf{r})\tilde{n}^1(\mathbf{r}).\end{aligned} \tag{2.46}$$

The nuclear charge density $-Z(\mathbf{r})$ is defined as a sum of δ-functions on the nuclear sites, $Z(\mathbf{r}) = -\sum_R \mathcal{Z}_R\delta(\mathbf{r}-\mathbf{R})$, where $\mathcal{Z}_R$ are the atomic numbers. Note that the self energy of a point charge is infinite and thus it must be subtracted out.

Two terms in the expressions for total energy deserve closer inspection – the *compensation density* $\tilde{Z}(\mathbf{r}) = \sum_R \tilde{Z}_R(\mathbf{r})$ and the potential $\bar{v}(\mathbf{r})$. The former is given as a sum of angular momentum dependent gaussians, which have an analytical Fourier

transform. It is nonspherical and it is constantly adapting to the instantaneous environment.[9] The construction of compensation charges must be achieved in a way that the augmentation charge densities $n_R^1(\mathbf{r}) + Z_R(\mathbf{r}) - \tilde{n}_R^1(\mathbf{r}) - \tilde{Z}_R(\mathbf{r})$ have vanishing electrostatic multi-pole moments for each atomic site. This is necessary if we don't want for the one-center contributions to produce an electrostatic potential outside of their own atomic region. When this condition is fulfilled, the electrostatic interaction of the one-center parts between different sites vanishes. Moreover, the compensation density given in this form is still localized in the atomic region, but a technique similar to Ewald summation [67] allows to replace it by a very extended charge density. If this is done, all the functions in $\tilde{E}$ converge as fast as the auxiliary density itself.

The potential $\bar{v} = \sum_R \bar{v}_R$, which occurs in the last terms of (2.44) and (2.46) enters the total energy in the form of the operator B, described in Subsection 2.3.2

$$\begin{aligned} 0 &= \sum_R \left[\sum_i f_i \, \langle \tilde{\psi}_i | \Big(\bar{v}_R - \sum_{l,l' \in R} |\tilde{p}_l\rangle \, \langle \tilde{\phi}_l | \bar{v}_R | \tilde{\phi}_{l'} \rangle \, \langle \tilde{p}_{l'}| \Big) | \tilde{\psi}_i \rangle \right] \\ &= \sum_R \left[\sum_i f_i \, \langle \tilde{\psi}_i | \bar{v}_R | \tilde{\psi}_i \rangle - \sum_R \sum_{l,l' \in R} D_{ll'} \, \langle \tilde{\phi}_l | \bar{v}_R | \tilde{\phi}_{l'} \rangle \right]. \end{aligned} \tag{2.47}$$

The main reason behind the introduction of potential $\bar{v}$ is that the self-consistent potential in the plane-wave part of total energy $\tilde{E}$ is rarely smooth enough. This artificial potential improves the plane wave convergence significantly, without changing the converged result. Note that $\bar{v}$ must be localized within the augmentation region, where the expansion (2.32) of the auxiliary wavefunction into the auxiliary partial waves holds.

2.3.4 Comparison of PAW and pseudopotential methods

Once we have obtained the expression for the total energy in terms of the electron density, the rest follows: the Kohn-Sham potential is the derivative of the potential energy with respect to density, the hamiltonian follows from derivatives with respect to wavefunctions and the forces are partial derivatives of the energy functional with respect to atomic positions. As we stated in Section 2.2 the PAW method is to some extent an approach that combines the pseudopotentials with the all-electron methods, thus recovering the information about electron density in the regions close to nuclei. The question arise: what approximations are incorporated into the PAW method? The answer is that all the approximations are made already in the derivation of the expression for the total energy functional:

[9] A similar term occurs in the pseudopotential approach. For comparison of the compensation charge densities in PAW and pseudopotential method we refer to [64].

- we use the frozen-core approximation. It is not an inherent characteristic of the PAW method and in principle can be overcome. See [68] for a relaxation of this requirement;

- the plane wave expansion of the auxiliary wavefunction is truncated after some energy cutoff defined as $E_{\mathrm{cut}} = \frac{1}{2}(\hbar^2)G^2_{\mathrm{max}}$. The size of the basis set can be easily controlled with this single parameter, thus achieving the desired convergence degree. Typical cutoff is around 15 Ha ($\approx$ 400 eV);

- the partial wave expansions must be converged. Most often one uses one or two partial waves per angular momentum (l, m) and site. Cautionary note is that the partial wave expansion is *not* variational, as the changes in partial waves affect the total energy functional itself and not only the basis set.

The PAW method is in a close connection with the pseudopotential approach. Moreover, the latter can be derived as the well defined approximation from the PAW method. The augmentation part of total energy $\Delta E = E^1 - \tilde{E}^1$ is a functional of the one-center density matrix $D_{ll'}$ defined in (2.40), and the pseudopotential approach can be recovered if we truncate a Taylor expansion of ΔE about the atomic density matrix after the linear term, and the term linear to $D_{ll'}$ is the energy related to the nonlocal pseudopotential,

$$\begin{aligned} \Delta E(D_{ll'}) &= \Delta E(D^{\mathrm{at}}_{ll'}) + \sum_{l,l'}(D_{ll'} - D^{\mathrm{at}}_{ll'})\frac{\partial \Delta E}{\partial D_{ll'}} + O(D_{ll'} - D^{\mathrm{at}}_{ll'})^2 \\ &= E_{\mathrm{self}} + \sum_i f_i \, \langle \tilde{\psi}_i | v_{\mathrm{nl}} | \tilde{\psi}_i \rangle + O(D_{ll'} - D^{\mathrm{at}}_{ll'})^2. \end{aligned} \tag{2.48}$$

The last expression can be interpreted as follows: the PAW method is an analogue to the pseudopotential method but with a pseudopotential that adapts to the instantaneous electronic environment. This is achieved as the explicit nonlinear dependence of the total energy on the one-center density matrix is properly taken into account. Derivation of the formal relationship between the PAW method and the ultra-soft pseudopotentials [69] in detail can be found in the paper of Kresse and Joubert [64].

To conclude the discussion on the PAW method, we will point out its main advantages compared to the pseudopotentials:

- PAW method cures the transferability issues of the pseudopotential method. Watson [70] and Kresse [64] shown that most pseudopotentials fail for high spin atoms such as Cr. Even if it is possible to construct the pseudopotentials that can handle situations like this, the failure can not be predicted beforehand. There is no guarantee that a pseudopotential constructed from the all-electron

calculation on isolated atom or by fitting to experimental data will be accurate for molecule or solid. In contrast, well-converged PAW results do not depend on a reference system such as isolated atom, because it uses the full density and potential.

- The full charge and spin density obtained with PAW method enable the determination of hyperfine parameters. These parameters are sensitive probes of the electron density near the nucleus, which is not available in the pseudopotential method. Though the reconstruction techniques for the pseudopotential approach that make possible the calculation of hyperfine parameters are invented [71], they are not widely used as the PAW method is more straightforward and more precise.

- the plane wave convergence is more rapid compared to the norm-conserving pseudopotentials and should be equivalent to that of ultra-soft pseudopotentials [69]. However, the expression for total energy in PAW method is simpler than that of the ultra-soft pseudopotentials and therefore is expected to be more efficient.

- the algorithm for the construction of pseudopotentials requires the determination of parameters $\{\lambda_i\}$. As they influence the results, their choice can be critical. Furthermore, the PAW method provides more flexibility for the choice of auxiliary partial waves, which are like pseudopotentials obtained from the isolated atom as reference system. However, the choice of partial waves does not influence the converged results.

Chapter 3

Two-dimensional materials

Discovery of graphene in 2004 [1], the first truly two-dimensional (2D) crystal, has started a new era of materials' science and triggered the exponential growth of interest in 2D materials across various disciplines. Since their modern debut, owing to the rich variety of structural, mechanical, thermal, electronic and optical properties, 2D materials continue to exhibit scientific and technological promise. They provide a broad platform for theoretical and experimental investigation and development of next-generation nano- and optoelectronic devices. The ongoing efforts resulted with nearly a hundred of experimentally isolated 2D materials and thousands of them that are just waiting to be discovered [72].

A spotlight of the last decade of research has been on 2D semiconductors [73] whose physical properties can be tuned through manipulation of thickness [74], substrate engineering, strain [75, 76], or doping [77]. The possibilities are becoming even greater with the synthesis of van der Waals heterostructures [2], made by stacking layers of different 2D materials in a precisely chosen sequence. In this chapter, bearing in mind the still growing manifold of 2D materials and their heterostructures, we will provide the very basics of the structural and electronic properties of the few representatives which are in the focus of our current research.

3.1 Graphene

Graphene is a single-atomic layer of carbon atoms arranged in a hexagonal structure (Fig. 3.1). It is the basic atomic structure for all the other carbon allotropes. The ball structure of zero-dimensional (0D) *fullerene* (C_{60}) can be wrapped-up from a piece of graphene layer with the introduction of pentagons (and therefore curvature) of carbon atoms. Similarly, one-dimensional (1D) *carbon nanotubes* (CNTs) with a variety of chiralities can be made by rolling graphene sheets into cylinders with the diameter of few nanometers. The direction of rolling, given by the chiral vector in

a graphene plane, defines the chirality of CNTs.

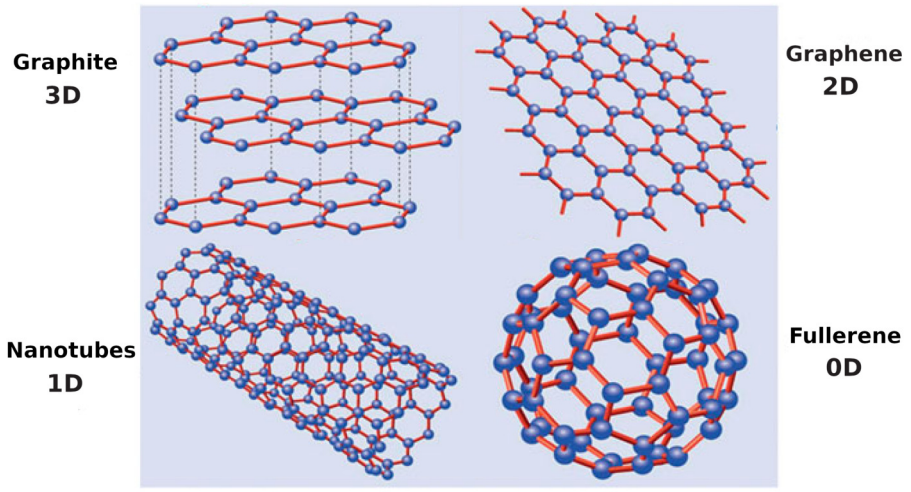

Figure 3.1: Carbon allotropes of different dimensions. Adapted from [78].

The first high-quality graphene sheets were isolated from *graphite* by Geim and Novoselov in 2004 using the technique called the micromechanical cleavage [1]. The subtle optical effect that graphene creates on top of SiO_2 substrate of carefully chosen thickness allows its observation with an ordinary optical microscope. Prior to this discovery, the first observation of graphene was reported in 1961 by Boehm and coworkers [79]. They obtained single graphite sheets[1] by reduction of graphite oxide in very dilute alkaline suspensions, but the mechanical exfoliation of graphene directly from graphite along with the demonstration of its extraordinary properties such as strong ambipolar electric field effect with a carrier concentration of $10^{13}\,\mathrm{cm}^{-2}$ and a room-temperature mobility of $10^4\,\mathrm{cm}^2\,\mathrm{V}^{-1}\,\mathrm{s}^{-1}$ was due to Geim and Novoselov. The significance of their work was recognized by the science community and the two researchers shared the Nobel Prize in Physics in 2010.

The discovery of graphene came four centuries after the invention of a lead pencil with a core made of graphite powder mixed with a clay binder. A lead pencil is suitable for writing and drawing as the graphite is made out of graphene monolayers weakly coupled by van der Waals forces (Fig. 3.1). Thus, every time we press a pencil against a paper we are producing graphene sheets. The reason for a few-centuries gap between the invention of pencil and the isolation of graphene is twofold: (a) only recently the suitable experimental tools for the search of one-atom-thick materials are constructed and (b) no one expected for the 2D material to exist in a free state, as Mermin argued that the long-range crystalline order in two dimensions can be

[1]The word *graphene* was coined by Hanns-Peter Boehm in 1986 to describe single sheets of graphite, but the term itself became highly popular only after the discovery of Geim and Novoselov.

broken with little energy cost at any finite temperature thus breaking 2D crystal at ambient conditions [80].

3.1.1 Graphene crystal structure

Graphene crystal structure consists of two interpenetrating triangular sublattices, A and B. Therefore, the honeycomb lattice can be represented as a triangular lattice with a two-atoms basis and a lattice constant of $a = 2.46$ Å. Every atom of sublattice A has three nearest neighbors from sublattice B (and vice versa) at the distance of $a/\sqrt{3} \approx 1.42$ Å (Fig. 3.2). The primitive lattice vectors $\mathbf{a}_1$ and $\mathbf{a}_2$ (Fig. 3.2) can be written as

$$\mathbf{a}_1 = \left(\frac{a}{2}, \frac{\sqrt{3}a}{2}\right), \quad \mathbf{a}_2 = \left(\frac{a}{2}, -\frac{\sqrt{3}a}{2}\right). \tag{3.1}$$

From the relations $\mathbf{a}_i \cdot \mathbf{b}_j = 2\pi\delta_{ij}$ we find the primitive vectors of the reciprocal lattice,

$$\mathbf{b}_1 = \left(\frac{2\pi}{a}, \frac{2\pi}{\sqrt{3}a}\right), \quad \mathbf{b}_2 = \left(\frac{2\pi}{a}, -\frac{2\pi}{\sqrt{3}a}\right). \tag{3.2}$$

On Fig. 3.2b the high symmetry BZ points are labeled. Of particular importance

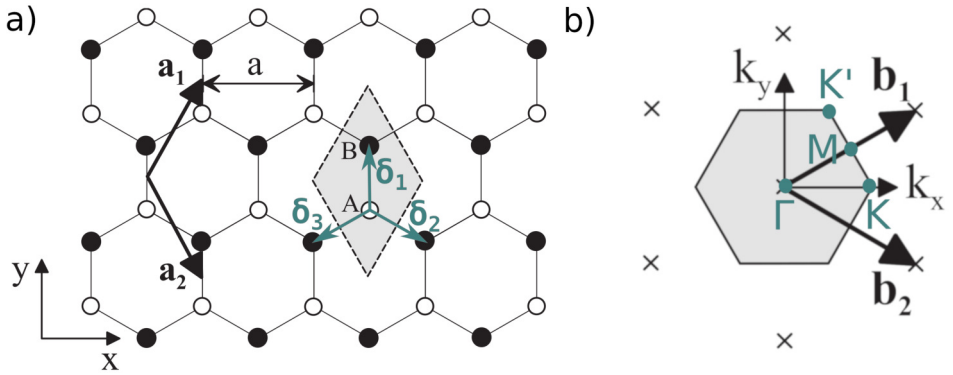

Figure 3.2: a) Honeycomb lattice is made of two interpenetrating triangular lattices labeled with A (white circles) and B (black circles). $\mathbf{a}_1$ and $\mathbf{a}_2$ are lattice primitive vectors and $\boldsymbol{\delta}_1$, $\boldsymbol{\delta}_2$, $\boldsymbol{\delta}_3$ (green) are the nearest neighbors vectors. b) BZ of the triangular lattice (shaded area) with the high symmetry points (green) Γ, K, K′, M. $\mathbf{b}_1$ and $\mathbf{b}_2$ are primitive vectors of the reciprocal lattice. Adapted from [81].

are the six corners of the BZ – points K and K′ – for reasons that will become clear latter.[2] The triangle ΓMK is the irreducible wedge of the BZ.

[2]Only two adjacent BZ corners are inequivalent, as the other four can be reached from these two with the translations by reciprocal lattice vectors.

3.1.2 sp^2 hybridization

Carbon is the sixth element in the periodic system. The electronic configuration of an isolated carbon atom is $1s^2 2s^2 2p^2$, i.e. two electrons are in the core $1s$ state and they are not involved in the chemical bonds while the rest four electrons are in the valence $2s$ and $2p$ states. As the energies of $2p$ orbitals $(2p_x, 2p_y, 2p_z)$ are approximately 4 eV higher than the energy of $2s$ orbital, it is favorable that two electrons occupy $2s$ state and the other two occupy $2p$ states. However, in molecules and solids, carbon atom is surrounded by its neighbors and the electronic structure is changed drastically from the isolated case. One electron in a carbon atom is excited from $2s$ to the third (empty) $2p$ state. This gives the possibility for carbon atoms

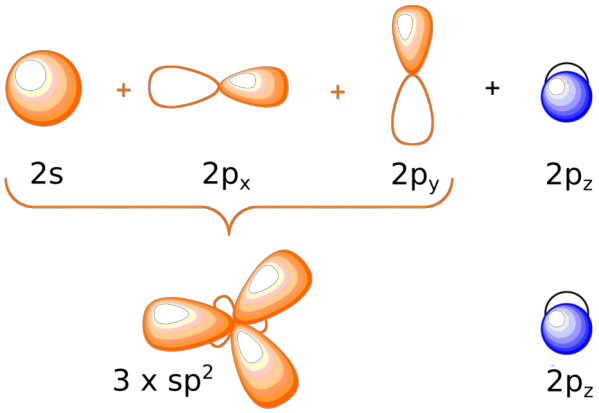

Figure 3.3: Up: valence atomic orbitals of carbon atom; down: hybridized sp^2 orbitals (left) and unaffected $2p_z$ atomic orbital (right).

to form $n+1$ sp^n hybridized orbitals by superposition of $2s$ and $n \times 2p$ orbitals. In graphene, sp^2 hybridization (Fig. 3.3) leads to a trigonal planar structure followed by the formation of strong σ bonds of carbon atom with its three nearest neighbors (Fig. 3.2). Hybridized sp^2 orbitals, lying in graphene (xy) plane, can be written as a linear combination of $2s$, $2p_x$ and $2p_y$ orbitals,

$$
\begin{aligned}
|sp_a^2\rangle &= \frac{1}{\sqrt{3}}|2s\rangle - \sqrt{\frac{2}{3}}|2p_y\rangle\,, \\
|sp_b^2\rangle &= \frac{1}{\sqrt{3}}|2s\rangle + \sqrt{\frac{2}{3}}\left(\frac{\sqrt{3}}{2}|2p_x\rangle + \frac{1}{2}|2p_y\rangle\right), \\
|sp_c^2\rangle &= -\frac{1}{\sqrt{3}}|2s\rangle + \sqrt{\frac{2}{3}}\left(-\frac{\sqrt{3}}{2}|2p_x\rangle + \frac{1}{2}|2p_y\rangle\right).
\end{aligned}
\tag{3.3}
$$

Head-on overlapping of sp^2 orbitals leads to the formation of strong covalent σ bonds in graphene, which are responsible for the robustness of its structure and high mechanical stability. Graphene is the strongest material ever measured, with

an intrinsic tensile strength of 130.5 GPa and a Young's modulus of 1 TPa [82]. The electronic structure emerging from sp^2 orbitals, σ bands, are far from the Fermi level (E_F), thus the electrons which occupy σ bands do not participate in the electronic transport.

In addition to σ bonds in graphene, lateral overlap of the unhybridized $2p_z$ orbitals is leading to the formation of weaker π bonds and the corresponding π *bands*. Details about the π bands, which are crucial for many of peculiar electronic properties of graphene are described in the following subsections.

3.1.3 π bands of graphene

The electronic properties of graphene are mainly governed by the energy bands near E_F, π bands, which originate in the lateral overlap of the atomic $2p_z$ orbitals. The expressions for π bands can be derived via the *tight-binding* (TB) method. The method itself, followed by the complete derivation of the π bands dispersion, is given in Appendix B.

Graphene elementary cell contains two carbon atoms. Each atom participates with one $2p_z$ orbital, thus two energy bands will be derived via the TB method – a fully occupied π and an empty π^* band. Dispersion relations for *the valence* π band ($-$ sign) and *the conduction* π^* band ($+$ sign) are

$$\varepsilon_{\pm}(\mathbf{k}) = \frac{\epsilon_{2p} \pm \gamma|f(\mathbf{k})|}{1 \mp s|f(\mathbf{k})|}, \tag{3.4}$$

where

$$f(\mathbf{k}) = \mathrm{e}^{\mathrm{i}k_y a/\sqrt{3}} + 2\cos(k_x a/2)\mathrm{e}^{-\mathrm{i}k_y a/2\sqrt{3}}. \tag{3.5}$$

Expression (3.4) for the values of parameters $\gamma = 3.033\,\mathrm{eV}$, $s = 0.129$, $\epsilon_{2p} = 0$ (from [83]) is plotted in Fig. 3.4a. The latter value ($\epsilon_{2p} = 0$) means that the zero of energy scale is set to be equal to the energy of $2p_z$ orbital. Graphene has no bandgap as two bands are meeting at K and K′ points in BZ, thus *the valence band maximum* (VBM) and *the conduction band minimum* (CBM) coincide. Finally, the vicinity of points K and K′ is where the graphene shows its remarkable property – the linear energy dispersion near E_F.

3.1.4 Dirac fermions

To derive the expressions for the electronic excitations close to E_F we need to expand $f(\mathbf{k})$ in the vicinity of points K and K′. By relabeling these points according to the inset of Fig. 3.4a, their coordinates become

$$\mathrm{K} \to \mathrm{K}_+ \left(\frac{4\pi}{3a}, 0\right), \;\; \mathrm{K}' \to \mathrm{K}_- \left(-\frac{4\pi}{3a}, 0\right) \quad \Leftrightarrow \quad \mathbf{K}_\xi = \left(\xi\frac{4\pi}{3a}, 0\right), \; \xi = \pm 1. \tag{3.6}$$

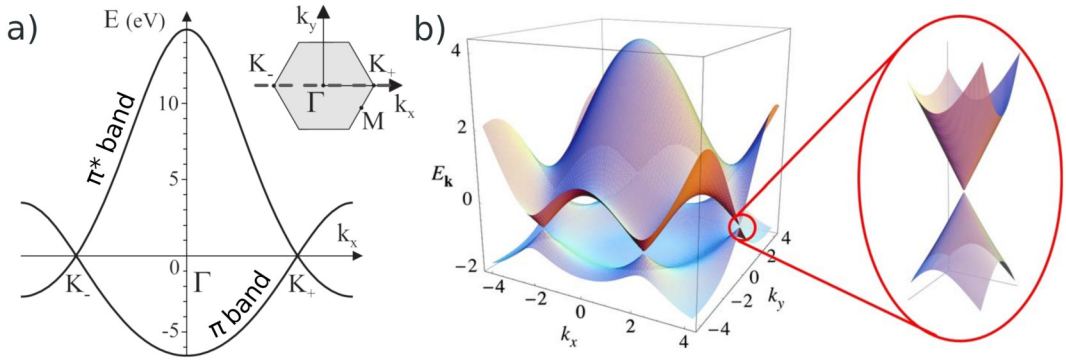

Figure 3.4: a) 2D plot of π bands with BZ in inset. Adapted from [81]. High symmetry points of BZ are relabeled (K$\rightarrow$K$_+$, K$'\rightarrow$K$_-$) to follow the discussion of Dirac fermions. Parameters used in the tight-binding calculations are from [83]; b) 3D plot of π bands of graphene in the approximation of next-nearest neighbors with Dirac cones magnified in the inset. The difference in energy scale compared to the 2D plot comes from the different values of parameters γ and s. From [78].

It is easy to verify that the function $f(\mathbf{k})$ vanishes at the points K$_+$ and K$_-$. If we define $\mathbf{q} \equiv \mathbf{k} - \mathbf{K}_\xi$ and assume that $a|\mathbf{q}| \ll 1$, the Taylor expansion of $f(\mathbf{k})$ near $\mathbf{K}_\xi$ up to the first order yields

$$\begin{aligned} f(\mathbf{k}) = f(\mathbf{K}_\xi + \mathbf{q}) &= \mathrm{e}^{\mathrm{i}q_y a/\sqrt{3}} + 2\mathrm{e}^{-\mathrm{i}q_y a/2\sqrt{3}}\cos\left(\frac{2\pi\xi}{3} + \frac{q_x a}{2}\right) \\ &\approx \left(1 + \frac{\mathrm{i}q_y a}{\sqrt{3}}\right) + 2\left(1 - \frac{\mathrm{i}q_y a}{2\sqrt{3}}\right)\left(-\frac{1}{2} - \frac{\xi\sqrt{3}q_x a}{4}\right) \approx -\frac{a\sqrt{3}}{2}(\xi q_x - \mathrm{i}q_y), \end{aligned} \tag{3.7}$$

For the sake of notational simplicity, let us restrict the discussion to the excitations near the K$_+$ (K) only.[3] Within the first order of q the overlap matrix $\mathcal{S}$ (B.14) can be considered as unity matrix, as $s \sim q^2$. Consequently, the equation (B.7) becomes the eigenproblem for the transfer integral matrix $\mathcal{H}$, indicating that $\mathcal{H}$ is an effective hamiltonian for graphene at low-energy, i.e. it describes the excitations near E_F. As $\mathbf{p} = \hbar\mathbf{q}$, $\mathcal{H}$ can be expressed as follows

$$\mathcal{H}_\mathrm{K} = \frac{a\gamma\sqrt{3}}{2\hbar}\begin{pmatrix} 0 & p_x - \mathrm{i}p_y \\ p_x + \mathrm{i}p_y & 0 \end{pmatrix} = \frac{a\gamma\sqrt{3}}{2\hbar}\mathbf{p}\cdot\boldsymbol{\sigma} = v_F\mathbf{p}\cdot\boldsymbol{\sigma}, \tag{3.8}$$

where $v_F = a\gamma_0\sqrt{3}/(2\hbar)$ is the Fermi velocity and $\boldsymbol{\sigma} = (\sigma_x, \sigma_y)$ are Pauli matrices,

$$\sigma_x = \begin{pmatrix} 0 & 1 \\ 1 & 0 \end{pmatrix}, \quad \sigma_y = \begin{pmatrix} 0 & -\mathrm{i} \\ \mathrm{i} & 0 \end{pmatrix}. \tag{3.9}$$

If we recall the expression for the hamiltonian of the independent relativistic particles of mass m and spin $1/2$ in 2D,

$$\hat{H}_\mathrm{2D} = c\mathbf{p}\cdot\boldsymbol{\sigma} + mc^2\sigma_z, \quad \sigma_z = \begin{pmatrix} 1 & 0 \\ 0 & -1 \end{pmatrix}, \tag{3.10}$$

[3]The discussion for excitations near K$_-$ is analogous, only the chirality is reversed. See [81] p. 14-16.

we conclude that $\mathcal{H}_{\mathrm{K}}$ describes the massless spin-1/2 particles in two dimensions – the so-called *Dirac fermions*.

The eigenvalues and eigenfunctions of hamiltonian (3.8), i.e. energies and wavefunctions of Dirac fermions are

$$\varepsilon_{\pm}(\mathbf{q}) = \pm\hbar v_F q, \quad \Psi_{\pm} = \frac{1}{\sqrt{2}} \begin{pmatrix} 1 \\ \pm \mathrm{e}^{\mathrm{i}\phi} \end{pmatrix} \mathrm{e}^{\mathrm{i}\mathbf{q}\cdot\mathbf{r}}. \tag{3.11}$$

where $\pm$ refers to the conduction and valence bands, respectively, and ϕ is the polar angle of momentum in the graphene plane, $\mathbf{p} = (p_x, p_y) = (p\cos\phi, p\sin\phi)$. Similarly to light, the dispersion of Dirac fermions is linear in momentum but they are approximately 300 times slower than light.

The wavefunction (3.11) has two components, resembling the components of spin-1/2. Referring back to the definitions of the Bloch functions (B.2) and (B.7) shows that this degree of freedom is related to the relative amplitude of the Bloch function on the A and B sublattice. It is called *pseudospin*. If all the electrons of the π band were located on the A sublattice, this could be viewed as a pseudospin "up" state $|\uparrow\rangle = (1,0)^{\mathrm{T}}$, whereas electrons solely on the B sublattice correspond to a "down" state $|\downarrow\rangle = (0,1)^{\mathrm{T}}$. In graphene, electron density is shared equally between sublattices if the A–B symmetry is not broken due to an external potential. For the thorough discussion on the Dirac fermions of graphene and analogues we refer to [81, 84].

3.1.5 Density of states

Density of states (DOS) in 2D crystal is the number of states of electrons in energy interval $\mathrm{d}E$ around the certain energy E per unit area

$$D(E) = \frac{g}{(2\pi)^2} \sum_i \int_{\mathrm{BZ}} \mathrm{d}^2\mathbf{k}\, \delta(\varepsilon_i(\mathbf{k}) - E) \tag{3.12}$$

where g is the degeneracy of electronic states.[4] An analytic expression for DOS in the vicinity of E_F can be obtained easily by inserting the expression (3.11) for the energy of electrons. For the conduction band (ε_+) the expression (3.12) yields [5]

$$D(E) = \frac{g}{2\pi} \int_0^{\infty} \mathrm{d}q\, q\delta(\hbar v_F q - E) = \frac{g}{2\pi\hbar^2 v_F^2} E, \quad E > 0. \tag{3.13}$$

As the electrons in graphene have a degeneracy of 4 (spin degeneracy is 2 and additional factor of 2 is due to pseudospin), using similar treatment for the valence

[4] Assuming the same degeneracy for all electron bands.

[5] The integration formally goes to infinity, but we must bear in mind that the linear dispersion holds only in the vicinity of E_F.

band (ε_-) we can express DOS for electrons in the vicinity of E_F as

$$D(E) = \frac{2}{\pi\hbar^2 v_F^2}|E|. \tag{3.14}$$

We conclude that as a consequence of linear dispersion near E_F the DOS in this energy interval is also a linear function of energy. The distinct electronic property of graphene can be deduced from Fig. 3.5 – it is a *semi-metal*, characterized by a fact that it does not show a bandgap but the DOS at E_F is zero. Moreover, from Fig. 3.5, it can be seen that Dirac approximation works well in the energy interval ~ 1 eV around E_F.

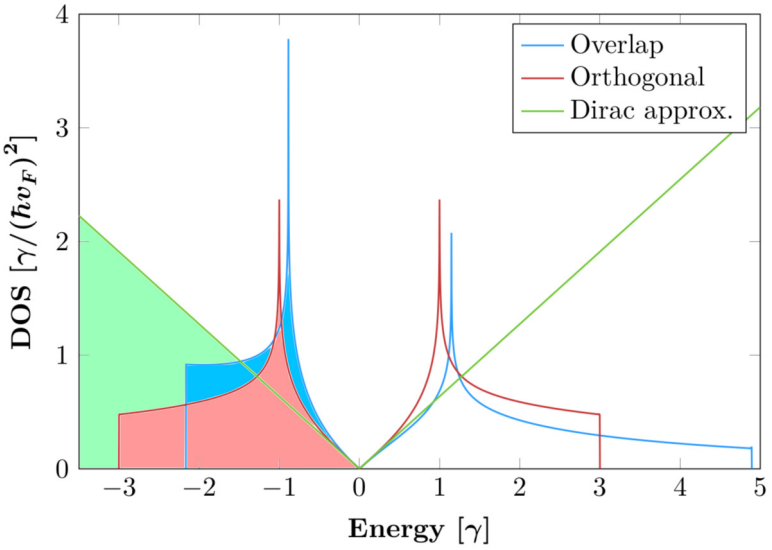

Figure 3.5: Graphene DOS calculated with the tight-binding method with zero energy at E_F. The plot has been made using values from [85]. The difference between the blue ($\gamma = 3.033$ eV, overlap integral $s = 0.129$) and the red line ($\gamma = 3.033$, no overlap $s = 0$) clearly represents the effect of the $2p_z$ orbital overlap on the electronic structure of graphene. DOS within the Dirac approximation is represented with a green line. Occupied states are filled with color. Adapted from [86].

3.2 Hexagonal boron nitride (h-BN)

Boron nitride (BN) is the lightest Group III-V compound. It exhibits various crystalline polymorphs analogous to carbon structure. For example, graphite and diamond, the two most common carbon allotropes, consist of sp^2-bonded graphene layers and sp^3 carbon atom network, respectively. In close resemblance to these structures, BN exhibits hexagonal (h-BN) and cubic (c-BN) polymorphs, which consist of layered and tetrahedral structures, respectively. From the former the

thermodinamically stable monolayers can be isolated by micromechanical cleavage method, similarly to graphene exfoliation from graphite.

Monolayer h-BN is composed of alternating boron and nitrogen atoms in a honeycomb lattice with a lattice constant of $a = 2.50$ Å, and a nearest-neighbor distance of 1.45 Å (Fig. 3.6a). As the electronic configuration of its atoms are B: [He]$2s^2 2p^1$ and N: [He]$2s^2 2p^3$, elementary cell of h-BN contains 12 electrons. Thus, h-BN is not only isostructural but also isoelectronic to graphene. Regardless of the geometrical similarities, h-BN shows strikingly different electronic properties from those of graphene. In the polar structures, such as h-BN, p_z orbital electrons are predominantly located on the atom with larger electronegativity. This removes the degeneracy of valence and conduction bands at K point and leads to bandgap opening. As the difference in the Pauling electronegativity of B (2.04) and N (3.04) is large, h-BN is ionic crystal and contrary to semimetallic graphene it is an insulator, exhibiting a direct K → K bandgap between 4.69 eV (PBE) and 7.92 eV (with the GLLB-SC quasi-particle correction) [87, 88].[6] Band structure of h-BN is shown in Fig. 3.6b.

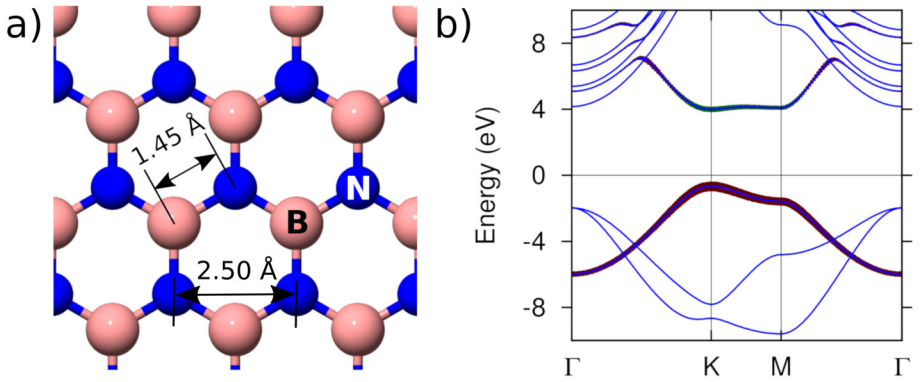

Figure 3.6: a) Crystal structure of h-BN. Boron atoms are represented with salmon orange spheres and nitrogen atoms with blue spheres; b) h-BN band structure calculated within the LAPW approach by applying PBEsol XC functional. Band colors represent their character: bands with predominately p_z character of N are in red, while that with p_z character of B are in green (unpublished results).

Due to the strong in-plane covalent B-N bonds and the absence of dangling bonds at surface, h-BN has excellent chemical and thermal stability with resistance to oxidation and to damage of high temperature up to approximately 1500 °C in air. It has a high dielectric breakdown field of 7.94 MV/cm, comparable to the breakdown fields of standard dielectrics, such as SiO_2. h-BN is regarded as a promising

[6] Many DFT XC functionals lead to gaps that are significantly below experimental values. This is a well-known problem in DFT approach and the great improvement has been made by better treatment of the non-local exchange. For details see [89, 90].

assistant material to enhance the performance of other 2D materials in nanodevices. Moreover, graphene/*h*-BN heterostructure serves as a platform suitable for studying many-body correlation effects of Dirac fermions in graphene, such as fractional quantum Hall effect in the high magnetic field [91].

3.3 Phosphorene

Black phosphorus (BP) is a rare allotrope of phosphorus, firstly sintesized a century ago from white phoshporus under high temperature and pressure [92]. It is much denser (2.69 $\mathrm{g\,cm^{-3}}$) than white (1.83 $\mathrm{g\,cm^{-3}}$) and red phosphorus (2.05 − 2.34 $\mathrm{g\,cm^{-3}}$) and can sustain up to 400 °C in air without spontaneous ignition in sharp contrast to highly flammable white phosphorus.

At normal conditions, bulk BP is a layered structure and resembles graphite. First studies of BP showed that it is an intrinsic *p*-type semiconductor with an energy gap of around 0.33−0.35 eV and hole and electron mobility of 350 and 220 $\mathrm{cm^2\,V^{-1}\,s^{-1}}$ at room temperature, respectively [93]. Angle-resolved photoemission spectroscopy measurements have confirmed a 0.2−0.3 eV direct bandgap [94]. Very recently single layer of black phosphorus known as *phosphorene* was mechanically exfoliated from bulk BP thus reviving interest in this material [95, 96].

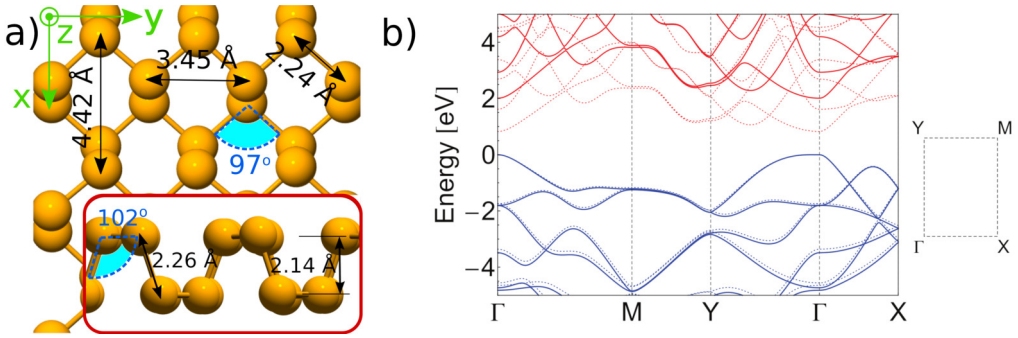

Figure 3.7: a) Crystal structure of phosphorene. High-symmetry directions, armchair (x) and zigzag (y), are presented in green. Each P atom is bonded with three neighboring atoms, two of which are in the same plane at 97° and the third is between the layers at 102°. Distances between P atoms and angles between bonds shown in this figure are obtained from DFT-PBE calculations; b) The DFT-calculated (dashed lines) and GW-calculated (solid lines) band structure of phosphorene. Zero is set to be at the top of the valence band (from [97]).

Phosphorene structure is markedly different from honeycomb graphene, as its atoms lie in two parallel planes making a form of a puckered (or buckled) sheet (Fig. 3.7a). For such structures, *buckling* is defined as a distance between two atomic planes. Each P atom in phosphorene is covalently bonded to the three neighbors

similarly to C atoms in graphene, but the sp^3 hybridization is the reason for the puckering, as four sp^3-hybridized orbitals so formed are directed towards the four corners of a tetrahedron with a P atom in its center.

Based on DFT calculations, Wei et al. found that the critical tensile strain of phosphorene in the X (armchair) and Y (zigzag) directions (Fig. 3.7a) are 30% and 27%, respectively. Such a large critical strain is undoubtedly associated with the unique structure of phosphorene. One of the most profound structural property of phosphorene is an inherent *in-plane anisotropy* which leads to the anisotropy of its mechanical properties, thermal conduction, optical detection as well as carrier transport [98].

First-principles calculations have confirmed the expectation that phosphorene bandgap is much larger compared to the bandgap of bulk BP, with the reported value between 0.8 eV (DFT result) and 2 eV (GW result) [97].[7] Though VBM is located slightly away from the Γ point and CBM is exactly at Γ point, we regard phosphorene as a direct-gap semiconductor as the difference between the VBM and energy at Γ point is less than 10 meV. The reason behind the discrepancy of 150% between the DFT and GW values, substantially larger than in other 2D semiconductors, is the highly anisotropic band structure of the lowest conduction band and highest valence band. Fig. 3.7b shows that the band dispersion is nearly flat along the Γ−Y direction with a large carrier effective mass of around $m_e \approx 2.6m_0$ and $m_h \approx 8.3m_0$ compared to the values $m_e \approx m_h \approx 0.3m_0$ found for Γ−X direction [**?**]. This confines particles to an effective 1D environment along the armchair direction, and the effective lower dimension contributes to a larger self-energy correction.

It was experimentally demonstrated for BP that the bandgap can be tuned monotonically from 0.3 eV to 1.0 eV when sample thickness is scaled down from bulk to single layer [96]. Furthermore, bandgap of phosphorene can be tuned by applying compressive strain. Kistanov et al. [99] showed that the compressive strain of up to −20% along the armchair direction reduces the bandgap from 0.84 to 0.51 eV, while further compression shows no significant effect; for ripples along the zigzag direction, semiconductor-to-metal transition occurs. For the comprehensive review of anisotropy in physical properties, as well as the utility of phosphorene in the field effect transistor technology, optoelectronic devices, gas sensors and batteries we refer to [98].

[7] Due to the surface oxydation, the preparation of a single layer phosphorene for ARPES measurement which would provide precise determination of the band structure is challenging [**?**].

3.4 Group XIV carbides – SiC, GeC and SnC

Carbides of group XIV elements, AC ($A = \mathrm{Si, Ge, Sn}$), are theoretically predicted to form an alternate arrangement of A and C atoms in a highly stable 2D honeycomb structure [100]. Thus, they are isostructural to h-BN (Fig. 3.6a), although nearest-neighbor distances and lattice constants are much larger than h-BN values (Table 3.1).

Table 3.1: Nearest-neighbor distances, d, lattice constants, a and cohesive energies per pair of atoms, E_c of SiC, GeC and SnC calculated within DFT-LDA approach. Values are taken from [100]. Bandgaps, E_G, within the DFT-LDA approach and G_0W_0-corrected values are from [101]. Symmetry points of BZ indicate where maximum (minimum) of valence (conduction) band occurs.

2D crystal	d(Å)	a(Å)	E_c(eV)	E_G(eV)	
				LDA	G_0W_0
SiC	1.77	3.07	15.25	2.57	3.88
				$\mathrm{K} \to \mathrm{M}$	$\mathrm{K} \to \mathrm{M}$
GeC	1.86	3.22	13.23	2.26	3.37
				$\mathrm{K} \to \mathrm{K}$	$\mathrm{K} \to \mathrm{K}$
SnC	2.05	3.55	11.63	1.71	2.43
				$\mathrm{K} \to \Gamma$	$\mathrm{K} \to \Gamma$

Despite the fact that single layers of AC materials are not yet experimentally isolated, there are direct experimental indications that 2D form of SiC may exist [102]. As a theoretical evidence for the structural stability of their monolayers, cohesive energies E_c per pair of atoms AC obtained within the DFT-LDA approach are comparable to that of graphene (20.08 eV) and h-BN (17.65 eV) (see values in Table 3.1). Calculations for variable lattice constants of buckled (or puckered) AC geometries confirmed that the planar structure is the most stable one. Furthermore, analysis of phonon modes which provide a reliable test for a structural stability, showed no imaginary phonon frequencies of SiC, GeC, and SnC [100].

In addition to structural similarity to h-BN, the electronic structures of these materials resemble that of h-BN. The reason for a bandgap opening at K point is the symmetry breaking due to the substitution of one C atom in the elementary cell with a Si (Ge, Sn) atom. Compared to large h-BN bandgap, the bandgaps of AC materials are smaller, and this discrepancy can be attributed to the smaller difference in the electronegativity of Si (Ge, Sn) and C than that between B and N. Thus, AC are semiconductors, but only GeC has a direct bandgap located at K point. SiC is an indirect-gap semiconductor with VBM at the K point and CBM

at the M point and SnC has VBM at K point and CBM at Γ point. Their band structures are presented in Fig. 3.8. Both the valence and the conduction bands

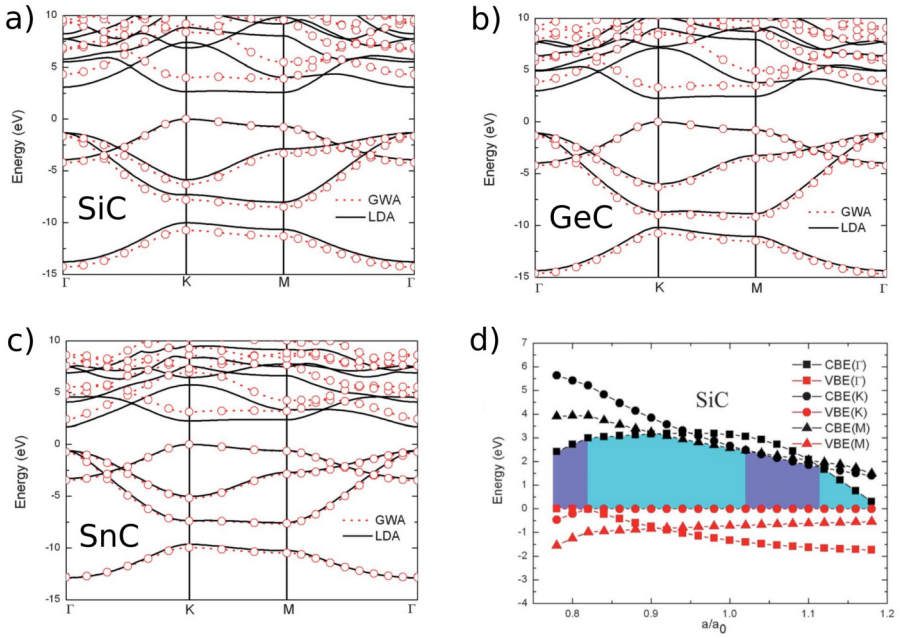

Figure 3.8: Electronic band structure of a) SiC, b) GeC and c) SnC. The DFT-LDA band structures are shown with a solid black line, and the G_0W_0 corrected band structures are presented with red circles connected with dotted lines; d) the valence and the conduction band energies of SiC at the Γ, K and M points for variable lattice constants, where a_0 is the equilibrium lattice constant. Blue (green) color indicates direct (indirect) bandgap for a certain lattice constant. Adapted from [101].

have predominantly Si (Ge, Sn) and C p-orbital character. From Fig. 3.8 it can be seen that the bands between the points K and M are nearly flat, indicating a large carrier effective mass in K–M direction.

The bandgaps of AC monolayers decrease in the sequence SiC → GeC → SnC (Table 3.1). Lü et al. speculated that the bandgaps of the AC are mainly determined by the interplay between the (1) repulsion of the valence band and the conduction band and (2) the delocalization effect due to orbital overlapping [101]. The reduction of the AC bond length enhances the repulsive effect and thus increases the bandgap, while on the other hand it causes broadening of both the valence and the conduction bands which decreases bandgap. For SiC, as the lattice constant increase from $0.78a_0$ to $0.91a_0$ (a_0 is the equilibrium lattice constant), the delocalization effect is dominant and bandgap increases. However, from $0.91a_0$ to $1.18a_0$ the bandgap decreases as the repulsive effect dominates. This results with an arch-shape modulation of the SiC bandgap under strain, as can be seen in Fig. 3.8d.

3.5 Transition metal dichalcogenides (TMDs)

Transition metal dichalcogenides (TMDs) are layered materials with electronic properties which promote them as main candidates for range of application – from nanoelectronics and nanophotonics to actuation and sensing at the atomic scale. The first paper with the description of their structure was published by Linus Pauling in 1923 [103]. By the end of the 1960s, around 60 TMDs were known, at least 40 of them with a layered structure [104]. In the last 15 years, the rapid growth of graphene-related research and the development of advanced techniques suitable for isolation of single layers from bulk samples brought TMDs back in the spotlight.

Generalized chemical formula of TMDs is MX_2, where M is a transition metal of groups IV-X and X is a chalcogen (S, Se, Te). TMD monolayer itself contains three atomic planes (X–M–X) which can adopt two structural phases based on the coordination of transition metal atom – *trigonal prismatic* (D_{3h} point group) or *octahedral* (D_{3d} point group) (see Fig. 3.9).

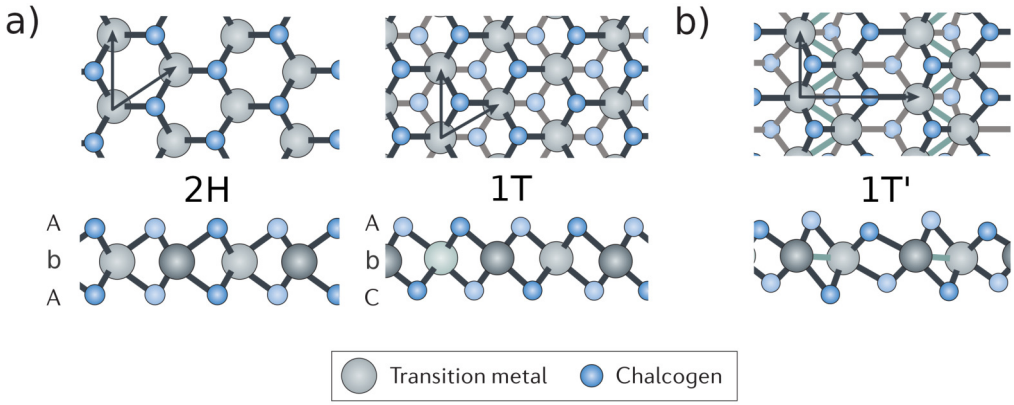

Figure 3.9: a) Structural phases of monolayer TMDs: trigonal prismatic (2H) and octahedral (1T); b) distorted octahedral (1T′) structural phase. Lattice vectors are represented with arrows. Adapted from [105].

Bulk TMDs, similarly to graphite, are layered materials with weak van der Waals forces between the layers. They can be found in several different *polytypes* depending on the type of stacking. The most common are *trigonal* (1T), *hexagonal* (2H) and *rhombohedral* (3R), where the digit indicates the number of layers in the stacking sequence. For example, the most abundant phase of MoS_2 is 2H with the stacking sequence AbA BaB, where capital (lower case) letters stand for chalcogen (transition metal) atoms. We point out that the structural phase of all layers within a polytype is the same – for 1T it is trigonal prismatic whereas 2H and 3R polytypes have octahedral coordination of transition metal atom.

Electronic properties of bulk TMDs are distinct – ranging from insulators such as HfS_2, semiconductors such as MoS_2 and WS_2, semimetals such as WTe_2 and $TiSe_2$, to metals such as NbS_2 and VSe_2 [106]. Moreover, some TMDs exhibit low-temperature phenomena including superconductivity, *charge density wave* (CDW – a periodic distortion of crystal lattice) and Mott transition (metal to non-metal phase transition) [107, 108, 109, 110]. Structural phases together with the observed electronic properties of the most common TMDs are presented in Fig. 3.10.

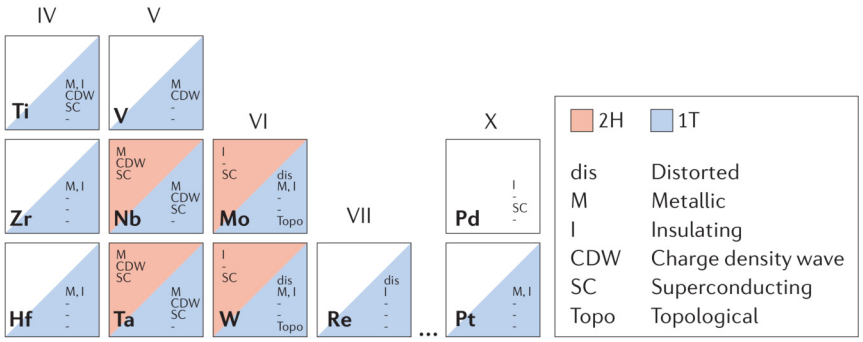

Figure 3.10: The periodic table with the basic structural and electronic properties of bulk TMDs. Adapted from [105].

Now we will focus our attention on monolayer TMDs. Exfoliation of single layers of TMDs mainly preserves the electronic properties of their bulk counterparts, though the confinement effects due to reduced dimensionality lead to additional characteristics [111, 112, 113]. Based on their structural phase, they will be referred to as 2H-MX_2 (trigonal prismatic) and 1T-MX_2 (octahedral) (see Fig. 3.9).[8] In both 2H and 1T phases, the non-bonding d bands of the TMDs are located between the bonding (σ) and antibonding (σ^*) bands which arise from the M–X bonds.

The electronic structure strongly depends on: (1) the coordination environment of the transition metal, and (2) the number of its d electrons [114]. Due to *the crystal field*, trigonal prismatic coordination of transition metal atoms leads to the formation of three groups of d orbitals – d_{z^2}, $d_{x^2-y^2,xy}$ and $d_{xz,yz}$ with a considerable bandgap between the first two groups. On the other hand, when a transition metal atom is surrounded by chalcogen atoms situated in the vertices of octahedron, d orbitals split into two groups – doubly degenerate d_{z^2,x^2-y^2} (e_g) and triply degenerate $d_{yz,xz,xy}$ (t_{2g}). In both cases, the diversity in the electronic properties of TMDs, presented in Fig. 3.10, stems from the progressive filling of the non-bonding d bands from group IV to group X. Thus, materials with the partially filled d orbitals, as in the

[8] The indices which label the number of layers in a stacking sequence of bulk TMDs are now redundant, but they are frequently retained in the literature.

case of 2H-$NbSe_2$ and 1T-$ReSe_2$, exhibit metallic conductivity. On the contrary, fully occupied orbitals, such as in 1T-$HfSe_2$, 2H-$MoSe_2$ and 1T-$PtSe_2$, result in the semiconducting material.

Compared to the impact of metal atoms, the effect of chalcogen atoms on the electronic structure is less profound but the trend is still observable. The chalcogen atoms cause broadening of the d bands. Thus, the bandgap decreases along the chalcogen group. The first-principles calculations have confirmed the gradual decrease, as LDA (G_0W_0) bandgaps of 2H-MoS_2, 2H-$MoSe_2$ and 2H-$MoTe_2$ are 1.58 (2.48), 1.32 (2.18) and 0.93 (1.71), respectively [115].

For a range of TMDs, one phase is thermodynamically more stable than the other, but the metastable phase can be obtained by various manipulations. For example, the transition of semiconducting 2H-MoS_2 to the metallic 1T polymorph can be achieved by mechanical deformation [8] or by adsorption of alkali metals [104, 116, 15]. Destabilization of the 2H phase due to the adsorption of alkali metals is caused by (1) the change in the d-electron count as the valence s electron is transferred from alkali metal atom to the transition metal atom and (2) the relative change in the free energy of the two phases. Moreover, recent studies have shown that the structural change of MoS_2 can be partial, resulting with the formation of coherent 2H-1T interfaces [117, 118]. The opposite scenario of 1T $\rightarrow$ 2H transition is reported for TaS_2 on Li intercalation [119]. In Fig. 3.10 transition metals which can exhibit both phases are represented with two-color squares.

Apart from the 2H $\rightarrow$ 1T structural phase transition, several group VI TMDs undergo a distortion of the crystal lattice that lower the periodicity of the 1T phase. The pronounced distortion results in the additional metal-metal bonds which can lead to the dimerization of the 1T phase. The so-called 1T$'$ (Fig. 3.9b) phase is formed under certain conditions owing to instability in the electronic structure of the 1T phase [120, 121]. The microscopic mechanism behind the 1T $\rightarrow$ 1T$'$ transition is believed to be the Jahn-Teller effect, in which the splitting of the partially filled degenerate d orbitals lowers the total energy [121]. This distortion is reminiscent of CDW phases of group V TMDs which are typically stable at low temperatures ($< 120\,\mathrm{K}$ for $TaSe_2$ and $< 40\,\mathrm{K}$ for $NbSe_2$) [109], but this lattice distortion has been observed at room temperatures for Li-intercalated MoS_2 and WS_2 [118]. Not less intriguing is the fact that the 1T$'$ phase is metastable even after the intercalant is removed [122].

To conclude the discussion, we will take a closer look at the electronic properties of semiconducting 2H-MoS_2, which is widely considered as one of the most promising TMDs for future electronic devices [13]. Its bandgap can be tuned by reducing its

thickness from bulk to monolayer as shown in Fig. 3.11. The bandgap gradually increases from bulk to monolayer, with the corresponding values of 0.88 eV and 1.71 eV, respectively [123]. The experimental value for the bandgap of monolayer 2H-MoS_2 is 2.16 eV [124]. Moreover, bulk 2H-MoS_2 is an indirect-gap semiconductor

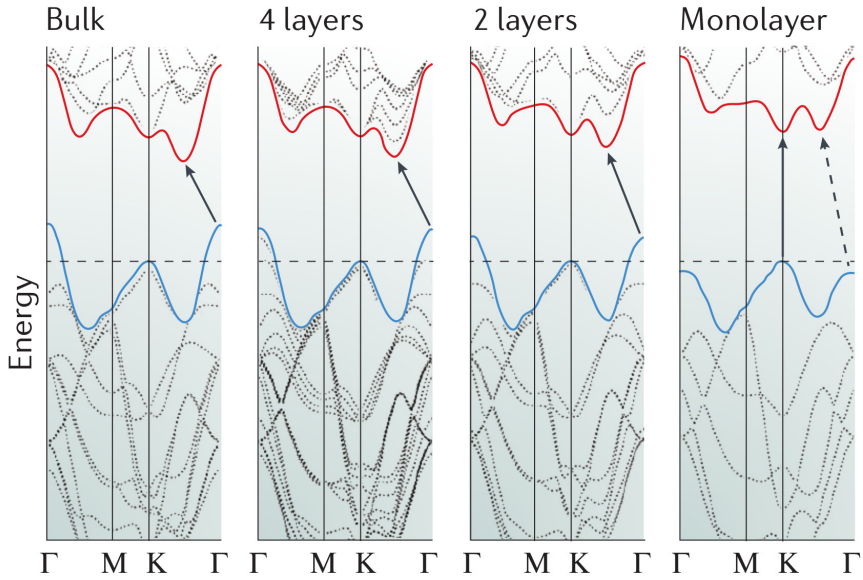

Figure 3.11: Band structure of 2H-MoS_2 calculated within DFT-GGA approach for samples of decreasing thickness. Lowest energy transitions are indicated with solid arrows. Adapted from [123].

with VBM at Γ point and CBM at the midpoint along Γ–K direction, while the monolayer 2H-MoS_2 is a direct-gap semiconductor with VBM and CBM at the K point. Monolayers of all the group VI TMDs have in common that their VBM and CBM are located at the corners of the hexagonal BZ (see Fig. 3.2b). This property opens the possibility for the observation of valley-dependent physics and, in further perspective, the application in the valleytronic devices.

Chapter 4

Growth of metals on graphene

This chapter is devoted to the initial stages of growth of metallic structures on graphene. We selected lithium (Li), calcium (Ca) and titanium (Ti) as representatives of three groups of metals, namely – alkaline, alkaline earth, and transition metals. Based on the atomic-scale description of the interaction between their adatoms we rationalized the tendency of metals to form clusters on graphene. For metals which show a strong preference for clusterization, comparison of the total energies of their few-atoms clusters adsorbed on graphene clarifies their preference towards the formation of 2D or 3D nanostructures on graphene.

Particularly interesting properties were found for Ca adsorbed on graphene. Moderate attractive interaction between Ca adatoms on graphene is a driving force for the formation of 2D structures of Ca on graphene. We provide a detailed description of the electronic properties of the monolayer and bilayer graphene functionalized with Ca as such materials show great promise in the engineering of high quality contacts in vertical heterostructures of 2D materials.

4.1 Introduction

Since the discovery of graphene, studies of its structural and electronic properties were accompanied the search for the potential applications of this 2D material in future nanotechnologies. For the development of efficient graphene-based electronic devices of critical importance is the high-quality junction between graphene and metallic contacts. Xia et al. argued that the factors that determine the resistance of metal-graphene junction remain unclear as the measurements of contact resistance have been inconsistent [125]. They found at 6 K an anomalous temperature dependence in a palladium-graphene junction as it drops abruptly to a value of just $110 \pm 20\,\Omega$, which is few times the minimum achievable resistance. For the thorough understanding of such behavior, of high priority is the atomic scale description of

metal-graphene interaction.

Depending on the strength of the interaction of metal atoms with graphene and the nature of interaction among metal atoms themselves, they form either smooth ultra-thin films on graphene or 3D nanostructures with strikingly different electrical contacts. The prediction of the growth mode of metals on graphene can be made already from the insights which the study of their small clusters can give. Besides, due to its chemical inertness graphene is a suitable template for the growth of metal nanoclusters used as model catalysts [126]. Structural properties of metal clusters, i.e. the size and the shape, substantially affect their catalytic activity.

Another potential application of 2D materials which draws special attention is their usage in the design of materials for hydrogen storage. It is well known that pristine carbon structures cannot adsorb a large amount of hydrogen [127], therefore the *functionalization* of graphene with metal atoms is considered as a promising method to increase the number of adsorbed H_2 molecules. Recent DFT studies of Ti-decorated single-walled carbon nanotubes (SWCNTs) [128], C_{60} molecules decorated with Ti, Sc and V atoms [129] and graphene doped with Al atoms [130] all assumed that metal atoms are individually dispersed across carbon surfaces. Although the individual binding of metal atoms on a surface is necessary to achieve full hydrogen storage capacity, this binding picture is not always easy to achieve. For instance, Sun et al. [131] reported the tendency of Ti atoms to cluster at C_{60} and Krasnov et al. [132] reported that Sc atoms form clusters on small SWCNTs. In cases like these, the tendency for clustering is driven by the metal-metal attraction, which is much stronger than the interaction of metal atoms with carbon surface.

Cohen and co-workers [133] performed the first systematic DFT study of the binding of metal atoms at graphene. They used *the cohesive energies* of bulk metals (E_C) as a measure of the strength of metal-metal interaction and compared their values with *the binding energies* (E_B) of individual metal atoms adsorbed on graphene. They argued that the shape and geometry of structures formed by metal atoms upon adsorption on graphene can be guessed from the E_B/E_C values. According to their reasoning, metals with high E_B/E_C values show tendency for wetting the surface, while the ones with small E_B/E_C ratio form closely packed 3D clusters. The values of E_B/E_C for a range of metals calculated by applying GGA-PBE XC functional are represented in Fig. 4.1a.[1]

Their assumption is partly supported by the study of the adsorption of alkali metals on graphite [135]. Furthermore, Pulido et al. [134] showed that gold, repre-

[1] Unpublished results from our calculations. Values from [133] only slightly differ from the values presented in Fig. 4.1.

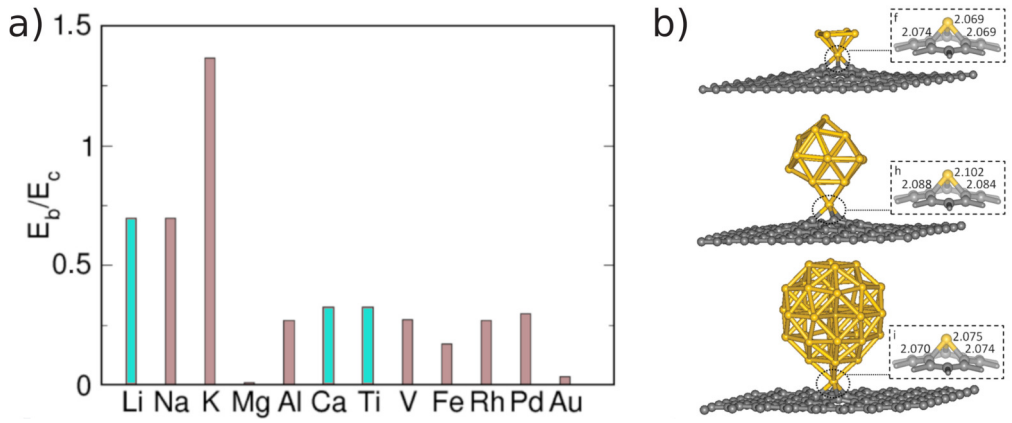

Figure 4.1: a) Ratio between binding energy of metal atoms on graphene (E_B) and their bulk cohesive energy (E_C) calculated with GGA-PBE XC functional (unpublished results). Metals which we further consider in our study are shown in green; b) Gold clusters with 5, 19 and 39 atoms supported on the graphene sheet. Geometries are optimized within DFT approach, with the usage of GGA-PW91 functional. Adapted from [134].

sentative of metals with small E_B/E_C values, form compact 3D clusters on graphene, as shown in Fig. 4.1b. However, the values of cohesive energies in metal clusters are generally much smaller than the corresponding bulk value. For instance, calculated cohesive energy of a gas-phase Ti dimer is 1.47 eV/atom, significantly smaller than the bulk value found for *hcp* Ti crystal of 5.29 eV. It is worth noting that alkali metals have the highest E_B/E_C ratio and gold has by far the lowest and there are plenty of metals with intermediate E_B/E_C values (Fig. 4.1a). Hence, the prediction of growth mode of nanostructures formed upon deposition of metal atoms on graphene based solely on the E_B/E_C ratio can be considered only as a rough guess. For an accurate description of preference for 2D or 3D growth of metals a more subtle approach must include not only individual metal atoms on graphene but also their small clusters.

We selected three metals – Li, Ca and Ti – as typical representatives of adsorbates with markedly different adsorption behavior. From a microscopic picture of the interaction between metal adatoms combined with the structural properties of their small clusters, we provide a detailed description of the structural and electronic properties of metal nanostructures formed on graphene. For Li atom on graphene, we applied a simple model to include the long-range electrostatic repulsion between Li adatoms from neighboring unit cells in the estimate of the binding energy. In addition to this, we report a novel structure of graphene functionalized with Ca atoms adsorbed in a monolayer arrangement and get insights into the origin of the enhanced adhesion in bilayer graphene induced via Ca intercalation.

4.2 Metal adatoms on graphene

We start the discussion on the metal adsorption on graphene with the definitions of physical quantities which will be often used in further discussion. For additional information on computational details, e.g. choice of the XC functional, division of the BZ, structure optimization algorithm etc. see Appendix C.

- *The binding energy* of metal cluster M_n at graphene, where $M = \mathrm{Li}, \mathrm{Ca}, \mathrm{Ti}$ and n is the number of atoms, is defined as

$$E_{\mathrm{B}}(M_n) = nE(M) + E(G) - E(M_n/G), \tag{4.1}$$

  where $E(M)$, $E(G)$ and $E(M_n/G)$ are total energies of free metal atom, pristine graphene (per unit cell) and metal cluster M_n on graphene, respectively. Thus, the binding energy of metal adatom is obtained as $E_{\mathrm{B}}(M) = E(M) + E(G) - E(M/G)$.

- *The adhesion energy*, as a measure of energy gained upon deposition of metal cluster on graphene from gas phase, is defined as

$$E_{\mathrm{ad}}(M_n) = E(M_n) + E(G) - E(M_n/G), \tag{4.2}$$

  where $E(M_n)$ is the total energy of isolated gas-phase cluster.

- To estimate the strength of the interaction between adsorbed metal atoms we define *the interaction energy* as follows

$$E_{\mathrm{int}}^{\mathrm{M-M}} = E_{\mathrm{B}}(M_2) - 2E_{\mathrm{B}}(M). \tag{4.3}$$

  The positive (negative) value of $E_{\mathrm{int}}^{\mathrm{M-M}}$ corresponds to the repulsive (attractive) interaction between adsorbates, while the strength of the interaction is proportional to the absolute value of $E_{\mathrm{int}}^{\mathrm{M-M}}$.

The simplest sistem which can be adsorbed on graphene surface is an individual atom. We used 6×6 unit cell with 72 C atoms to simulate the adsorption of metal adatoms and small metal clusters (dimers, trimers and tetramers) on graphene surface (Fig. 4.2). Our tests showed that the further increase of the unit cell size has a minor effect to the structural and electronic properties of adsorbates. Three distinguishable adsorption sites are considered: (1) on top of C atom (T site), (2) between adjacent C atoms (B site) and (3) above the center of the hexagon (H site) (see Fig. 4.2). For all three considered metals we found the preference for adsorption

at H site. This behavior is already reported for Li, Ca and Ti in [133] and our results just confirm their findings. Besides, the displacements of C atoms are small and do not exceed 0.05 Å irrespective of the adsorbed metal. The distances between metal adatoms adsorbed at H site and the graphene sheet are shown in Table 4.1.

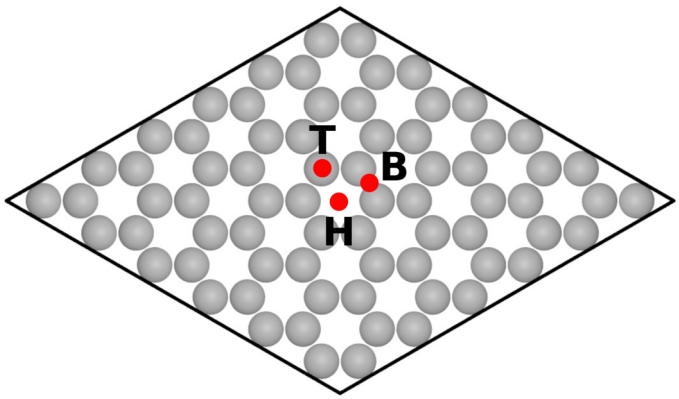

Figure 4.2: The unit cell with 72 C atoms. Different adsorption sites are denoted: hollow (H), bridge (B) and on-top (T).

We compared the binding energy of metal adatom with the cohesive energy of bulk metal calculated for the most stable crystal structure. For Li it is body-centered cubic (*bcc*) lattice, for Ca face-centered cubic (*fcc*) lattice and hexagonal close-packed (*hcp*) lattice for Ti [33]. The corresponding values for E_C, E_B, their ratio E_B/E_C together with the electron charge transfer from metal adatoms to graphene obtained from Bader analysis [136] are given in Table 4.1.

Table 4.1: Structural and energetic properties of metal adatoms for the hollow site. The properties listed are distances between metal adatoms and the graphene plane (h) and the corresponding binding energies (E_B), cohesive energies of bulk metals (E_C), ratio between the binding and cohesive energies (E_B/E_C) and the electron charge transfer from adatoms to graphene (ΔQ).

Atom type	Li	Ca	Ti
h(Å)	1.71	2.30	1.84
E_B(eV)	1.16	0.55	1.52
E_C(eV)	1.65	1.94	5.29
E_B/E_C	0.70	0.28	0.29
ΔQ(e)	0.90	0.89	0.92

Driven by the high E_B/E_C parameter Li atoms on graphene arrange into dispersed 2D layers, as already reported in previous studies [133, 135]. This is a general trend for alkali metals on graphene and we chose Li as a representative for further description of interaction of alkali metals with graphene.

Small E_B/E_C values found in Mg, some transition metals and noble metals [133] indicate much stronger metal-metal binding compared to the metal-graphene interaction. Consequently, when adsorbed on graphene, these metals tend to maximize the number of metal neighbors in the structures they form. Hence, they are likely to gather into compact 3D clusters. Recently, the experimental study of Zan et al. [137] confirmed the clustering of Fe and Cr atoms on single-layer graphene sheet. We will describe in detail the interaction of transition metal atoms with graphene taking Ti as a typical representative.

The E_B/E_C value of Ca is close to that found in transition metals, as reported in [133] and confirmed by our calculations (Table 4.1). Yet, Lee et al. [138] showed that Ca adatoms prefer to bind individually on zig-zag edges of graphene nanoribbons. Therefore, it is arguable whether the conclusions on trends in metal binding on graphene can be drawn solely from the E_B/E_C ratio. We provide a more accurate description of clustering of Ca adsorbates on graphene based on (1) the considerations of Ca dimers, trimers and tetramers and (2) interaction between Ca adatoms. In addition to this, we describe a novel 2D structure with Ca coverage of 1/6 monolayer [139], confirmed by our calculations as very stable.

4.3 Interaction between metal adatoms

The shape and the type of the thermodynamically stable structures formed upon deposition of metal adatoms on graphene critically depend on the interaction between adsorbates. We evaluated the interaction energy of metal dimers on graphene from eq. (4.3) for four dimer configurations with distances 2.47 Å, 4.26 Å, 4.91 Å and 6.51 Å as depicted in Fig. 4.3a-d, respectively. Along with the calculations of metal dimers with fixed bond length, for metals with an attractive interaction between adatoms, that is Ca and Ti, we performed additional calculations on their dimers adsorbed on graphene with unconstrained geometry optimization.

In conjunction with the considerations on Ca and Ti dimers, we performed calculations on their trimers and tetramers in order to find the most stable adsorption geometries of these clusters. Trimers are used to examine the tendency of metals for wetting the surface. When the growth morphology of metal nanostructures is inquired, tetramers are the smallest clusters where one can inspect the preference for either 2D or 3D growth. Therefore, if the preferred geometry of tetramer adsorbed on graphene is planar rhombohedral, the metal has a tendency towards 2D growth. On the contrary, tetrahedral adsorption geometry is a clear evidence of 3D growth.

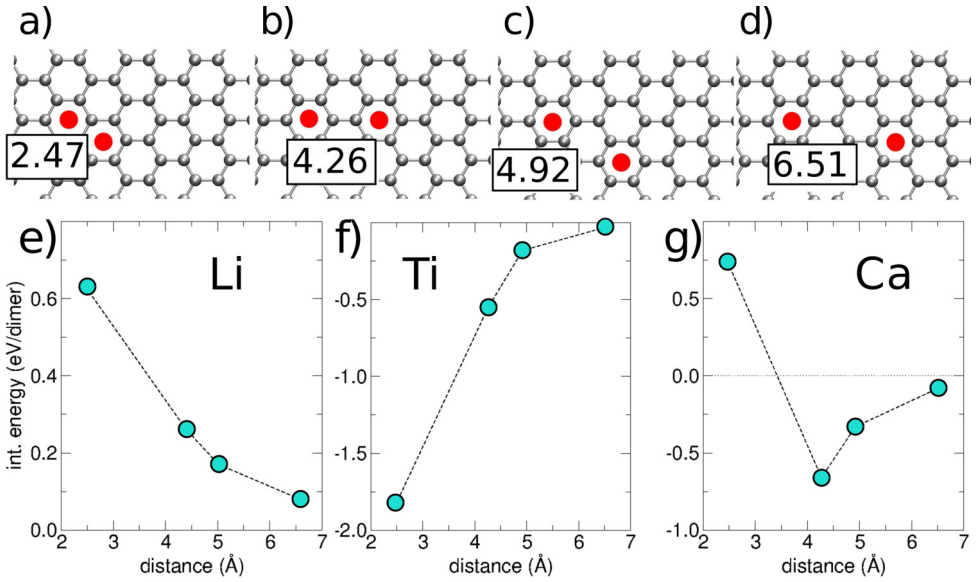

Figure 4.3: a)-d) Dimer configurations with the corresponding distances between metal adatoms in angstroms; e) lithium, b) titanium and c) calcium interaction energies.

4.3.1 Lithium adsorption on graphene

High E_B/E_C value of Li (Table 4.1) and of alkali metals in general [133] shows that these atoms are very unlikely to form clusters upon their deposition on graphene. Therefore, we did not further consider Li clusters on graphene.

In Fig. 4.4 the DOS of the pristine graphene is compared with that of the graphene with Li adatom adsorbed at the H site. Atomic-orbital projected DOS presented in Fig. 4.4 shows that Li-2s valence state is completely empty, thus proving that the electron from Li-2s state is transferred to the lowest unoccupied states of pristine graphene. We performed Bader charge analysis which confirmed that 0.9 electrons are transferred from Li adatom to graphene (Table 4.1). Our calculations show no spin polarization of graphene substrate upon deposition of Li atom, as the transferred electron is delocalized across the surface thus filling both spin channels equally. The cone-shaped DOS near E_F specific to graphene is preserved, but the E_F is shifted higher in energy due to the presence of an additional electron.

From calculated interaction energies of Li dimers, Fig. 4.3e, we found that the Li-Li interaction is always repulsive as the Li adatoms on graphene are positively charged. Due to *periodic boundary conditions* (PBC) imposed within graphene plane long-range electrostatic repulsion between Li adatoms from neighboring cells results in the strong variation in the binding energy E_B as a function of the unit cell size. We obtained E_B from the calculations performed using $n \times n$ rhombohedral cell, where $n = 3 - 8$. Thus, as the Li-Li distance increases from 7.38 Å to 19.68 Å the

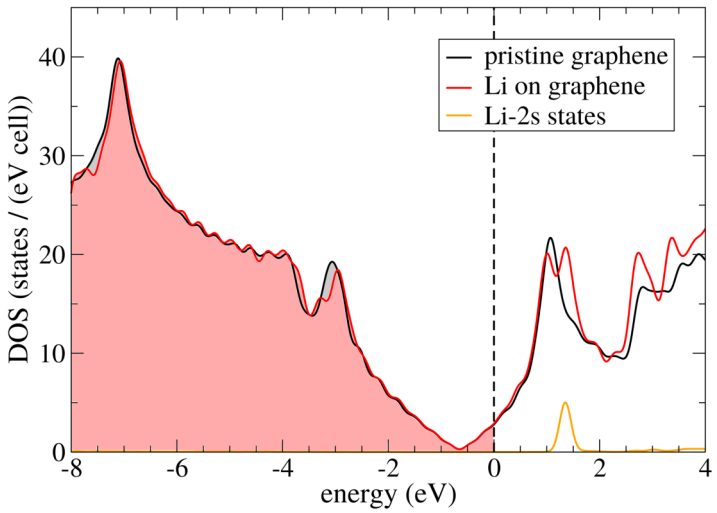

Figure 4.4: Total DOS of pristine graphene (black), graphene with adsorbed Li atom at H site (red) and the atom-projected DOS for Li-2s state (orange). DOS of pristine graphene is shifted in energy scale to match the DOS of Li atom adsorbed on graphene. Zero of the energy scale is set at the Fermi level of Li atom adsorbed on graphene.

binding energy approaches the value which corresponds to the infinite unit cell size, E_∞. We fitted the obtained DFT-PBE results to a curve that closely resembles the screened Coulomb potential,

$$E_{\mathrm{B}}(r) = E_\infty - \alpha \frac{\mathrm{e}^{-\beta r}}{r}, \tag{4.4}$$

where r is the distance between Li adatoms from the neighboring cells. The values of parameters $\alpha = 7.29$ eV and $\beta = 0.11$ best fit the binding energy. The DFT-PBE values for E_{B} together with the fitting function are shown in Fig. 4.5.

Thus, Li binding energy calculated employing PBC can be considerably underestimated if calculations are performed on the small unit cells with imposed in-plane PBC. Khanta et al. [140] performed DFT-LDA calculations for a variable unit cell size and found an increase in Li binding energy of 0.66 eV when the unit cell is doubled from 4.88 Å to 9.76 Å. Latter studies [141, 142] confirmed a strong variation in the binding energy depending on the unit cell used to model graphene surface. Therefore, an accurate picture of the binding of Li adsorbates on graphene should account for the long-range electrostatic repulsion. A simple approach to include this interaction is to apply eq. (4.4) and estimate the binding energy as E_∞ for $r \to \infty$.

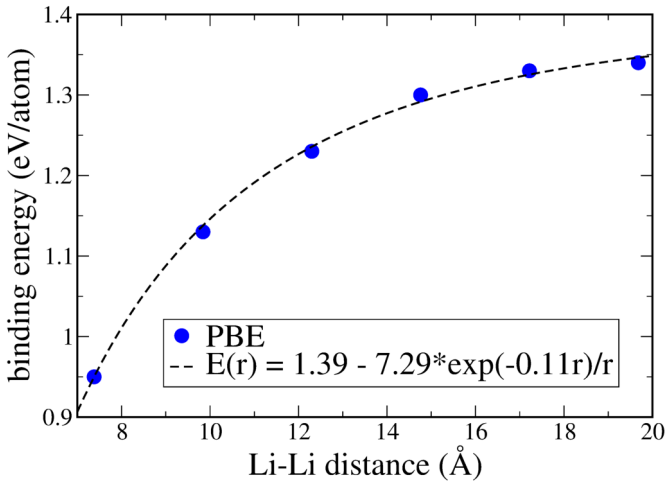

Figure 4.5: Variation of Li binding energy on graphene with the distance between adatoms from neighboring unit cells.

4.3.2 Titanium clusters on graphene

Titanium, a representative of the transition metals, has an intermediate E_B/E_C value (Table 4.1), much smaller than the value of Li but much larger than the values of noble metals (see Fig. 4.1a). Thus, the firm prediction of Ti growth on graphene requires additional considerations.

Far the most favorable Ti dimer configuration on graphene is the one with Ti atoms chemisorbed in the centers of adjacent carbon hexagons, as depicted in Fig. 4.6a, with binding energy of 2.43 eV/atom and Ti-Ti distance of 2.37 Å (see Table 4.2). The length of Ti_2 in this configuration is slightly shorter than the dis-

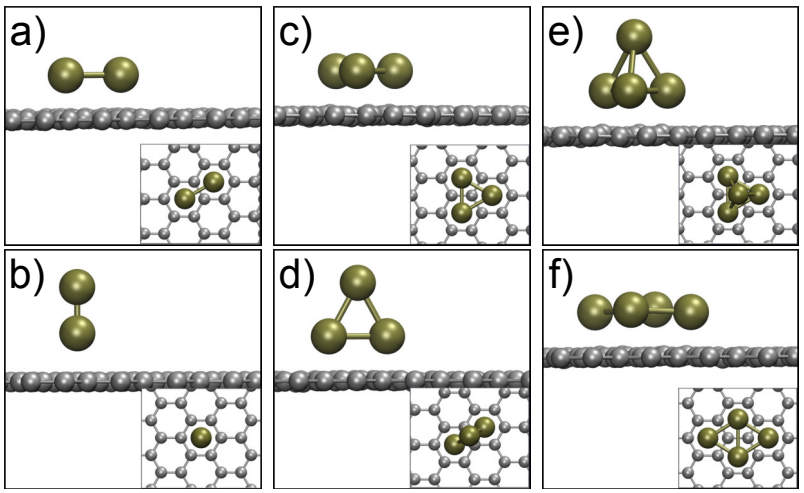

Figure 4.6: Ti dimers a-b), trimers c-d) and tetramers e-f) on graphene. Ti and C atoms are shown as dark green and gray spheres, respectively. The most stable adsorption geometries for small Ti clusters are presented in the upper panel.

tance between centers of the adjacent hexagons as Ti atoms tend to come closer to each other and recover the length of the gas-phase Ti_2, which is 1.94 Å [143].

In addition to the parallel-to-plane adsorption geometry, Ti_2 can be adsorbed perpendicularly to surface (Fig. 4.6b). Xiao et al. reported that bonding of Co dimers on hexagonal carbon rings results in a perpendicular arrangement of the dimers with respect to the carbon plane [144]. Our calculations show that perpendicular adsorption geometry of Ti_2 is not stable, as the binding energy is 1.30 eV (0.65 eV/atom) lower than the one of Ti_2 parallel to graphene plane due to the lack of the second contact point to the surface. Thus, in further inspection of Ti dimer adsorption, we will take into account only configurations where both Ti atoms are lying on the graphene surface.

Considerations on Ti dimers of variable length clearly show that the interaction between Ti adatoms on graphene is *strong*, *attractive* and *short-ranged* (see Fig. 4.3f), as the interaction energy obtained from eq. (4.3) is negative for all dimer lengths. According to our calculations, when Ti-Ti distance increases from 2.47 to 4.26 Å, the absolute value of interaction energy reduces greatly from 1.84 to 0.55 eV, and for larger distances it steeply diminishes as depicted in Fig. 4.3f. Finally, if the dimer length is larger than 6 Å, the interaction between Ti atoms is negligible.

Table 4.2: Binding energies (E_B), adhesion energies (E_{ad}), average intra-cluster bond lengths of Ti dimers, trimers and tetramers on graphene and the largest out-of-plane displacements of C atoms (Δz) when a particular metal cluster is adsorbed. The corresponding adsorption geometries are presented in Fig. 4.6. Note that the energies are expressed per metal atom.

Cluster type	Adsorption geometry	E_B (eV/atom)	E_{ad} (eV/atom)	M-M bond length (Å)	Δz (Å)
Ti_2	Fig. 4.6a	2.43	0.97	2.37	0.06
Ti_2	Fig. 4.6b	1.78	0.31	1.96	0.04
Ti_3	Fig. 4.6c	2.91	1.11	2.48	0.13
Ti_3	Fig. 4.6d	2.67	0.88	2.52	0.08
Ti_4	Fig. 4.6e	3.15	0.74	2.62	0.16
Ti_4	Fig. 4.6f	2.97	0.79	2.57	0.13

In Table 4.2 we also included adhesion energies (E_{ad}) of small Ti clusters obtained from eq. (4.2). The adhesion energy is expected to decrease with the increase of cluster size due to reduced reactivity of bigger clusters compared to the smaller ones. With the increase in cluster size the coordination number of metal atoms is approaching the value of bulk metal, thus chemical bonds are becoming saturated. Furthermore, the ratio of the number of atoms in direct contact with the surface and

the total number of atoms in cluster is decreasing as the cluster is growing. However, in small clusters which contain only a few atoms deviations from this trend often occur. This is the case for Ti, as the adhesion energy of Ti_2 parallel to the surface is 0.14 eV lower than of the Ti_3 adsorbed as depicted in Fig. 4.6c.

In addition to strong Ti-Ti interaction which drives the increase in the number of bonds in Ti clusters, Ti adsorbates on graphene will also optimize the number of bonds to the surface. The insights from the adsorption of Ti trimers confirm this tendency (Fig. 4.6c-d). The interaction of Ti atoms with graphene is of comparable strength to the Ti-Ti interaction in small clusters. Trimer in the Fig. 4.6c has all of its atoms in direct contact with the surface, adsorbed in the centers of the neighboring hexagons. It is the most stable trimer configuration, with the binding energy of 2.91 eV/atom. When adsorbed perpendicularly to graphene plane, as depicted in Fig. 4.6d, Ti_3 misses one contact point which give rise to 0.24 eV/atom smaller binding energy. For the sake of completeness, we inspected linear Ti trimer and found that it is highly unstable in gas phase as its total energy is 1.13 eV (0.38 eV/atom) higher than the total energy of triangular Ti_3. Hence, we did not include linear Ti trimers in further considerations.

The expected tendency of 3D growth is confirmed after the investigation of structural properties of Ti_4 – the smallest clusters which can be used to probe the preference for either 2D or 3D adsorption. We found that upon deposition on graphene, tetrahedral Ti_4 (Fig. 4.6e) is 0.72 eV lower in energy than the energy of the planar Ti_4 (Fig. 4.6f). Compared to the favorable Ti_3 adsorption geometry (Fig. 4.6c), Ti_4 depicted in Fig. 4.6e has an extra Ti atom above the center of the Ti triangle which results with three additional Ti-Ti bonds. On the other hand, planar Ti_4 has one additional Ti atom in direct contact with the surface but has one less Ti-Ti bond than the tetrahedral Ti_4. We conclude that the planar adsorption geometry is highly unfavorable due to preference of Ti clusters to maximize the number of internal bonds at the cost of less atoms on graphene surface.

Therefore, the strong attractive metal-metal interaction is the driving force for 3D clustering of Ti on graphene. Note that the adhesion energy of planar Ti tetramer is larger than that of tetrahedral cluster (Table 4.2) due to noticeably higher total energy of the planar Ti_4 in gas phase. Our calculations showed that the tetrahedral Ti_4 in gas-phase is 0.90 eV lower in total energy than its planar counterpart. Though the planar geometry of Ti_4 adsorbed on graphene has one more atom on the surface compared to the tetrahedral isomer, the strength of Ti interaction with graphene is insufficient to break Ti-Ti bonds in tetrahedral Ti_4 and thus flatten its structure.

The final note of this subsection is dedicated to other transition metals. As the

binding picture of their adatoms is found to be qualitatively the same as that of Ti [133], we expect that all of them are likely to form similar 3D islands on graphene.

4.3.3 Calcium clusters on graphene

Calcium atom, as a representative of the alkali-earth metals, has two valence electrons in its ground state occupying $4s$ orbital. This gives rise to the qualitatively different binding picture than that of transition metals, where the dominant role in the binding is played by d electrons. Therefore, even though the E_B/E_C of Ca is nearly equal to the value found for Ti (see Table 4.1), the structural properties of Ca adsorbates could differ substantially from those of transition metals.

Similarly to the study of Ti, we started our account on Ca clusters with the pursuit for the most stable dimer configuration. Parallel-to-plane adsorption geometry depicted in Fig. 4.7a with the bond length of 3.65 Å is far more favorable than the perpendicular dimer configuration with bond length of 3.79 Å, shown in Fig. 4.7b. The binding energy of the former is 0.99 eV/atom, noticeably higher than 0.61 eV/atom which is the binding energy of the later (Table 4.3).

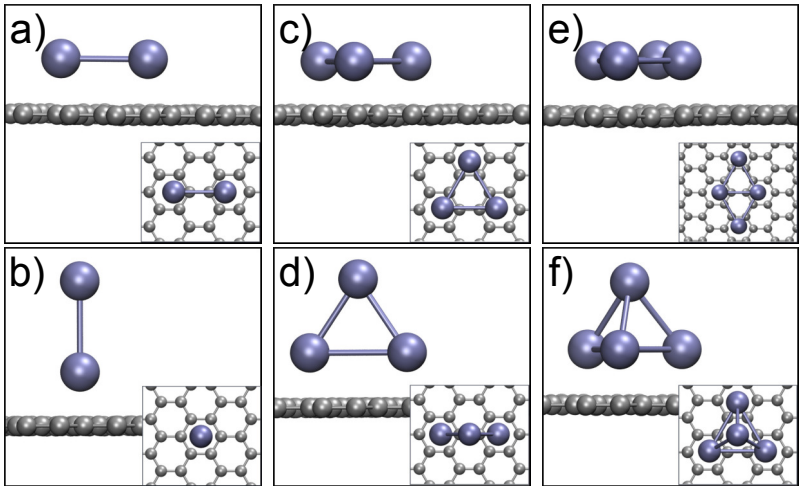

Figure 4.7: Ca dimers a-b), trimers c-d) and tetramers e-f) on graphene. Ca and C atoms are shown as ice-blue and gray spheres, respectively. The most stable geometries are presented in the upper panel.

The dependence of interaction energy on dimer length (Fig. 4.3g) clearly shows the substantial difference in the nature of the interaction of Ca adatoms from that of Ti (Fig. 4.3f). We found very strong repulsion between Ca adatoms at the distance of 2.47 Å. This repulsive interaction is not surprising for such small distances between Ca atoms, as it can be rationalized from the fact that the equilibrium length of gas-phase Ca_2 is 4.00 Å. At intermediate distances of 4.26 and 4.92 Å the interaction between adatoms is attractive, thus revealing the tendency of Ca atoms for

clusterization. Yet, the interaction energy of 0.88 eV/dimer of the most stable Ca_2 configuration is much smaller than the corresponding value of 1.85 eV/dimer found for the most stable adsorption configuration of Ti_2. Furthermore, Ca dimer length is 3.65 Å, much larger than 2.43 Å of the Ti dimer. The differences in the structural properties of Ca and Ti dimers already indicate possible 2D growth of Ca, though for the unambiguous conclusion on the growth morphology bigger clusters must be examined.

Table 4.3: Binding energies (E_B), adhesion energies (E_{ad}), average intra-cluster bond lengths of Ca dimers, trimers and tetramers on graphene and the largest out-of-plane displacements of C atoms (Δz) when a particular metal cluster is adsorbed. The corresponding adsorption geometries are presented in Fig. 4.7. Note that the energies are expressed per metal atom.

Cluster type	Adsorption geometry	E_B (eV/atom)	E_{ad} (eV/atom)	M-M bond length (Å)	Δz (Å)
Ca_2	Fig. 4.7a	0.99	0.88	3.65	0.08
Ca_2	Fig. 4.7b	0.61	0.50	3.79	0.02
Ca_3	Fig. 4.7c	1.04	0.66	3.83	0.13
Ca_3	Fig. 4.7d	0.88	0.50	3.82	0.03
Ca_4	Fig. 4.7e	1.14	0.77	3.87	0.14
Ca_4	Fig. 4.7f	1.05	0.41	3.81	0.06

The study of Ca trimers (Fig. 4.7c-d) shows that a trimer parallel to graphene plane is 0.48 eV more stable than the same trimer adsorbed perpendicularly to plane, with only two atoms on the surface. Furthermore, maximal out-of-plane displacement of C atoms for horizontally adsorbed trimer is considerably larger than the corresponding displacement for vertically adsorbed trimer (Table 4.3), indicating much stronger interaction with graphene when Ca_3 is adsorbed as depicted in Fig. 4.7c.

The preference for 2D growth is strongly supported by the study on the Ca tetramer. After the calculations on gas-phase tetramers, we found the planar geometry of Ca_4 to be metastable as the tetrahedral one is 1.08 eV lower in energy. This energy difference between planar and tetrahedral Ca_4 is even larger than the energy difference of the corresponding Ti tetramers in the gas-phase. Yet, the adsorption on graphene is changing the energy balance of Ca tetramers drastically. The planar Ca_4 depicted in Fig. 4.7e is the most stable tetramer configuration, with the total energy as much as 0.36 eV lower than that of the Ca_4 with tetrahedral geometry depicted in Fig. 4.7f. The strength of the interaction of Ca atoms with graphene is sufficient for breaking intra cluster Ca bonds in order to gain one extra Ca atom in

direct contact with the surface.

Strong interaction of Ca with graphene, together with the Ca-Ca attraction of moderate strength give rise to the preference of Ca adsorbates to gather into 2D islands and finally to form stable 2D monolayers on graphene with uniform coverage. We will devote the remainder of the chapter to these particular structures.

4.4 Calcium 2D structures on graphene

From the inspections on small Ca clusters on graphene we concluded that the 2D growth mode of Ca on graphene is preferred. In this subsection we describe the structural and electronic properties of one-atom-thick films of Ca adsorbed on graphene sheet. In addition to this, we report the enhanced adhesion of Ca-intercalated bilayer graphene.

We calculated total energies of structures with different Ca coverages and found that the most favorable configuration is the one with the coverage of 1/6 monolayer[2] with the Ca-Ca distance of 4.26 Å. This structure is depicted in Fig. 4.8a and we refer to it as G-Ca-2D. When this structure is compared with Ca dimers adsorbed

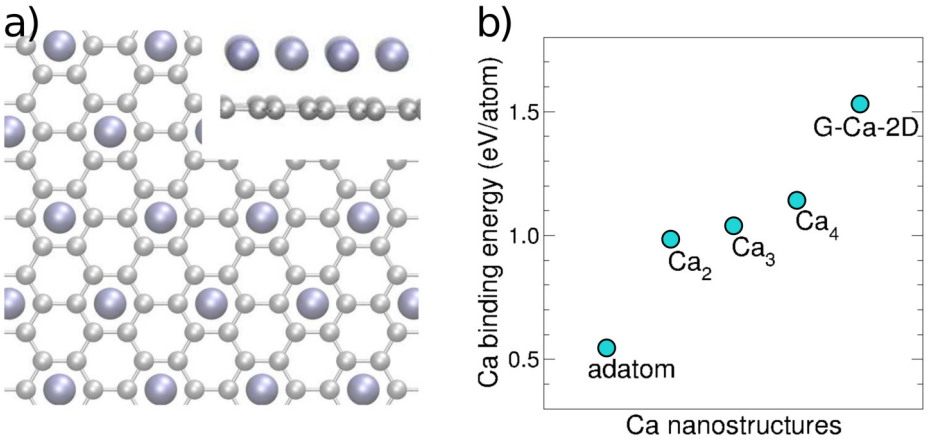

Figure 4.8: a) The most stable monolayer arrangement of Ca adatoms on graphene, marked in text as G-Ca-2D; b) Trends in Ca binding energy as a function of size of Ca nanostructures.

on graphene presented in Fig. 4.3a-d, it becomes clear that for the Ca-Ca distance of 4.26 Å the interaction energy of 0.66 eV is not far from its maximum value of 0.88 eV found for the most stable Ca dimer with the bond length of 3.64 Å (Fig. 4.7a). Though the Ca-Ca distance in G-Ca-2D structure is larger than the equilibrium value found for the most favorable Ca_2 configuration on graphene, the benefit of this

[2]That is – one Ca atom per six C atoms.

arrangement is in the great increase in the coordination number of Ca adatoms, as each of them shares as many as six nearest neighbors. This results with the binding energy of 1.53 eV/atom, which is noticeably higher than the values calculated for any of small Ca clusters (Fig. 4.8b).

To get insights into the electronic properties of G-Ca-2D structure and find further evidence of its high structural stability, we calculated the corresponding band structure along the high symmetry direction $\Gamma - K$ of BZ (Fig. 4.9a) and produced the DOS plots (Fig. 4.9b-c). Due to the electron charge transfer from Ca adsorbates the Fermi level of G-Ca-2D is shifted up on energy scale from the Dirac point by 1.5 eV (Fig. 4.9b-c) and the C-2p states in the vicinity of the Fermi level are partly hybridized with the Ca-4s states. The character of these states can be rationalized from the DOS plot projected on C and Ca atomic orbitals (Fig. 4.9c). In the energy range from -2 eV to 1 eV relative to the Fermi level, we found that the electronic states are either or pure Ca-4s character (from -2 to -1 eV) or mixture of Ca-4s and C-2p orbitals (from -1 to 1 eV). The considerable energy dispersion

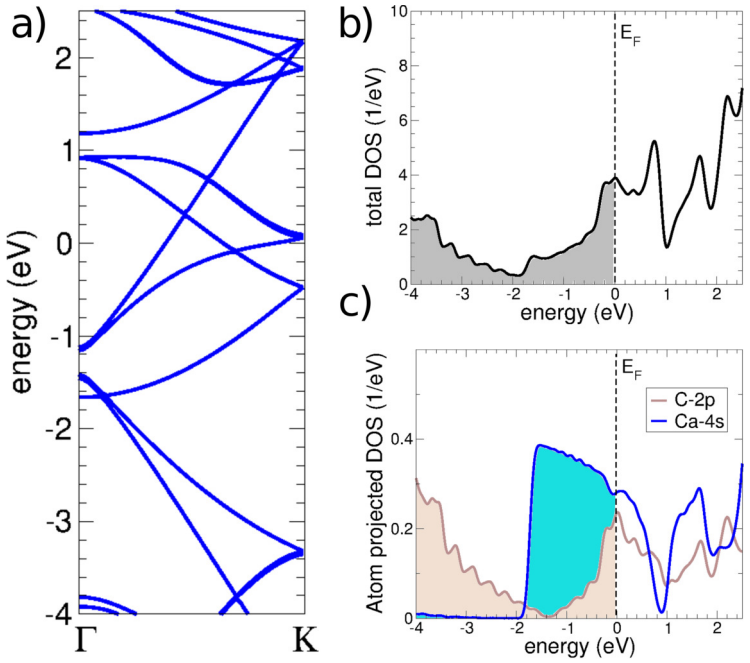

Figure 4.9: a) Band structure of G-Ca-2D structure depicted in Fig. 4.8a; b) total DOS and c) atom-projected DOS of the G-Ca-2D.

over BZ presented in Fig. 4.9a is a firm evidence of the modification of Ca atomic states due to direct overlap of Ca-4s orbitals centered at neighboring Ca adatoms, which results in the high stability of the G-Ca-2D nanostructure.

The modification of graphene electronic structure due to adsorption of uniform Ca layer and the formation of G-Ca-2D heterostructure can be exploited for various

purposes. For instance, one can achieve the ultra-strong adhesion when G-Ca-2D is brought in contact with an additional pristine graphene sheet on top of Ca layer. The corresponding sandwitched structure is depicted in Fig. 4.10a. Graphite intercalation is one of the best-known experimental procedures used for extraction of graphene layers from graphite since intercalants increase the distance between layers appreciably and are likely to weaken the inter-layer attraction.

In order to find the equilibrium inter-layer distance we calculated the adhesion energy for various distances ranging from 3.0 to 7.0 Å. It is well-known that the London dispersive forces play a decisive role in the inter-layer interaction of heterostructures of 2D materials. Thus, we included London dispersive forces in our calculations by applying optB88-vdW functional [145] and found that the Ca-intercalation of bilayer graphene truly increases the distance between the graphene planes from 3.55 to 4.65 Å. Nonetheless, intercalation with Ca also increases the adhesion energy nearly three times from 0.26 J/m^2 of pristine graphene bilayer to 0.74 J/m^2. This adhesion energy is larger than the values obtained for typical micromechanical structures and is comparable to the ultra-strong adhesion of graphene sheet on a silicon oxide substrate [146].

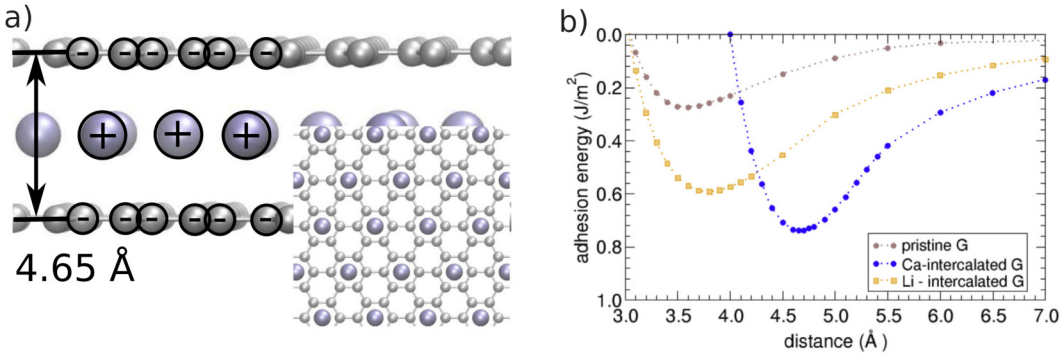

Figure 4.10: a) Ca-intercalated graphene bilayer with the same Ca coverage as in G-Ca-2D structure; b) adhesion energy as a function of distance between graphene layers calculated for pristine, Ca- and Li-intercalated graphene bilayers are presented with brown, blue and yellow dots, respectively. The calculations are performed applying optB88-vdW functional [145].

The origin of the vast increase in the adhesion energy is the attractive electrostatic interaction between the graphene plane and the Ca layer. We performed Bader analysis on the structure shown in Fig. 4.10a and reveal a charge transfer of 1.05 electrons per Ca atom to graphene planes. As a matter of comparison, an individual Ca atom adsorbed on graphene monolayer showed much lower charge transfer of 0.89 electrons (see Table 4.1). Further proof that the enhanced adhesion has an electrostatic origin can be found if the adhesion energy is calculated without the

inclusion of dispersive forces. Thus, we performed the calculations with GGA-PBE functional and found the adhesion energy of 0.37 J/m^2 when the bilayer graphene is intercalated with Ca atoms. As the GGA-PBE value of the adhesion energy of pristine bilayer graphene is negligible, we conclude that the gain of 0.37 J/m^2 is solely due to electrostatic interaction. Therefore, the positively charged Ca layer is a mediator of the electrostatic attraction between negatively charged graphene planes (Fig. 4.10a).

Motivated by the importance in the technology of *lithium-ion batteries* (LIBs) where graphite is used as main anode material, we calculated the adhesion energy of the Li-intercalated bilayer graphene. Considering adsorption structures with coverage Θ of 1/18 ML and 1/32 ML and applying optB88-vdW functional, we calculated adhesion energies of 0.58 and 0.41 J/m^2, respectively. The results for $\Theta = 1/18$ ML are compared to those found for Ca-intercalated graphene with the coverage of $\Theta = 1/6$ ML. Our study revealed that the adhesion energy of Li-intercalated bilayer graphene increases with an increase of coverage. Note that due to electrostatic repulsion between Li adatoms both monolayer and bilayer graphene which contain high concentration of Li are unstable. Therefore, thermodynamically favorable coverage when bilayer graphene is intercalated with Li depends on the competing effects of a strong repulsion between Li adatoms and their attractive interaction with graphene layers.

Chapter 5

Lithium adsorption on two-dimensional crystals

During the last decade, newly discovered 2D materials have been extensively utilized in the design of nanoelectronic devices as well as in the cutting-edge technology of energy storage. Owing to their layered structure and peculiar electronic properties, 2D materials are widely considered as main candidates in the development of novel components of lithium-ion batteries with superior functionalities. To succeed in the rational design of the improved cathode and anode materials, one needs to understand the basic physical mechanisms governing the interaction of Li with 2D materials.

This Chapter is devoted to the interaction of Li with fifteen 2D crystals, including transition metal oxides (TMOs) and dichalcogenides (TMDs), carbides of Group XIV elements, functionalized graphene, silicene and germanene as well as black phosphorus (BP) and Ti_2C MXene. Structural and electronic properties of the majority of aforementioned materials are already described in Chapter 3. Here we describe the general trend in Li binding based on the position of the lowest unoccupied electronic states of pristine 2D materials. Therefore, we distinguish two classes (or groups) of 2D materials: the first class contains the majority of them which follow a simple binding picture while the second one encompasses a few materials where the interaction with Li gives rise to substantial changes of structural and electronic properties.

5.1 Introduction

Since the isolation of single graphene layer in 2004 and the experimental demonstration of its superb electronic properties the research efforts motivated by this discovery have resulted in a whole new class of 2D materials with a variety of structural

and electronic properties. The possibilities became even larger with the appearance of van der Waals (vdW) heterostructures made of various 2D crystals stacked in a predetermined sequence [2]. Different choice of stacking sequence in vdW heterostructures can drastically alter their properties and hence the functionality of the electronic devices which are made of them.

2D materials together with their vdW heterostructures are widely considered as promising candidates for key components in diverse fields of nanotechnology, e.g. for post-silicon transistors [13, 147], next generation of solar cells [148], or *lithium-ion batteries* (LIBs) with improved charging rate and storage capacity [149, 150]. The efficiency of LIBs, today's main energy storage devices in mobile phones, notebooks as well as electrical cars, depends on the choice of materials they are build of, as they must be able to adsorb and quickly transport large quantities of lithium. These features strongly depend on (1) the strength of Li binding to these materials and (2) the mobility of Li atoms on their surface.

The prediction of the behavior of Li atoms upon their deposition on cathode or anode is based on our understanding of interaction of Li atoms with the building blocks of battery's components. Therefore, the number of scientific papers aimed to shed light on the microscopic mechanisms which are governing the interaction of Li with 2D materials is rapidly growing. Due to importance of graphene in various future technologies, Li adsorption on this 2D crystal has been thoroughly studied [133, 141, 151]. In Chapter 4 we have shown that the repulsive interaction between Li adsorbates at graphene is of electrostatic origin and is a consequence of the pronounced electronic charge transfer from Li adatoms to graphene layer. The same effect is found in DFT studies of adsorption of alkaline metals to other 2D crystals. Though the first-principles studies covered Li adsorption on MXenes [152], phosphorene [153, 154, 155], SiC [156], MoO_2 [157], MnS_2 [158], MoS_2 [159, 160] as well as graphene/MoS_2 bilayers [161], the study which will provide the details on general trends of Li adsorption on a variety of 2D crystals is still missing.

We applied DFT to reveal the structural and electronic properties of Li adsorbates at 2D materials. General trends of Li binding at diverse 2D crystals can be rationalized from their basic electronic properties, namely the energies of the lowest unoccupied electronic states. Among selected 2D materials, graphane and carbides of Group XIV elements show distinct behavior compared to other 2D crystals as the new electronic states emerge upon Li adsorption on these 2D crystals. Explanation for this specific behavior together with the classification of 2D crystals based on the structural deformation of surface and the changes in the electronic structure of 2D crystal upon Li adsorption are provided in the following sections.

5.2 Modeling of 2D crystal surfaces

The selection of 2D crystals made in this work was motivated by the necessity of having a large diversity of structures which carry out distinct electronic properties needed for unambiguous conclusions on general binding trends. Thus, our study includes transition metal dichalcogenides (MoS_2, $MoSe_2$, CrS_2 and $CrSe_2$), transition metal oxides (MoO_2 and CrO_2), MXene (Ti_2C monolayer), Group XIV carbide monolayers (SiC, GeC, SnC), hydrogenated silicene (Si-H), germanene (Ge-H) and graphene (Gra-H), fluorinated graphene (Gra-F) as well as black phosphorus monolayer – phosphorene (BP).

2D crystals were modeled with a supercell with periodic boundary conditions within the layer and the open boundary conditions in the direction perpendicular to layer with at least 8 Å of vacuum on each side of the surface. The imposed periodic boundary conditions affect Li *binding energy* (E_B), as Li atoms from the neighboring cells interact with each other. Consequently, for the correct values of E_B the supercell must be sufficiently large. We performed test calculations for Li atom adsorbed on SnC and CrO_2 for various supercell sizes ranging from 3×3 to 6×6 (Table 5.1) and concluded that the best choice is a 4×4 surface unit cell, as it provides well-converged binding energies with a modest computational cost. Therefore, 2D

Table 5.1: Binding energy of Li adatom on SnC and CrO_2, calculated for rombohedral surface unit cells of different size.

2D crystal cell size	SnC	CrO_2
	(eV)	
3×3	1.87	4.06
4×4	1.88	4.22
5×5	1.90	4.26
6×6	1.91	4.28

crystals were modeled with a 4×4 rhombohedral cell containing 16 atoms per atomic layer (transition metal oxides and dichalcogenides) or 16 atoms per sublattice of honeycomb structure (carbides of Group XIV elements, fluorinated graphene as well as graphane, silicane and germanane). Phosphorene was modeled with a rectangular unit cell with 36 phosphorus atoms. For all investigated surfaces we carried out the calculations with theoretically optimized lattice constants (Table 5.2). The sampling of Brillouin zone was done according to the Monkhorst-Pack scheme [47] with 16 k-points.

Majority the structures listed in Table 5.2 are semiconducting, except Ti_2C which shows metallic behavior. One of the guidelines for this particular choice of 2D

structures was the position of their lowest unoccupied states relative to the value of the electrostatic potential far from the surface. We will refer to it as *the electrostatic vacuum*. For the sake of shortness, as fourteen of fifteen listed 2D crystals are semiconducting we shall refer to the lowest unoccupied states as *the conduction band minima* (CBM).[1]

Table 5.2: Structural and electronic properties of pristine 2D crystals selected in this work: lattice constants, position of the conduction band minimum (CBM) and midgap states calculated with respect to the electrostatic vacuum. Also, binding energies (E_B) of Li atom on 2D crystals with the corresponding distance from the nearest atom from the surface d(Li-X). Energies are in eV and distances are in Å.

	2D crystal	Lattice constant	CBM	Midgap state	d(Li-X), X	Li binding energy (E_B)
1	Graphane (Gra-H)	2.52	−1.30	−2.87	2.45, H	0.01
2	SiC	3.10	−2.51	−3.91	2.32, Si	1.00
3	GeC	3.26	−2.75	−4.21	2.31, C	1.43
4	Silicane (Si-H)	3.86	−2.87	–	2.07, H	0.64
5	SnC	3.59	−3.56	−4.19	2.32, C	1.88
6	Germanane (Ge-H)	4.04	−3.71	–	2.11, H	0.93
7	$MoSe_2$	3.32	−3.89	–	2.49, Se	1.43
8	Phosphorene (BP)	4.42, 3.43	−4.17	–	2.46, P	1.98
9	MoS_2	3.18	−4.25	–	2.38, S	1.79
10	Fluoronated graphene (Gra-F)	2.62	−4.48	–	1.88, F	1.78
11	Ti_2C	3.04	−4.52	–	3.07, Ti	2.31
12	$CrSe_2$	3.22	−4.57	–	2.49, Se	2.06
13	CrS_2	3.05	−4.98	–	2.38, S	2.45
14	MoO_2	2.83	−5.79	–	2.01, O	2.99
15	CrO_2	2.65	−6.99	–	2.00, O	4.23

In our study, for every 2D crystal we firstly checked if Li binds to its surface, i.e. if E_B is positive, and made a choice of 2D crystals with the intention to cover the large interval of CBM on energy scale. For example, *h*-BN has the CBM of −1.16 eV which is the highest value of all considered 2D crystals (see Table 5.2), but we found no binding of Li to its surface. Thus, we excluded *h*-BN from further considerations.

[1]But, bearing in mind that the notion of CBM does not apply for metals, as the lowest unoccupied states in metals lye just above the Fermi level.

5.3 Li adatoms on 2D crystals

We begin our investigation of Li adsorption at 2D crystals with an individual Li atom adsorbed at different sites of selected 2D crystal. Only the most stable adsorption geometries, i.e. sites with the highest E_B value, are further considered. DFT calculations reveal that Li adsorption geometries of 15 selected 2D crystals

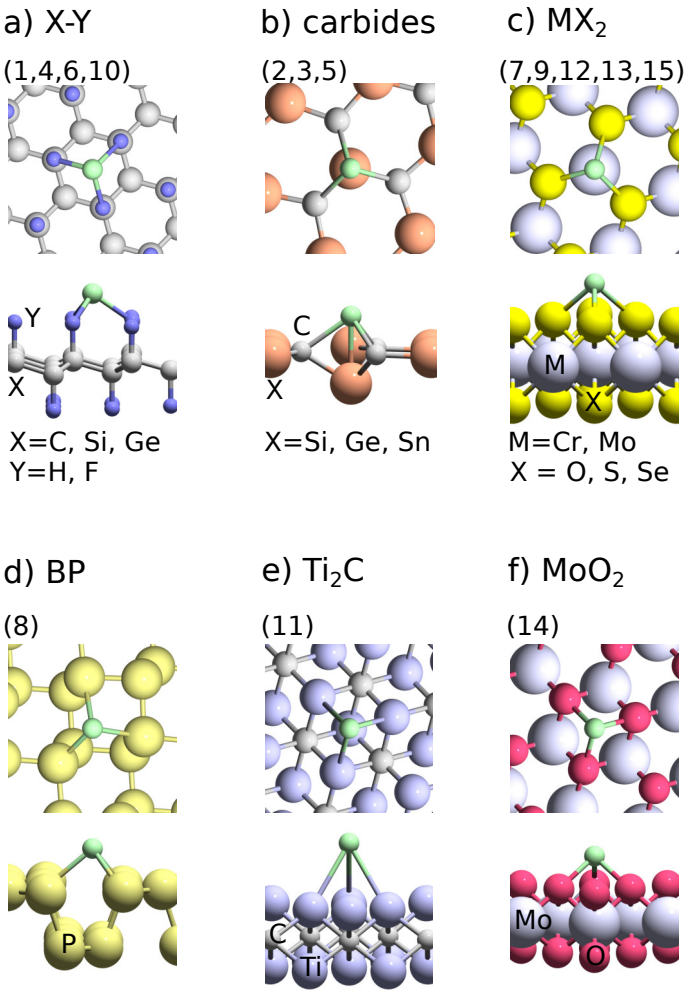

Figure 5.1: Top and side view of the most stable adsorption geometries of Li atom (green sphere) on 2D crystals. Materials are classified into groups according to their structural similarity: a) graphane, silicane, germanane and fluoronated graphene; b) carbides of Group XIV elements – SiC, GeC and SnC; c) MX_2 structures – TMOs and TMDs ; d) phosphorene; e) Ti_2C; f) MoO_2. MoO_2 is depicted separately as Li adsorption geometry on this 2D crystal is different from all the rest of the MX_2 group. The numbers in the upper left corner of images correspond to the enumeration of 2D structures in Table 5.2 and in Fig. 5.2.

can be classified into six different groups as depicted in Fig. 5.1.

The most favorable adsorption sites of Li atom at hydrogenated monolayers of C,

Si and Ge, known as graphane, silicane and germanane as well as at fully fluorinated graphene is depicted in Fig. 5.1a. At each of these surfaces Li binds in the hollow site between three H or F atoms. The second group of adsorption geometries, depicted in Fig. 5.1b, encompasses carbides of Group XIV elements – namely SiC, GeC and SnC. They have in common that Li atom binds atop of metal atom which becomes largely displaced from the surface plane. The third group of 2D crystals (Fig. 5.1c) contains majority of MX_2 monolayers, where the preferred binding site is atop metal atom and between three O, S or Se atoms. The most stable adsorption sites of Li atom on BP and Ti_2C are depicted in Fig. 5.1d and Fig. 5.1e, respectively. On the contrary to other MX_2 structures shown in Fig. 5.1c, Li atom adsorbed on MoO_2 monolayer displays different behavior as it binds in the threefold hollow site between O atoms without metal atom underneath (Fig. 5.1f). The corresponding binding energies together with the distances of Li atom from its nearest neighbors are presented in Table 5.2.

When Li is adsorbed on 2D crystal, it shows strong tendency to transfer the $2s$ electron to the surface. This behavior is shared by all alkaline adsorbates due to their low electronegativity. At semiconducting or insulating surfaces the electron is transferred from the atomic Li-$2s$ state to the states near the CBM, which are the lowest unoccupied states in the system. Thus, it is likely to expect a correlation between the energy gain due to charge transfer from Li adatom to the surface and the position of the CBM. Moreover, this energy gain of the system can be identified as Li binding energy, E_{B}.

Following these arguments, we plotted E_{B} as a function of CBM for fifteen 2D crystals considered in this work, as shown in Fig. 5.2. The plot indeed demonstrates a strong correlation between Li binding energy and the position of CBM of pristine 2D crystals. The highest E_{B} of 4.23 eV was calculated for Li adatom at CrO_2 and is accompanied with the lowest energy of the CBM among studied 2D crystals of nearly -7 eV below the vacuum level.[2] On the other hand, graphane has the highest CBM position of -1.30 eV below vacuum and the lowest Li binding energy of only 0.01 eV. For other 2D crystals the values of E_{B} and CBM are between these two limits (Table 5.2). The only metal among studied materials is Ti_2C, thus instead of the CBM position the Fermi level of Ti_2C is plotted in Fig. 5.1 as it represents the bottom of the lowest unoccupied states of the metallic system.

From the plot in Fig. 5.2 one can clearly differentiate between two groups of materials showing distinct Li adsorption behavior:

[2]When expressing CBM position the zero of the energy scale is set to the electrostatic potential at the cell boundary in the z-direction, i.e. electrostatic vacuum.

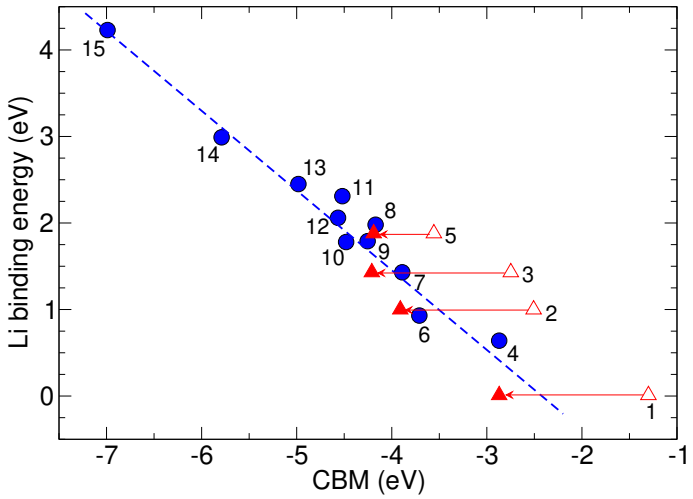

Figure 5.2: Correlation between Li atom binding energy (E_B) and conduction band minimum (CBM) for selected 2D crystals; surfaces without and with midgap state are marked with blue circles and red triangles, respectively. Open triangles indicate the CBM positions of pristine 2D crystals, while the filled triangles correspond to the midgap states, which are the lowest unoccupied states of deformed 2D crystals. Horizontal arrows between the open and filled triangles indicate energy shifts from CBM of pristine 2D crystal to its midgap state induced upon Li adsorption. The numbering of materials is the same as in Table 5.2. The dashed blue line serves as a guide to eyes.

1. the materials which closely follow the correlation graph of Li binding energy and the CBM position. Majority of the studied 2D materials belong to this group. They are represented with blue circles in Fig. 5.2. For the sake of brevity, we will refer to them as the materials from *the blue group*;

2. the materials whose dependence of Li binding energy on CBM position is shifted from the correlation graph. They are represented with red triangles in Fig. 5.2. This group of materials will be referred to as *the red group*.

To substantiate the differences in structural and electronic properties of Li adsorbates on the two groups of materials, we further inspect the Li adsorption on the groups' representatives – CrO_2 from the blue group and SnC from the red group. This particular choice is made based on the CBM position of materials, as CrO_2 and SnC show the strongest Li binding among all 2D materials from their respective groups. Thus, we expect the most pronounced changes in their structural and electronic properties upon Li adsorption.

The adsorption geometry of Li atom on CrO_2 monolayer is shown in Fig 5.1c. As Li atom is adsorbed, the positions of Cr and O atoms are slightly changed as the largest displacement does not exceed 0.06 Å. The effect of Li adsorption on

the electronic structure of CrO_2 can be rationalized from the DOS plots shown in Fig. 5.3. Total DOS of a pristine CrO_2 is also plotted in Fig. 5.3a for comparison. Figure 5.3a clearly demonstrates that Li adatom donates its only valence $2s$ electron to the conduction band of CrO_2 and shifts the Fermi level of a pristine monolayer by 0.44 eV. Apart from the change in the occupation, CrO_2 electronic states near E_F are barely affected by Li adsorbate. This observation is confirmed by the plot of DOS projected on relevant atomic orbitals, that is $3d$ orbitals of Cr, $2p$ orbitals of O and $2s$ orbitals of Li (Fig. 5.3b). Most of the Li-$2s$ states are located within the

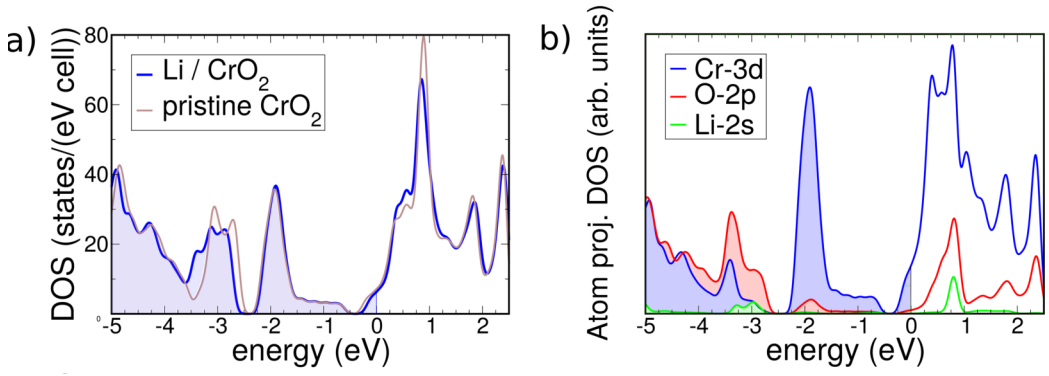

Figure 5.3: a) Total DOS of pristine CrO_2 monolayer and the monolayer with adsorbed Li atom; b) DOS of the CrO_2 monolayer with adsorbed Li atom, projected on $3d$ orbitals of Cr (blue), $2p$ orbitals of O (red) and $2s$ orbitals of Li (green).

peak which lies 0.8 eV above E_F (Fig. 5.3b), and the contribution of Li-$2s$ states to the total DOS near E_F is negligible. The states near the top of the valence band and the bottom of the conduction band are predominately of Cr-$3d$ character with the small contribution from O-$2p$ orbitals. Thus, upon adsorption of an Li atom on CrO_2, $2s$ electron is transferred to the $3d$ orbitals of Cr atoms and delocalized across surface as shown in plot of the accumulated electron charge density (Fig. 5.4a).

For the sake of completeness, we show the plots of the total DOS of pristine BP and graphane monolayers as well as DOS of these surfaces with added Li atom (Fig. 5.5). Though the structure of these 2D crystals are different compared to MX_2 materials, the Li adsorption behavior is the same, as the only effect of Li adsorbate on the electronic structure of BP and graphane is in the filling of the lowest unoccupied states.

Compared to majority of 2D crystals belonging to the blue group, graphane and carbides of Group XIV elements, i.e. 2D crystals from the red group display completely different Li binding picture. Though the general trend in Li binding to 2D crystals from the red group is still observable as the binding energy increases when the CBM position is deeper on energy scale, the points in Fig. 5.2 which

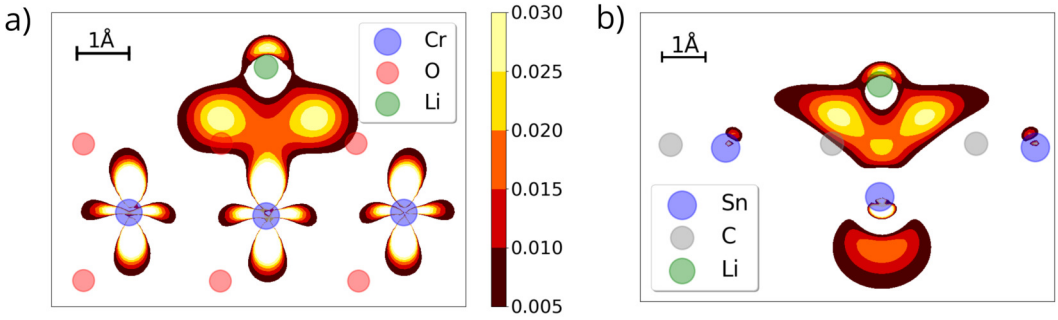

Figure 5.4: Electron density induced upon Li adsorption at (a) CrO_2 and (b) SnC monolayer. Only isocontours corresponding to charge accumulation are plotted. Thermographic scale (in e/Å^3) in the middle of the figure applies to both graphs.

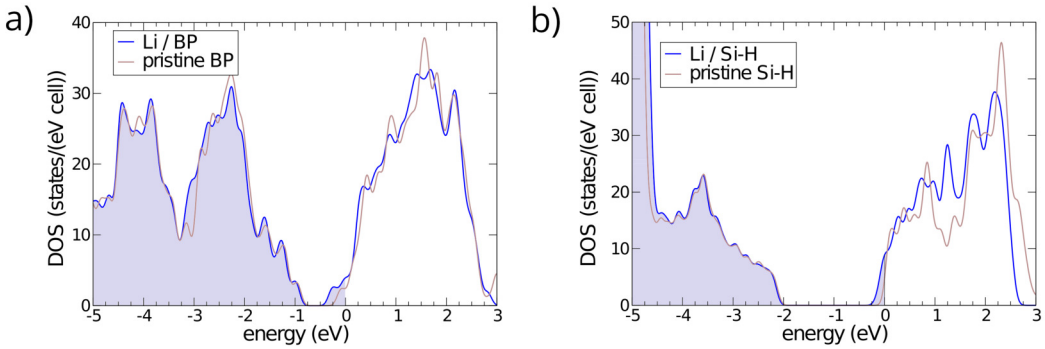

Figure 5.5: Total DOS of (a) BP and (b) silicane monolayer with and without Li adatom. Total DOS of pristine 2D crystals are shifted on energy scale to match the total DOS of Li atom adsorbed on the 2D crystals. Zero of the energy scale is set to the Fermi level of Li atom adsorbed on 2D crystal.

correspond to graphane, SiC, GeC and SnC (open red triangles) show a pronounced deviation from the dashed line.

Considerable differences can be found in the structural properties of Li atom adsorbed on 2D materials belonging to distinct groups. In a sharp contrast to the materials from the blue group where the adsorption of Li atom only slightly changes the positions of the surface atoms, the Li adsorption induces large deformations in the surfaces of SiC, GeC and SnC (see Fig. 5.1b). After Li atom is adsorbed at the position above the Si, Ge and Sn atoms of SiC, GeC and SnC, the host atoms are moved downwards as much as 0.75, 0.90 and 1.13 Å, respectively. The increase in the deformation in the sequence SiC−GeC−SnC is accompanied with the increase in Li binding energy, as the corresponding E_B values are 1.00, 1.43 and 1.88 eV (Table 5.2). On the other hand, the binding of Li on graphane is very weak as the E_B is only 0.01 eV (Table 5.2) and the presence of Li atom in the system does not

alter the positions of the surface atoms. Thus, for materials from the red group, the deformation of surface upon Li adsorption is well correlated to the strength of Li binding. This correlation is not documented for any of the 2D materials from the blue group, as the surface deformation after Li adsorption is modest even for CrO_2 which has the highest E_B value of all considered materials.

Closer inspection reveals that after the adsorption of Li atom *midgap states* appear on each of the four surfaces from the red group. To shed light on the origin of midgap states we compared the total DOS of ideal SnC monolayer to that of deformed SnC monolayer in Fig. 5.6a. The positions of Sn and C atoms in deformed

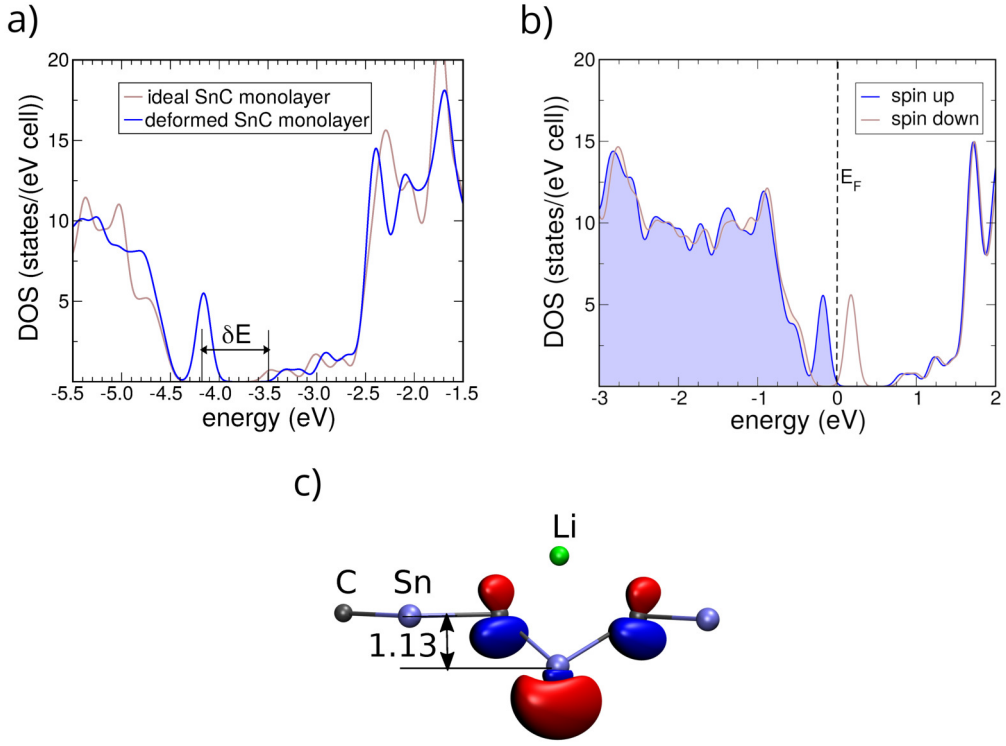

Figure 5.6: a) Total DOS of pristine SnC monolayer calculated for the ideal sheet (brown curve) and deformed monolayer (blue line) where Sn and C atoms are fixed at the positions as in SnC with Li adatom. δE indicates the position of the midgap state relative to the CBM of ideal SnC monolayer; b) Total DOS obtained from spin-polarized calculations of SnC monolayer with adsorbed Li atom on top of Sn atom; c) Isosurface plot of Kohn-Sham orbital of the midgap state at Γ point. Two-color scheme corresponds to the regions with different sign of wavefunction. The number on the left indicates the displacement of Sn atom (in Å) from the SnC plane, induced by Li adsorbate.

SnC monolayer are the same as that of the SnC monolayer with Li adatom. From Fig. 5.6a we conclude that the emergence of midgap states is triggered by the large displacement of the atom which lies below Li adatom.

As the midgap state lies above the valence band maximum and below the conduction band minimum, it plays the role of the lowest unoccupied state in the system. Thus, after the Li atom is adsorbed on the surfaces of graphane, SiC, GeC and SnC, Li-2s electron is transferred to the midgap states instead of the CBM. Moreover, spin-polarized DFT calculations reveal that the total magnetic moment of $1\mu_B$ is induced upon the adsorption of Li atom on each of these four surfaces. Total DOS of SnC monolayer with Li adatom calculated for separate spin channels in Fig. 5.6b confirms that only spin-up midgap state is filled. High degree of localization of the midgap state in SnC favors the spin polarization of the system.

Comparison of the charge density induced upon Li adsorption on the blue group representative CrO_2 (Fig. 5.4a) to that of SnC (Fig. 5.4b) which represents the red group clearly portraits the differences in redistribution of the electronic charge in these materials after the Li atom is deposited on their surfaces. When Li atom is adsorbed on SnC, Li-2s electron is transferred to the midgap state mainly localized around Li adatom and at Sn atom below, with the small contribution from the few C atoms nearby (Fig. 5.4b). This is markedly different from the corresponding plot of the charge transferred from Li to CrO_2 monolayer, where the Li-2s electron is completely spread across surface.

When Li atom is adsorbed on any of the surfaces from the red group, the midgap state becomes the highest occupied state in the system. To expose the degree of localization of this state, we plotted the isosurface of the highest occupied Kohn-Sham orbital at Γ point of Li atom adsorbed on SnC (Fig. 5.6c).[3] This plot confirms that the wavefunction that corresponds to the midgap state is of localized character, as its lobes are located at the Sn atom below the Li atom and at the nearest C atoms.

To conclude this section, we present the plots of the total DOS of Li atom adsorbed on SiC and GeC monolayers (Fig. 5.7). Comparison of these plots to the plot in Fig. 5.6b of the Li atom adsorbed on SnC confirms that the appearance of the midgap state is characteristic for all the materials from the red group. Interestingly, trend in the change of the position of midgap state can be observed in the sequence SiC−GeC−SnC as it is moving from the CBM closer to the VBM, while the splitting between the spin-up and spin-down midgap states is becoming less pronounced.

5.4 High Li coverage on 2D crystals

Rapid development of various customer electronic devices generated the urgent need for further improvements in energy storage. Among all characteristics of LIBs of

[3] Γ point in BZ is at $k = 0$. Hence, the Kohn-Sham orbital is a real function.

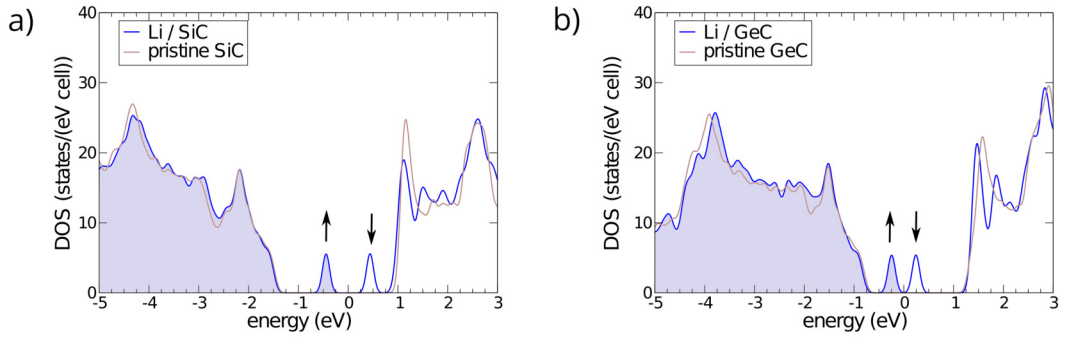

Figure 5.7: Total DOS of (a) SiC and (b) GeC monolayer with and without Li adatom. Total DOS of pristine 2D crystals are shifted on energy scale to match the total DOS of Li atom adsorbed on the 2D crystals. Zero of the energy scale is set to the Fermi level of Li atom adsorbed on 2D crystal. Vertical arrows indicate the spin polarization of the midgap states.

particular importance is their storage capacity, the property correlated to the quantity of lithium contained inside the battery. Thus, for technological application of 2D materials in cathode or anode electrodes they must be able to accommodate densely packed Li adsorbates without serious material expansion.

So far we studied the properties of 2D crystals with low coverages of Li adsorbed on their surface. Based on the nature of interaction of 2D crystal with an individual Li atom, in Section 5.3 we classified 2D crystals into two groups carrying out qualitatively different interaction with Li adsorbates. Here we examine the ability of Li to form densely packed structures at (1) SnC monolayer, representative of the group of materials where the interaction of Li adatoms with the surfaces is well localized, and (2) CrO_2 monolayer, representative of the group of materials with fairly delocalized charge transfer from Li adatoms.

5.4.1 High coverage Li structures on SnC

We start the investigation of high Li coverage structures at 2D materials with the study of interaction between two Li adatoms, adsorbed closely to each other. Based on the interaction between metal atoms in their dimer configuration, one can draw conclusions on the preference of metal atoms to form ordered densely packed structures at 2D materials. Similar study has been conducted in Section 4.3 for various dimer configurations of Li, Ca and Ti adsorbed on graphene.

DFT study of various Li_2 adsorption geometries on SnC revealed the structure depicted in Fig. 5.8a as the most stable one. The binding energy of 2.06 eV per atom is larger than 1.88 eV found for an individual Li on the same surface.[4] The

[4]The same rhombohedral 4×4 surface unit cells has been used for both calculations.

increase of 0.18 eV in E_B indicates that the interaction between two Li atoms in their dimer configuration is attractive. This is completely opposite to the long-range repulsion between Li adatoms on graphene thoroughly examined in Subsection 4.3.1. The stability of Li dimers adsorbed on SnC originates from the midgap state which can accommodate two electrons. DOS of an individual Li atom adsorbed on SnC presented in Fig. 5.6b clearly demonstrates that the midgap state is half-filled, as its spin-down component is completely empty.

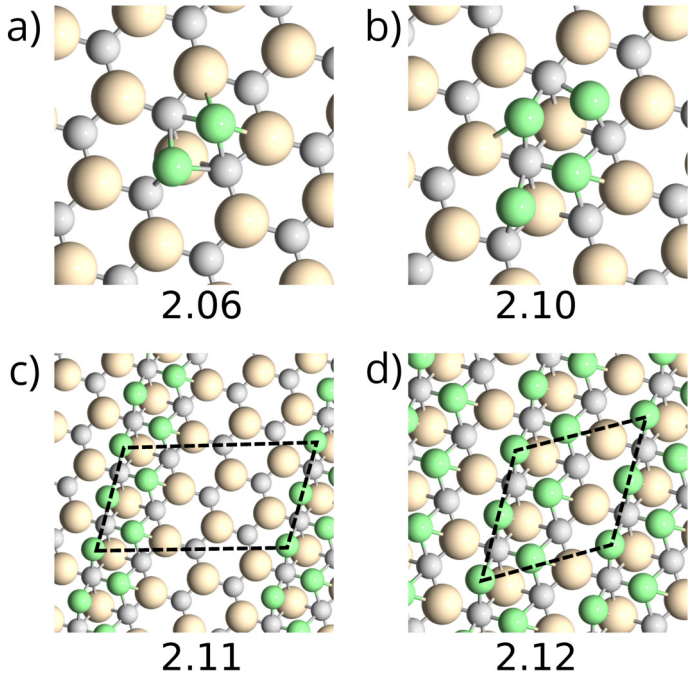

Figure 5.8: The most stable adsorption geometry of (a) Li dimer, (b) Li tetramer and the most stable ordered structures on SnC monolayer at Li coverages of (c) $\Theta = 1/2$ ML and (d) $\Theta = 1$ ML. A full monolayer (1 ML) represents the coverage where the number of Li atoms equals that of Sn atoms. Sn, C, and Li atoms are represented by large yellow, small gray, and green spheres, respectively. The numbers bellow images indicate Li binding energy in eV per atom. Surface unit cells of ordered structures are marked with dashed black lines.

When two Li adatoms are adsorbed above the same Sn atom, two Li-2s electrons are transferred to the surface giving rise to the completely filled midgap state. This is confirmed with the plot of total DOS presented in Fig. 5.9a. DOS projected on 2p orbitals of C atoms and on 5p orbitals of Sn atoms presented in Fig. 5.9b reveals that the midgap state is of predominately Sn-5p character. The preference of dimer adsorption configuration in comparison to the configuration where two individual Li atoms are adsorbed at different sites can be explained with the simple argument: when both Li atoms are adsorbed at the same site, the energy penalty for structure deformation is shared by two adatoms.

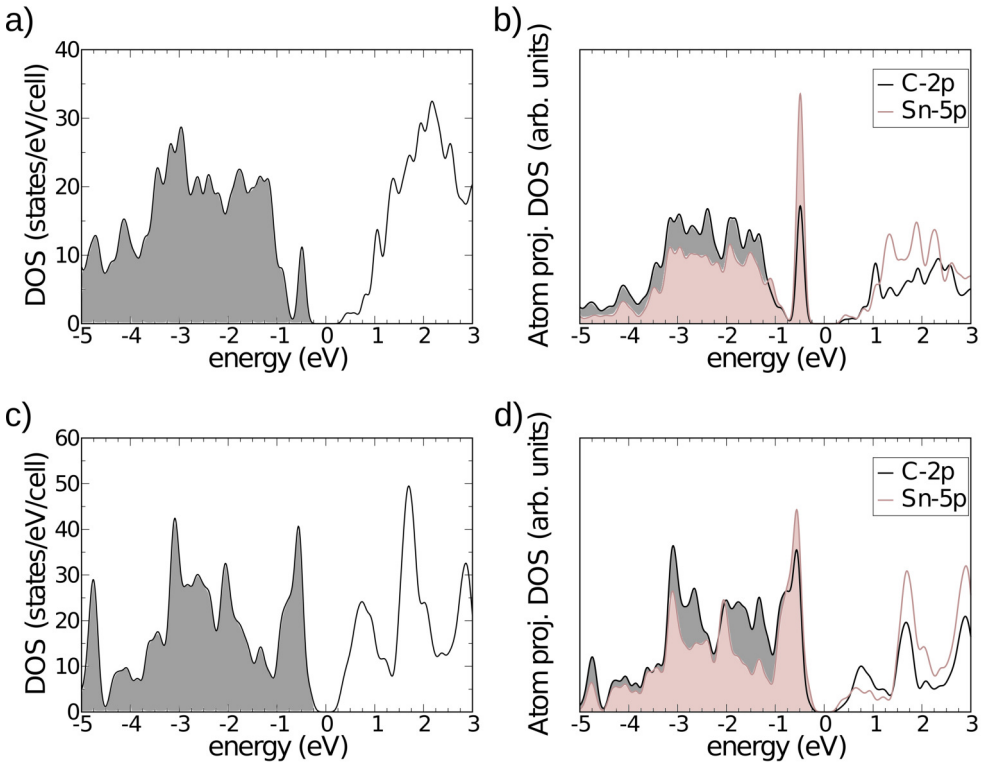

Figure 5.9: Total and atom-projected DOS of (a), (b) Li_2 dimer and (c), (d) Li monolayer on SnC.

Structures presented in Fig. 5.8b-d have similar binding energies, with the reported values close to that of an individual Li dimer. Small increase in E_B found in tetramer (Fig. 5.8b) and structures with high Li coverage of 1/2 ML (Fig. 5.8c) and 1 ML (Fig. 5.8d) is the firm evidence of their stability. Thus, instead of the highly ordered structures where Li atoms are uniformly spread across SnC surface the favorable adsorption geometries are the ones where Li atoms form chains of dimers as depicted in Figs. 5.8c and 5.8d. In all of these adsorption structures from Fig. 5.8 the number of Li atoms is twice the number of created midgap states.

With the increase of Li coverage the midgap states start to overlap. The broadening of the peak in DOS presented in Fig. 5.9c is due to hybridization of the midgap states located on neighboring Sn atoms. Even for the highest Li coverage, the system stays in its semiconducting state but with the substantial decrease in bandgap size due to merging of the midgap states with the states from the valence band (Fig. 5.9c).

High density of Li on 2D materials can cause substantial changes in their structure, e.g. in their lattice constant or the layer corrugation. The expansion of materials upon Li adsorption used in cathode and anode electrodes presents a major issue in the construction of LIBs. Thus, we examined the volume expansion effect

in lithiated 2D materials with Li coverage of 1/2 and 1 ML. DFT calculations reveal that the lattice constant decreases 1% in fully lithiated SnC (coverage of 1 ML) compared to the pristine sheet. However, Li adsorption causes large corrugation of the SnC layer, as the Sn atom is pushed down upon Li atom adsorption by as much as 1.13 Å (Fig. 5.6c). Thus, the average metal-metal distance in structure with Li coverage of 1 ML is 2% larger compared to the value found for pristine SnC sheet. These calculations indicate modest changes in the lattice constants of lithiated SnC, which should not significantly deteriorate its structural stability.

5.4.2 High coverage Li structures on CrO_2

In this subsection we examine the preference of Li to form clusters on CrO_2 and exploit the ability of this 2D crystal to accommodate Li structures with high coverages.

The most favorable Li dimer structure adsorbed on CrO_2 monolayer is depicted in Fig. 5.10a. We relaxed the structure where the Li atoms are placed above the

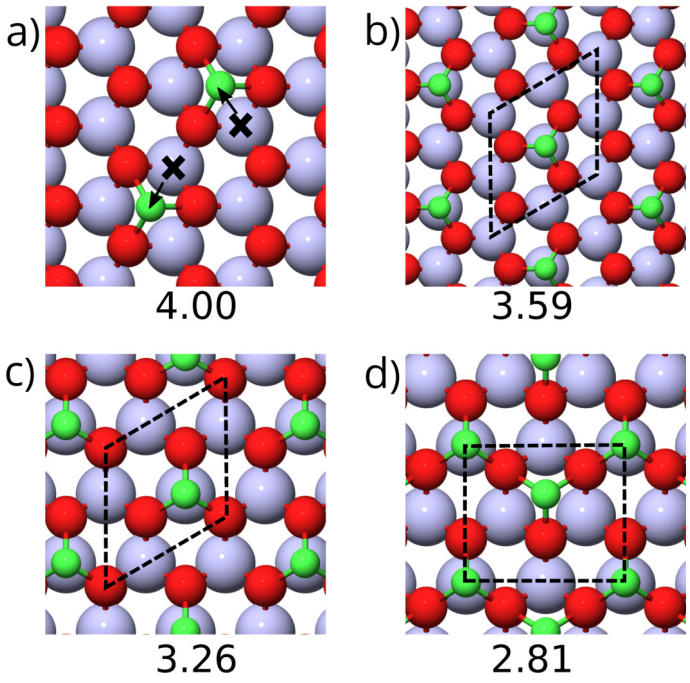

Figure 5.10: Atomic structure of a) Li dimer and the most stable ordered structures at CrO_2 monolayer at Li coverage b) Θ=1/4 ML c) Θ=1/3 ML and d) Θ=1/2 ML. Crosses in a) indicate the initial position of Li atoms prior to structural optimization. The numbers indicate Li binding energy in eV per atom; Cr, O and Li atoms are represented by light blue, red and green spheres, respectively. A full monolayer (ML) refers to the coverage where the number of Li and Cr atoms are equal. Surface unit cells are marked with black dashed lines.

adjacent Cr atoms as indicated by black crosses in Fig. 5.10a. Yet, this structure

is not stable as the Li atoms move further away from each other in the directions indicated with black arrows. As the Li adsorption on CrO_2 is not accompanied with the emergence of midgap states, strong Li-Li repulsion is not suppressed on this surface. The Li binding energy of 4.00 eV per atom is 0.23 eV smaller compared to that of the individual Li atom at the same surface. Thus, Li adatoms on CrO_2 do not show tendency towards clustering. Similar behavior is already discussed in Section 4.3.1 for Li adatoms on graphene, another 2D crystal where the Li binding is dominated by charge transfer from the adsorbed atoms to the surface.

The ordered Li structures on CrO_2 monolayer, as well as the corresponding binding energies for coverages Θ of 1/4, 1/3 and 1/2 ML are given in Fig. 5.10b-d, respectively. In a sharp contrast to SnC where the binding energy is nearly independent on Li coverage, we found the monotonic decrease of E_B with an increase in Li coverage Θ, reaching the value of 2.81 eV per atom at $\Theta = 0.5$ ML. This is as much as ~ 1.5 eV less than the binding energy of a single Li atom on the same surface. An increase of Li coverage at CrO_2 gives rise to the unfavorable accumulation of electrons in the conduction band of CrO_2 monolayer, and thus weakens lithium binding. This is completely opposite to the adsorption of Li on SnC. Thus, we expect that the CrO_2 is unsuitable substrate for the formation of densely packed Li structures.

5.4.3 Work function dependence on Li coverage

Throughout the Chapter, we examined the Li adsorption on 2D materials and provide the description of this phenomenon based on the electron charge transfer from Li to the surface. To conclude this discussion, we investigate the energy cost of electron removal from the lithiated surfaces of SnC and CrO_2, the feature which is quantified by the work function of the system.

To study the evolution of the work function with Li coverage we assumed the adsorption geometries as depicted in Figs. 5.1b and 5.1c and increased the unit cell size to simulate the decrease of Li coverage. Therefore, the unit cells with sizes in the range from 2×2 (1/4 ML) to 4×4 (1/16 ML) were used.

The results presented in Table 5.3 show that at both surfaces the workfunction decrease with an increase in Li coverage, but the degree of decrease is different. The work function of CrO_2 decreases from 7.33 eV to only 1.40 eV when Li layer with coverage of 1/4 ML is adsorbed on the pristine sheet. The corresponding change of work function of SnC is less drastic, as it decreases from 4.54 to 3.18 eV. As the Li coverage increases, the Fermi level of 2D crystal shifts closer to vacuum level which partially contributes to the decrease of work function. However, only a half

Table 5.3: Evolution of SnC and CrO_2 monolayer work functions with Li coverage. For both surfaces the calculations were performed using rhombohedral unit cells of different sizes. All energies are in eV.

Coverage (ML)	SnC	CrO_2
0	4.54	7.33
1/16	4.07	5.28
1/9	3.84	4.11
1/4	3.18	1.40

of the decrease of the CrO_2 work function is due to the change of the position of Fermi level as this shift is around 3 eV. Upon adsorption of Li on CrO_2 the electrons transferred from Li are uniformly spread across surface. Thus, the dipole layer of positively charged Li ions and negatively charged surface generates strong electric field which considerably reduces the work function. The strength of the field rapidly increases with the Li coverage. The effect on SnC sheet is less pronounced due to different Li adsorption geometry and localized character of the charge transfer.

Chapter 6

Adsorbate-induced structural phase transition in MoS_2

Since the fabrication of the first single-layer MoS_2 transistor in 2011 [13], large family of 2D materials known as *transition metal dichalcogenides* (TMDs) emerged as an important players in the development of ultrathin *field-effect transistors* (FETs). These 2D materials, which were in their bulk form extensively used for decades as lubricants, have been brought back to the spotlight of both academic and technological research for completely different applications.

In this Chapter we explore the adsorption of two different metals, namely lithium and calcium, as the viable routes for triggering the structural phase transition in MoS_2. The structural phases of MoS_2 are explained thoroughly in Section 3.5. Here we present the structural and electronic properties of Li and Ca adsorbed on two most stable phases of MoS_2 at various coverages, ranging from single adatoms to a half a monolayer. Binding pictures of Li and Ca on two phases of MoS_2 will be compared, and the simple model of Li adsorption on 2D materials explained in Chapter 5 based on the charge transfer from adsorbate to the surface will be tested also on Ca, where one can distinguish the boundaries of its validity.

6.1 Introduction

Far the most widely studied 2D crystal is graphene [1, 162], a material which displays various peculiar phenomena. Although it features ultrahigh electron mobility [163], graphene lacks a bandgap, the property which is crucial for applications in transistor nanotechnology. Various attempts of bandgap engineering turned out to be challenging due to the increase of fabrication complexity. Those endeavors led to the unfavorable deterioration of electron mobility in single-layer graphene [164, 165] or ended with the fabricated FETs based on bilayer graphene that require high

voltages to operate properly [166]. The lack of bandgap in graphene brought the spotlight to *the transition metal dichalcogenides* (TMDs), large family of 2D semiconductors which become the most widely studied channel materials in transistor nanotechnology.

Monolayer TMDs, whose structural and electronic properties are described in Chapter 3, are both fundamentally and technologically intriguing. The fact that the single-layer MoS_2 was used in the first operating 2D transistor as a channel material gained a renewed interest to the family of TMDs [13]. The bandgap of MoS_2 changes from indirect ($\sim 1.2\,\mathrm{eV}$) to direct ($\sim 1.8\,\mathrm{eV}$) as the thickness decreases from bulk to single layer [167, 123, 73]. However, apart from the change in size and the type of the bandgap with the decreasing thickness, the room-temperature mobility of charge carriers suffers a sharp decrease from bulk values of $200 - 500\,\mathrm{cm^2\,V^{-1}\,s^{-1}}$ to the values of only $0.5 - 3\,\mathrm{cm^2\,V^{-1}\,s^{-1}}$ in monolayer MoS_2 [168]. Ghatak et al. proposed that the charge traps present at the interface between the the MoS_2 layer and the SiO_2 substrate are the main reason for such degradation of mobility [169]. Often, disorder in 2D electron systems arises from extraneous sources, such as in modulation-doped III–V semiconductors where the remote dopant ions generate a random Coulomb potential which causes the localization of carriers due to weak screening at low carrier densities [170]. These are the indications that understanding the nature of the electronic states at the MoS_2/substrate interfaces as well as the charge transfer between the MoS_2 layer and the substrate or the dopant atoms/ions can be crucial for the improvement of MoS_2-based FET devices.

It is shown by Radisavljević et al. that gating MoS_2 with the high-κ dielectric HfO_2 recovers the room-temperature mobility of charge carriers back to the bulk values of $200\,\mathrm{cm^2\,V^{-1}\,s^{-1}}$, which is also comparable to that of graphene nanoribbons [13]. Further efforts in the engineering of mobility in MoS_2 focused on the so-called dual-gated FETs [171]. The additional top gate allows higher doping up to the concentrations of $n_{2D} \sim 3.6 \times 10^{13}\,\mathrm{cm^{-2}}$, which led to the observation of *metal-insulator transition* (MIT) [172], the first of its kind in a 2D semiconductor. For gate voltages corresponding to charge densities lower than $n_{2D} \sim 1 \times 10^{13}\,\mathrm{cm^{-2}}$, monolayer MoS_2 displays semiconducting behavior as the conductance decreases at lower temperatures, whereas for higher gate voltages the conductance increases as the temperature is decreased, which is the hallmark of metallic state. This particular MIT is the direct consequence of quantum interference effects of weak and strong localization corresponding to metallic and insulating state, respectively [173].

MIT can also be achieved as the consequence of the structural change in MoS_2. In Section 3.5 we explained that MoS_2 can undergo the structural phase transition

from hexagonal (2H) phase to the metastable trigonal (1T) phase (see Fig. 3.9) by various manipulations, thus giving rise to the drastic change in electronic structure from semiconducting to metallic state. The 2H $\rightarrow$ 1T structural phase transition can be achieved by mechanical deformation [8] thus exploiting the experimentally demonstrated strength of monolayer TMDs [174], by using an electron beam on the layer of 2H phase [175] or by changing the electron count as both n- and p-type doping drastically reduce the energy barrier of the transformation [77].

In practice, the p-type doping of MoS_2 can be achieved via the introduction of sulfur vacancies [176] and the n-type doping is commonly realized by intercalation with alkali metals such as lithium and sodium [177, 15, 178]. In the n-type doping scenario the electrons are transferred from adsorbate to the MoS_2 layer. Gao et al. [15] found that four electrons injected per MoS_2 unit reduce the barrier for the phase transition from 1.59 to 0.27 eV. However, this requires high coverage of Li, which can be very unfavorable due to electrostatic Li-Li repulsion and accumulation of electrons in the conduction band. Similar effects on Li binding to 2D crystal in the high-coverage regime is found for adsorption of Li on CrO_2, as explained in Subsection 5.4.2. On the other hand, adsorption of calcium can be a viable route to achive 2H $\rightarrow$ 1T phase transition as Ca atom has two valence electrons which can be donated to the substrate. Moreover, regarding Ca adsorption on graphene where we found very stable Ca-Gra-2D structure (see Section 4.4) the interaction between Ca atoms that are adsorbed on 2D crystals can be attractive at certain distances, in a sharp contrast to Li adsorbates on 2D crystals.[1]

Further, 1T phase is found to be unstable under ambient conditions as it spontaneously undergoes another phase transition due to occurrence of a *charge-density wave* (CDW). Zhuang et al. [77] reported that of all possible distorted structures derived from the 1T phase the so-called 1T$'$ structural phase (Fig. 3.9b) is the most stable one.[2] The corresponding energy difference as obtained from DFT calculations between the 1T and the 2H phase of 0.84 eV per MoS_2 unit is reduced to 0.54 eV after the emergence of 1T$'$ phase [77]. However, scanning tunneling transmission microscopy (STEM) imaging performed on chemically exfoliated MoS_2 single layers showed that all three 2H, 1T and 1T$'$ phases coexist within the single-crystalline nanosheets [118]. Similar hybrid structures are already synthesized from chemically different lattice-matched compounds such as that of graphene and h-BN [179], but the realization of in-plane heterostructures via the structural change of only one compound opens new possibilities. With the 2H $\rightarrow$ 1T phase transition the lattice

[1] Both MoS_2 and CrO_2 belong to the group of materials where the Li binding picture is dominated by the simple charge transfer from Li to the 2D crystal. See Chapter 5.

[2] For other possible structural phases see Fig. 1 of [77].

constant changes only slightly which enable mechanical stability of structures where three MoS_2 phases coexist within the same sheet. The mechanism of stabilization of 1T phase remains unclear and requires further investigation.

Motivated by previous studies of the role of adsorption of alkaline metals on the structural phase transition in TMDs [14, 15], we performed DFT calculations to reveal the structural and electronic properties of Li and Ca adsorbates on two structural phases of monolayer MoS_2. Simple picture of Li binding on 2D materials explained in Chapter 5 is valid for both phases of MoS_2 and also holds for the adsorption of Ca on the 1T′ phase at low coverages, but it breaks for Ca adsorption on 2H phase as well as for higher Ca coverages of the 1T′ phase. In this Chapter we rationalize this behavior and identify Li and Ca coverages needed to trigger the structural phase transition in MoS_2.

6.2 Modeling of the MoS_2 structural phases

We begin our discussion with the comparison of different phases of pristine MoS_2. The MoS_2 surfaces are modeled with the imposed periodic boundary conditions within the MoS_2 plane and open boundary conditions in a direction orthogonal to the plane with 10 Å of vacuum from both sides of the sheet. Calculated lattice constants of 2H and 1T phases are 3.18 Å and 3.20 Å, in good agreement with the values reported in previous studies [115, 77]. For additional computational details see Appendix C.

Zhuang et al. [77] showed that the optimizations of the same structures that starts from different geometries and sizes of the unit cell can lead to various derivations of the metastable 1T phase. Thus, one needs to perform calculations with different unit cells to find all possible distortions of 1T phase. We tested rhombohedral and rectangular unit cells and found that the usage of rhombohedral cell has a disadvantage because 1T′ phase (see Fig. 3.9), which is reported to be the most stable 1T derivation [77], cannot be obtained with rhombohedral cell due to specific geometry constraints related to the shape of the cell. Therefore, we chose a rectangular $\sqrt{3}a \times 2a$ cell with 4 Mo atoms, doubled it in both x and y directions to get the unit cell with 16 Mo atoms and performed structural optimization using BFGS algorithm [**?**]. Unit cells of both phases are depicted in Fig. 6.1. This size of the unit cell ensures at least 11 Å between the neighboring metal adatoms when an individual atom is adsorbed. Brillouin zone is sampled according to the Monkhorst-Pack scheme on a $5 \times 4 \times 1$ grid [47].

Relaxed 1T′ structure as found from our calculations is depicted in Fig. 6.1b.

Structural deformation of metastable 1T structure are followed with the dimerization of Mo atoms and formation of chains as two types of Mo−Mo bonds occur – shorter ones with the length of 2.74 Å and longer ones which are 3.69 Å long. The out-of-plane displacement of Mo atoms is modest and does not exceed 0.12 Å. On the other hand, the out-of-plane displacement of S atoms compared to positions in the 1T phase are much larger as the differences in heights of S atoms within the same S-layer are around 0.4 Å. Interestingly, the length of S−S bonds stays the same as it was in the 1T phase and equals 3.20 Å.

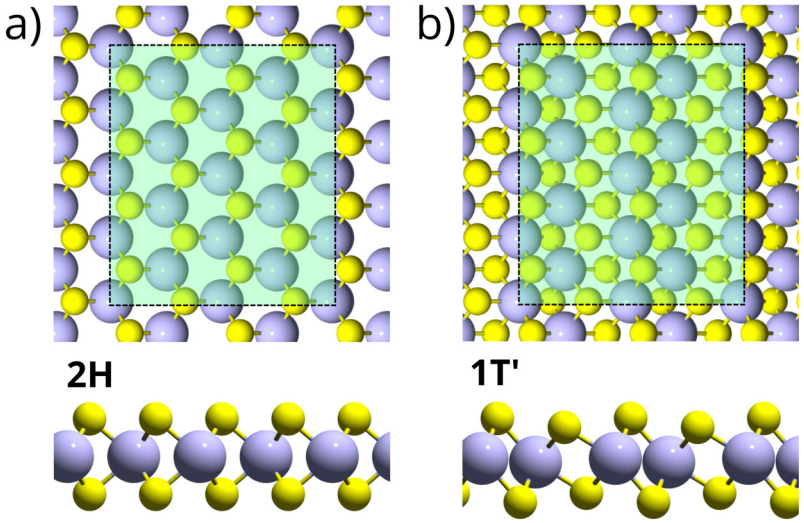

Figure 6.1: Top and side view of (a) 2H-MoS_2 and (b) 1T′-MoS_2 structures. Surface unit cells are marked with black dashed lines. Mo and S atoms are depicted as blue and yellow spheres, respectively.

From the total energy calculations we found that the energy difference of 0.83 eV per MoS_2 unit in favor of the 2H and compared to the undistorted 1T phase is reduced to 0.58 eV upon the emergence of 1T′ phase, in a good agreement with previous reports [77]. It is worth noting that the phase transition from the 1T′ phase to the most stable 2H phase does not happen at the room temperature as it requires very unfavorable sliding of the whole S plane. This process is hindered not only because of the artificial constraints that stem from the cell geometry but also because of the high energy barrier of this structural transition [77].

6.3 Adsorption of Li and Ca on MoS_2

We start our account on the adsorption of Li and Ca on 2H and 1T′ phases of MoS_2 with the identification of the most stable adsorption geometries of individual

adatoms. These structures are depicted in Fig. 6.2 and the results are summarized in the Table 6.1.

6.3.1 Li and Ca adatoms on MoS_2

When adsorb on 2H structure, both Li and Ca adatoms prefer to bind atop Mo atom and between three S atoms as depicted in Fig. 6.2a,c. The Li binding energy of 1.72 eV is accompanied by the charge transfer of 0.89 electrons from Li adatom to the 2H-MoS_2 surface as found from Bader analysis. These values are given in Table 6.1.

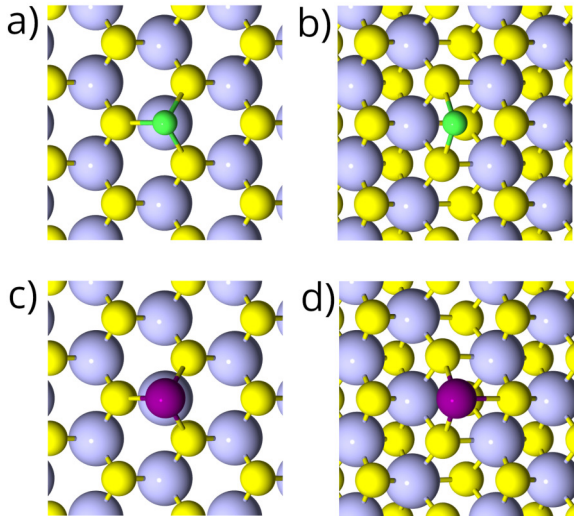

Figure 6.2: Adsorption geometries of individual (a-b) Li and (c-d) Ca adatoms on 2H (left) and 1T′ (right) phases of MoS_2. Coloring scheme of atomic spheres is as follows: Mo-blue, S-yellow, Li-green, and Ca-purple.

Atom-projected DOS of Li adatom on 2H surface plotted in Fig. 6.3 further supports this finding as the only Li valence electron is transferred from the Li-2s state mainly to the Mo-4d states located just above the CBM. This agrees well with the general

Table 6.1: Binding energy of Li and Ca adatoms on 2H and 1T′ phases of MoS_2, distances d from metal adatom to its nearest neighbors (S atoms) and electronic charge transfer ΔQ (in electrons) from metal adatom to the MoS_2 layer as calculated via Bader method.

Structure	E_B(eV)	d(Å)	ΔQ
Fig. 6.2a	1.72	2.39	0.89
Fig. 6.2b	3.28	2.34	0.90
Fig. 6.2c	1.26	2.72	1.21
Fig. 6.2d	4.41	2.55	1.47

trend explained in Chapter 5 for adsorption of Li on materials belonging to the *blue* group, where the Li binding picture is dominated by the simple charge transfer from Li to the surface.

The same analysis performed on Ca adatom adsorbed on 2H-MoS_2 reveals different binding picture compared to that of Li. The Ca binding energy of 1.26 eV is nearly 0.5 eV lower than the E_B of Li atom. In this case binding to the surface cannot be characterized solely by the charge transfer due to the hybridization of Ca and Mo states. This can be substantiated from the atom-projected DOS presented in Fig. 6.3 as the Ca-4*s* and Mo-5*d* states largely overlap in the vicinity of E_F.

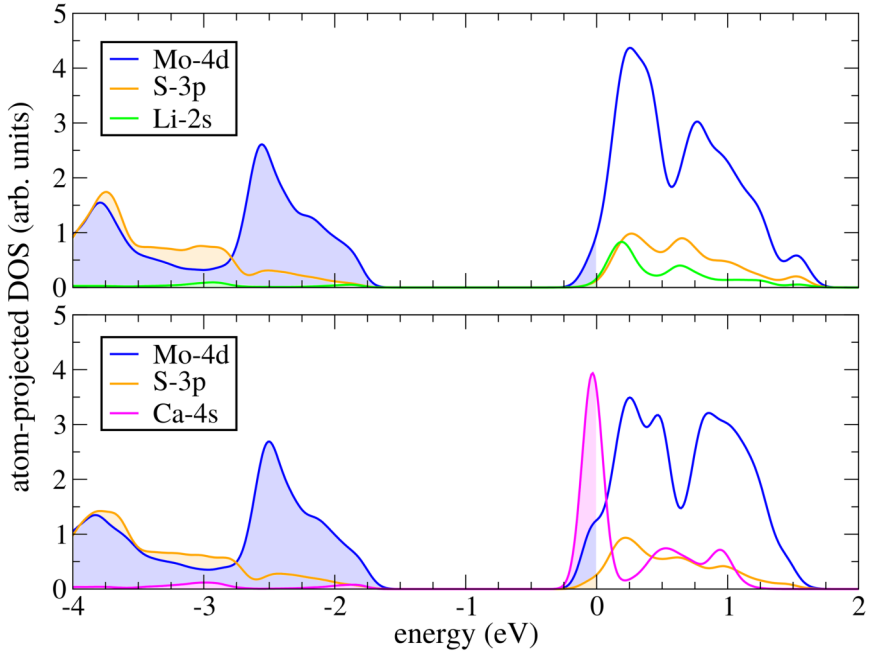

Figure 6.3: Atom-projected DOS of relevant atomic orbitals of Li (top panel) and Ca (bottom panel) adatoms adsorbed on 2H-MoS_2 in positions depicted in Fig. 6.2a,c. Zero of the energy scale is set to the Fermi level.

The 4*s* orbitals of Ca, still partly occupied upon the adsorption, are hybridized with the Mo-4*d* orbitals. Bader analysis reveals that 1.21 electrons are transferred from adatom to the surface, which is much less than the total number of 2 valence electrons that Ca adatom can donate to the surface. Furthermore, calculations performed on isolated Li and Ca atoms showed that Ca-4*s* state lies 0.52 eV below Li-2*s* state.[3] Thus, when electron is transferred from Li-2*s* state to the CBM of 2H-MoS_2 located at -4.25 eV below the vacuum level (see Table 5.2) the energy gain is greater than the gain following the transfer from Ca-4*s* state. This together

[3]As compared to the electrostatic vacuum, Li-2*s* and Ca-4*s* states lie at -3.17 eV and -3.69 eV, respectively.

with nearly one transferred electron in both cases partly explain why the Li binding energy is 0.46 eV larger than the Ca binding energy.

When Li and Ca atoms are adsorbed on 1T′ phase the most stable adsorption site is slightly displaced from the three-fold hollow position towards the closest Mo atom as depicted in Fig. 6.2b,d. As of Li adsorption, Bader analysis reveals 0.90 transferred electrons and atom-projected DOS plotted in Fig 6.4 confirms that Li-2s state is empty. Compared to the binding to 2H phase, both Li and Ca adatoms bind

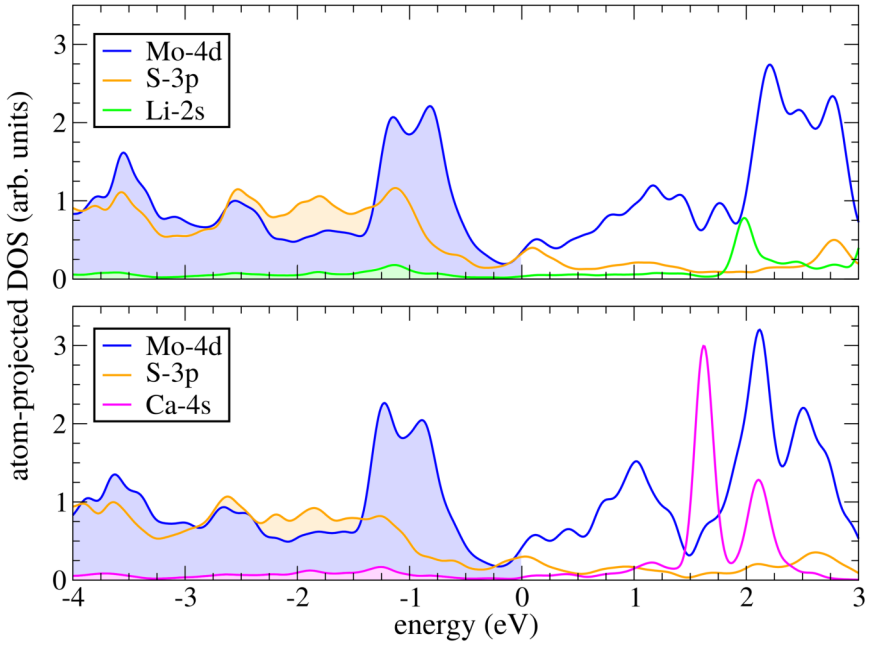

Figure 6.4: Atom-projected DOS of relevant atomic orbitals of Li (top panel) and Ca (bottom panel) adatoms adsorbed on 1T′-MoS_2 in positions depicted in Fig. 6.2b,d. Zero of the energy scale is set to the Fermi level.

much stronger to the 1T′ phase. Increase in Li binding energy of 1.56 eV is due to the position of E_F of metallic 1T′ phase. In fact, the E_F of 1T′ phase is located at -5.77 eV below the vacuum level, which is 1.52 eV lower than the position of CBM of 2H phase. This energy difference is well correlated with the difference in Li binding energies on the corresponding phases.

When Ca atom is adsorbed on 1T′-MoS_2 the binding picture is very similar to that of Li. There is no hybridization of Ca atomic states with the states from the surface as the energy of the highest occupied Mo-4d orbital is far from that of Ca-4s. Further, atom-projected DOS shows that Ca-4s state is completely empty, which is in a sharp contrast to the occupation of the same state when Ca is adsorbed on 2H phase. Charge transfer is 1.47 electrons and is much larger than the charge transfer from Ca adatom to the 2H phase. We report huge increase in the Ca binding energy,

as the corresponding value of 4.41 eV greatly exceeds E_B of Ca adatom on 2H phase which is only 1.26 eV. Moreover, it is also larger than the binding energy of Li on 1T′ phase. Compared to E_B of Ca adatom on 2H phase the vast increase in Ca binding energy on 1T′ phase is due to (1) the greater electron charge transfer from Ca adatom and (2) the position of the lowest unoccupied states of 1T′ phase which lie much deeper on energy scale than the CBM of 2H phase. Manifestations of stronger Ca binding are also visible in the distances between Ca atom and its nearest neighbors. This distance is 2.72 Å for 2H phase and is reduced to 2.55 Å when Ca is adsorbed on 1T′ phase. Thus, Ca atom is more immersed into the 1T′ structure and this fact can elucidate the results from Bader analysis which does not give the number of 2 transferred electrons because the charge basins of Ca largely overlap with those of its neighbors.

6.3.2 Effect of increase in adsorbate coverage on the relative stability of MoS_2 phases

Previous studies of MoS_2 structural stability propose different methods for fabrication of 1T and 1T′ phases of MoS_2 from the 2H phase. For instance, the adsorption of alkali metals on 2H-MoS_2 [177, 15] or the deposition of 2H-MoS_2 on suitable substrates [77] are often proposed strategies. We showed in Subsection 6.3.1 that the binding of a single Ca adatom to the 1T′-MoS_2 is much stronger than the Li binding to the same phase. Thus, the adsorption of Ca atoms on 1T′-MoS_2 leads to greater stabilization of this phase. Here we argue about the Li and Ca adsorption on MoS_2 as the viable routes for stabilization of 1T′ phase.

In order to investigate the effect of adsorbate coverage on the relative stability of Li- and Ca-adsorbed MoS_2 phases, we calculated the total energies of structures at very low coverage of $\Theta = 1/16$ ML (Fig. 6.2) and gradually increase the number of adatoms in the unit cell to compare the most stable 2H and 1T′ structures at coverages of $\Theta = 1/8$, 1/4, 3/8, 1/2 ML as depicted in Fig. 6.5. Energy differences are calculated per MoS_2 unit as follows

$$\Delta E = \frac{1}{16}\big(E(n\mathrm{M}/1\mathrm{T}') - E(n\mathrm{M}/2\mathrm{H})\big), \tag{6.1}$$

where M is either Li or Ca and n is the number of adatoms in the unit cell. Therefore, the positive values of ΔE correspond to the coverages at which 2H phase is the most stable one while the negative ΔE values are evidence that the relative stability of phases is reversed.

An increase in Li coverage stabilizes the 1T′ phase. The initial total energy difference of 0.58 eV per MoS_2 unit of pristine 2H and 1T′ phases reduces to 0.39 eV

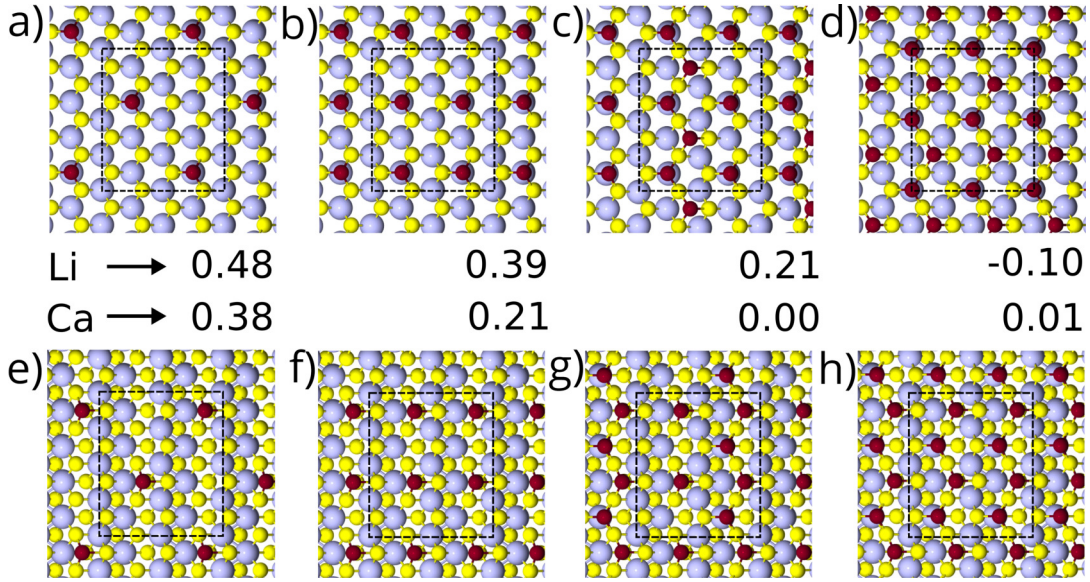

Figure 6.5: The most stable structures of 2H- and 1T′-MoS_2 at various coverages of Li and Ca. Upper panels: Li (Ca) adatoms on 2H-MoS_2 at coverages of (a) 1/8, (b) 1/4, (c) 3/8, and (d) 1/2 ML. Lower panels: Li (Ca) adatoms on 1T′-MoS_2 at coverages of (e) 1/8, (f) 1/4, (g) 3/8, and (h) 1/2 ML. The numbers between the upper and the lower panel are the differences in total energies of the 2H and 1T′ structures at corresponding coverages (in eV per MoS_2 unit). Coloring scheme of atomic spheres is as follows: Mo-blue, S-yellow, and Li/Ca-red.

at Li coverage of $\Theta = 1/4$ ML and finally the relative stability of phases is reversed at $\Theta = 1/2$ ML as the total energy of 1T′ phase becomes 0.10 eV lower than that of 2H phase. The difference in total energies of 2H and 1T′ phases drops linearly with increasing Li coverage as depicted in Fig. 6.6a. As stated in Subsection 6.3.1, when Li is adsorbed on MoS_2 the Li-2s electron is transferred to the lowest unoccupied states of the surface. This is a favorable process for both structural phases of MoS_2, because the CBM of 2H phase as well as the E_F of 1T′ phase are at lower energies as compared to the energy of the atomic Li-2s state. To substantiate the effect of an additional charge on the electronic states of the surface, we plotted the atom-projected DOS of Li adsorbed at coverages $\Theta = 1/16$, 1/4, 1/2 ML on the 2H and 1T′ phases in Fig. 6.7. From these plots we rationalize that the main effect of coverage increase is in the progressive filling of empty Mo-4d and S-3p states. Additionally, Fig. 6.7a shows that at coverage $\Theta = 1/2$ ML not all of the Li valence electrons are transferred to the surface as the Li-2s states are still partly occupied upon adsorption. This does not happen when Li is adsorbed at the same coverage on 1T′-MoS_2, as the atom-projected DOS plot in Fig. 6.7b shows completely empty Li-2s states.

On the other hand an increase in coverage strengthens the electrostatic repulsion

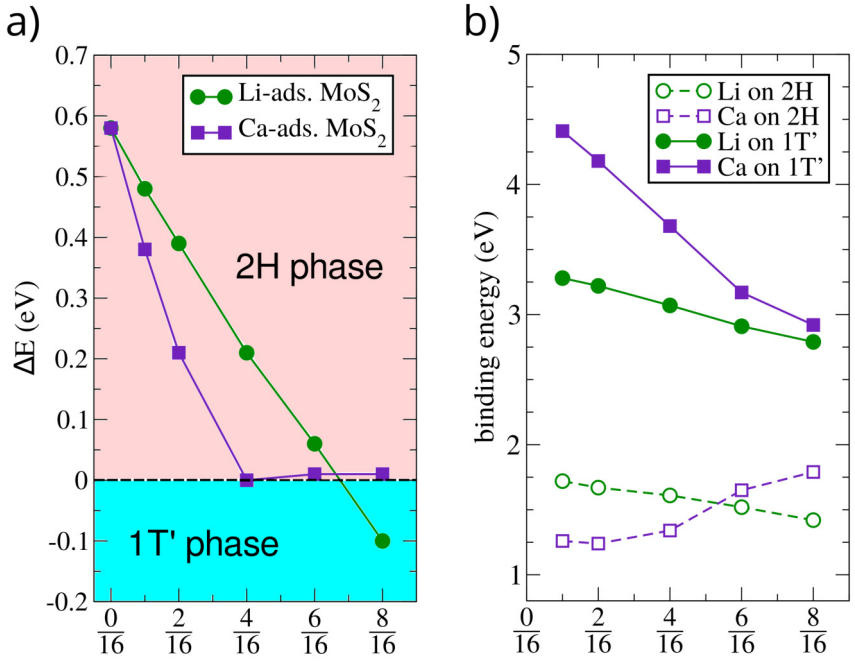

Figure 6.6: Evolution of (a) the total energy difference (ΔE, see eq. (6.1)) of 2H and 1T′ phases of MoS_2 and (b) the binding energy (per atom) of Li and Ca with the adsorbate coverage.

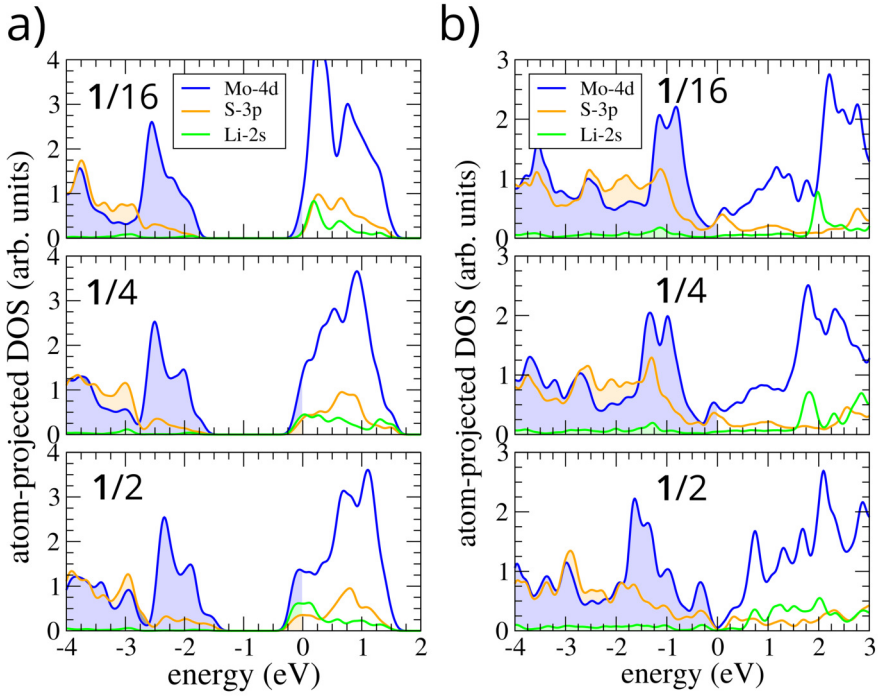

Figure 6.7: Atom-projected DOS of relevant atomic states of lithiated (a) 2H-MoS_2 and (b) 1T′-MoS_2. Atomic states are labeled in the legend and Li coverage (in ML) is displayed in each panel.

between Li adatoms, which further increases the total energy of the system. Thus, the relative stability of phases is the consequence of the interplay of these opposite contributions. To estimate the contribution of electrostatic Li-Li repulsion, we performed Bader analysis and revealed that the electron charge transfer from Li to the surface depends only slightly on the structural phase of MoS_2, as the obtained values range from 0.85 to 0.90 electrons for all studied coverages. Furthermore, the distances between Li adatoms at particular coverages are similar for both phases due to the nearly equal lattice constants of two phases. Similar amount of transferred charge and nearly equal distances between Li adatoms on both phases at the same coverage are indicators that the contribution of electrostatic repulsion to the total energy of 2H- and 1T′-MoS_2 is comparable. This is further supported by the fact that the rate of decrease in Li binding energy with the increase in coverage (Table 6.2) is similar for both phases as depicted in Fig. 6.6. This decrease is almost

Table 6.2: Binding energies in eV/atom of Li and Ca on 2H and 1T′ phases of MoS_2 at in the range from $\Theta = 1/16$ to $\Theta = 1/2$ ML.

Θ (ML)	1/16	1/8	1/4	3/8	1/2
Li on 2H	1.72	1.67	1.61	1.52	1.42
Ca on 2H	1.26	1.24	1.34	1.65	1.79
Li on 1T′	3.28	3.22	3.07	2.91	2.79
Ca on 1T′	4.41	4.18	3.68	3.17	2.92

entirely due to electrostatic repulsion between Li adatoms. Hence, an increase in coverage benefits to the 1T′ phase as its E_F is as much as 1.52 eV lower than the CBM of 2H phase (Subsection 6.3.1). We identified that Li coverage of $\Theta = 1/2$ ML is sufficient to stabilize the 1T′ phase (Fig. 6.6a).

Another viable route towards the stabilization of 1T′ phase is the adsorption of Ca. The binding energy of Ca adatom on 1T′ at low coverage of 1/16 ML is 4.41 eV, which is more than 3 eV higher than the binding energy on the 2H phase at the same coverage. With an increase in Ca coverage the difference between the total energies of 2H and 1T′ phases diminishes rapidly and finally at coverage of $\Theta = 1/4$ ML the total energy of 1T′ matches that of 2H phase, as depicted in Fig. 6.6a. However, an additional increase in Ca coverage does not lead to further stabilization of 1T′ phase and from the coverage of $\Theta = 1/4$ ML up to the $\Theta = 1/2$ ML the total energies of two phases are very similar (Fig. 6.6a).

The Ca binding energy at various coverages is presented in Table 6.2. Interestingly, it shows distinct behavior on two phases of MoS_2 – with the increase in coverage on 1T′ phase the E_B decreases while on the 2H phase it grows slowly, as

depicted in Fig. 6.6b. This is very different from the trends in Li binding energy, indicating that the Ca binding to the MoS_2 cannot be described solely by the simple charge transfer from the adsorbate to the surface.

To further inspect the differences in Ca binding on two phases of MoS_2, we plotted the atom-projected DOS for coverages $\Theta = 1/16$, $1/4$, $1/2$ ML as presented in Fig. 6.8. From these plots we can explain why the increase in coverage have

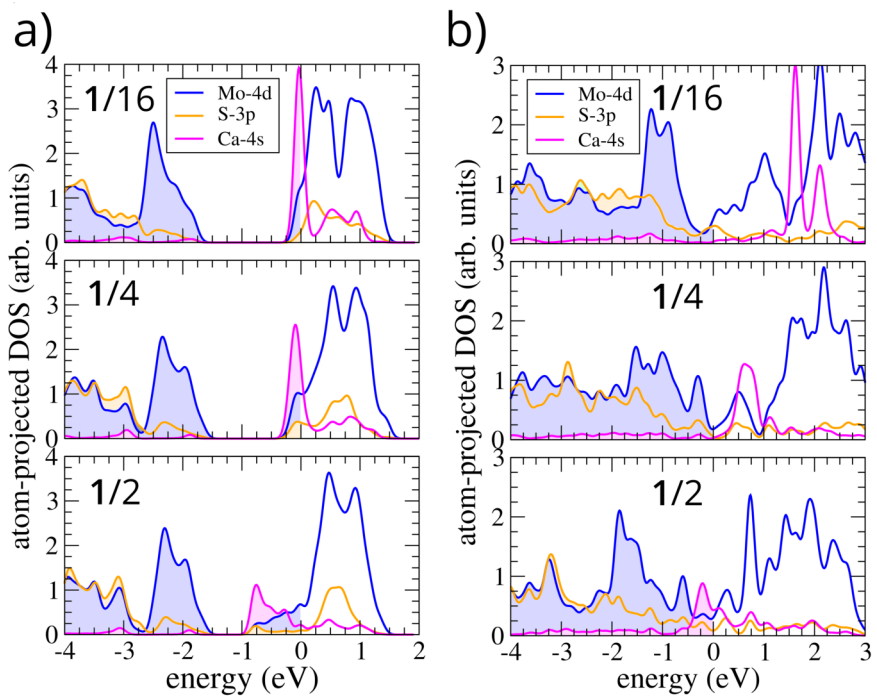

Figure 6.8: Atom-projected DOS of relevant atomic states of (a) 2H-MoS_2 and (b) 1T′-MoS_2 covered with calcium. Atomic states are labeled in the legend and Ca coverage (in ML) is displayed in each panel.

the opposite effects on the Ca binding energy on two phases. On both 2H and 1T′ phases the increase in coverage leads to the broadening of the Ca-4s states as depicted on plots that correspond to $\Theta = 1/2$ ML in Fig. 6.8. This is a clue that from the coverage of $\Theta = 1/4$ ML the neighboring Ca-4s states start to overlap, which leads to the formation of Ca-4s bands. As of 2H phase, with the increasing coverage the Ca-4s half-filled peak located at E_F moves to the region of (former) energy gap, where no electronic states existed prior to Ca adsorption. This lowers the total energy of the system as the filled electronic states move to lower energies.

On the other hand, the increase in Ca coverage on 1T′ phase from $\Theta = 1/16$ ML to $\Theta = 1/2$ ML (Fig. 6.8b) has two main effects on the electronic structure of the system. Firstly, the pronounced peak belonging to the Ca-4s state that was completely empty at coverages $\Theta = 1/16$ ML and $\Theta = 1/4$ ML is broadens and

partly fills at coverage of $\Theta = 1/2$ ML. Moreover, Bader analysis reveals that the charge transfer of 1.47 electrons from Ca to the surface at coverage $\Theta = 1/16$ ML is drastically reduced to 0.96 electrons when the coverage is increased to $\Theta = 1/2$ ML. This confirms that the simple binding picture build upon the charge transfer from adsorbate to the 1T′ surface does not hold for coverages higher than $\Theta = 1/4$ ML due to formation of Ca-Ca bonds which hinders the charge transfer. Secondly, an increase in Ca coverage destabilizes filled Mo-4*d* states as the peak located at -0.6 eV below E_F emerges. This gives rise to an increase in the total energy of the system as this peak is higher in energy than the rest of filled *d* states.

To conclude this Chapter, we present in Fig. 6.9 the plot of work function of Li- and Ca-adsorbed 1T′-MoS_2. From this plot one can substantiate the difference

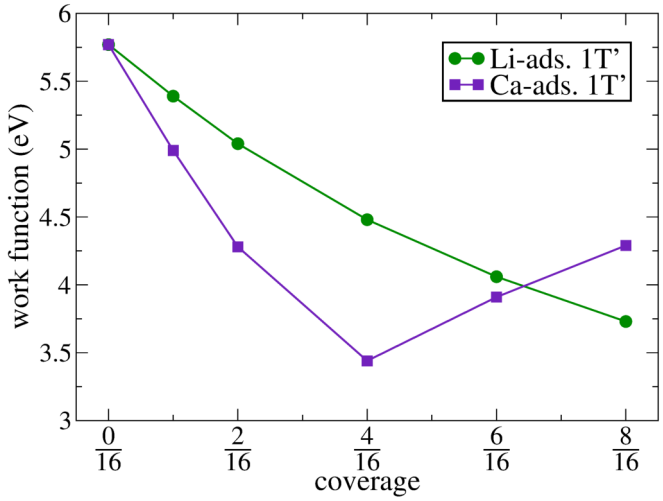

Figure 6.9: Work function of pristine 1T′-MoS_2 as well as of Li- and Ca-adsorbed 1T′-MoS_2 at coverages $\Theta = 1/16$, 2/16, 4/16, 8/16 ML.

between the Li- and Ca-covered 1T′ phase. The work function of Li-covered 1T′-MoS_2 monotonically decreases with the increase in coverage, as the Mo-4*d* and S-3*p* states from the conduction band are being gradually filled. Therefore, the energies of the highest occupied states are coming closer to the vacuum level and work function slowly reduces. On the other hand, the work function of 1T′-MoS_2 steeply drops off when Ca is adsorbed up to the coverage $\Theta = 1/4$ ML but then starts to grow as coverage is further increased. This is an evidence that the nature of the MoS_2 surface changes at high Ca coverages due to the formation of Ca layer.

Though we found no clear evidence that Ca adsorption can trigger the 2H→1T′ phase transition as the total energies of two phases are similar for coverages higher than $\Theta = 1/4$ ML, we suspect that Ca adsorption can be a viable route to stabilize 1T′ phase at much lower coverages than the adsorption of Li. Previous studies

reported that the choice of a suitable substrate can stabilize the 1T′ phase [77] and in experimental conditions the MoS_2 layer must be suspended. Thus, the joined effect of the suitable substrate and of the charge transfer from the Ca adsorbate can be used as a possible strategy for the stabilization of the 1T′ phase.

Conclusions

"The final result of our efforts as scientists is, after all, not a table of data, a set of equations or the output of a computer. It is an essay, a piece of expository prose. That's what grant officers, promotion committees and biographers care about and for once they're right." , (N. David Mermin, *What's wrong with this prose?*)

In a broad sense, the discussion presented in this dissertation addresses the problems of paramount scientific and technological importance, such as the cutting edge transistor nanotechnology and advanced energy storage. More precisely, in this thesis we applied the *ab initio* computational methods based on DFT to study the structural and electronic properties of metals adsorbed on 2D materials. Special attention has been paid to graphene, as the growth modes of different metals on this 2D crystal have been rationalized from the description of the adsorption of their adatoms and small clusters. The conclusions drawn from the behavior of Li on graphene served as a firm basis for further research on the adsorption of this alkaline metal on other 2D crystals, where the general Li binding trend is successfully explained by a simple charge transfer. Once again, lithium ability to donate electrons to the substrate is exploited for another role – as an initiator of the structural phase transition in MoS_2. The Li coverage of MoS_2 that sufficient enough to trigger the phase transition is determined, where it is shown that the same effect can be achieved with the usage of calcium adsorbates at smaller coverages.

Owing to its remarkable mechanical and electronic properties, graphene is a 2D crystal that bears a burden of high expectations. Fortunately, various methods of graphene's functionalization are paving the way towards reaching its full potential in electronic devices, and for that cause, the understanding of the interaction of graphene with metals is of ultimate importance. Considering this, we investigated the adsorption of Li, Ca and Ti atoms and small clusters on graphene by means of DFT in order to describe their contacts with this 2D crystal at the fundamental level. From the study of dimer adsorption on graphene, we found that the interaction between metal adatoms plays a critical role in the shape of nanostructures formed

on graphene. In line with the previous studies, we demonstrated the tendency of alkaline metals to arrange in sparse monolayers due to long-range electrostatic repulsion between adatoms.

The cohesive energies of transition metals are significantly larger than the binding energies of their adatoms on graphene. Thus, in order to minimize the total energy of the structure, transition metal atoms adsorbed on graphene gather into 3D clusters. On the other hand, the modest attraction between Ca adatoms causes the formation of 2D nanostructures with a rather high density of states at Fermi level. Upon intercalation with a monoatomic Ca layer, we found a nearly three-fold increase in the adhesion energy between graphene sheets as compared to that of a pristine graphene bilayer. With the help of Bader analysis, the inspection of charges on Ca and C atoms proved that the electrostatic attraction between graphene layers and Ca adsorbate is the origin of such enhancement in adhesion. Moreover, as opposed to 2D layers of alkaline metals, Ca monolayer on graphene is thermodynamically a very stable structure and thus could be potentially used either as an ultra-thin electrode or to improve contacts between 2D materials in their vertical heterostructures.

We further examined Li binding at fifteen different 2D crystals, with the particular choice of materials motivated by their relevance in the ongoing researches of LIBs. The expectation that at low coverage Li binding to 2D crystals causes only minor changes in their structural properties, while the effect of the adsorbate on the electronic properties of surfaces is limited to a simple charge transfer, was confirmed for the majority of studied 2D structures. Employing the position of the CBM of studied surfaces as a single parameter describing their electronic properties, for the majority of considered 2D materials we found an excellent correlation between CBM and the binding energy of Li adatom. Yet, a much more complicated Li binding picture which involves considerable structural deformation alongside with the qualitative changes in electronic properties of 2D crystals was found in four of investigated 2D crystals – graphane, SiC, GeC, and SnC.

The discrepancy observed in carbides of Group XIV elements and graphane was explained in terms of midgap states that emerge from Li adsorption. Due to localized nature of the interaction between Li and these surfaces, they can preserve the nearly constant value of Li binding energy for adsorbates varying from single adatoms to ordered structures with Li coverage of up to 1 ML. From DFT studies we identify SnC as a particularly promising 2D crystal for applications as the electrodes of LIBs, since it displays high structural stability, together with a modest variation in Li binding energy over a wide range of Li coverage. These results indicate that sheets of SnC combined with other 2D materials in multilayers or vdW heterostructures

could serve as building blocks of materials able to easily store and release a large amount of Li. However, the energetics of Li binding in multilayers of 2D materials is different from the binding on single layers and further studies are needed to confirm this assumption.

Finally, we investigated the structural and electronic properties of two different phases of MoS_2, namely the most stable semiconducting 2H phase, and the metallic 1T$'$ phase which is spontaneously obtained from the undistorted 1T phase. Differences in Li and Ca adsorption on two phases of MoS_2 are substantiated by applying DFT to calculate the charge transfer from adsorbate to the surface and also to reveal the character of the electronic states in the vicinity of Fermi level. Following the explained trend in Li adsorption on 2D crystals, we found that Li binding to both MoS_2 phases is fully described by the simple charge transfer. Moreover, the difference in Li binding energy on 2H and 1T$'$ phase is governed by the distinct positions of the corresponding lowest unoccupied states of pristine surfaces on the energy scale.

As expected, the Ca interaction with MoS_2 does not follow the same trend as Li. This discrepancy is due to the combined effect of the hybridization of Ca-4*s* states with Mo-4*d* states and the partial formation of Ca monolayer due to moderate Ca-Ca attraction at higher coverages. However, the adsorption of Ca on 2H-MoS_2 can be efficiently utilized to trigger the 2H$\rightarrow$1T$'$ phase transition, with an additional advantage that this is achived at Ca coverage that is twice lower than that of Li. Differences in electronic structure of Li- and Ca-covered MoS_2 result in a very dissimilar behavior of the corresponding work functions.

We believe that the results presented in this thesis will contribute to the full understanding of microscopic mechanisms governing the adsorption of metals on 2D materials. As a particularly interesting research field we consider metal contacts with vdW heterostructures of 2D crystals where the proper choice of 2D building blocks enables designing of synthetic materials with targeted properties thus showing great technological promise.

Appendix A

Adiabatic approximation

In Chapter 1 we stated that degrees of freedom of nuclei and electrons for a great deal of systems can be separated thus greatly simplifying the treatment of such systems. This appendix is devoted to the theoretical foundation of the adiabatic approximation and closely follows the discussions in references [181, 25].

The hamiltonian for a system of nuclei and electrons (1.1) can be written as

$$\hat{H} = \hat{T}_N + \hat{T}_e + \hat{U}(\{\mathbf{r}, \mathbf{R}\}), \tag{A.1}$$

where $\hat{T}_N = -\frac{1}{2}\sum_J \nabla_J^2/M_J$ and $\hat{T}_e = -\frac{1}{2}\sum_i \nabla_i^2$ are kinetic energies of nuclei and electrons, respectively. The term $\hat{U}$ contains all the potential interaction in the system and depends on the sets of all the electronic positions and spins $\{\mathbf{r}\} = (\mathbf{r}_1\sigma_1, \ldots \mathbf{r}_N\sigma_N)$ as well as the positions of all the nuclei $\{\mathbf{R}\} = (\mathbf{R}_1, \ldots, \mathbf{R}_P)$, where $N(P)$ is the number of electrons (nuclei).[1] We argued that the kinetic energy of nuclei is much smaller than the other terms hence it can be treated as a perturbation upon a family of electronic hamiltonians $\hat{H}_e(\{\mathbf{R}\}) = \hat{T}_e + \hat{U}(\{\mathbf{r}, \mathbf{R}\})$ parameterized by the set of fixed nuclear positions $\{\mathbf{R}\}$. Let us rewrite the original time-independent Schrödinger equation for a coupled system of nuclei and electrons

$$\hat{H}\Psi_s(\{\mathbf{r}, \mathbf{R}\}) = E_s\Psi_s(\{\mathbf{r}, \mathbf{R}\}), \tag{A.2}$$

where $s = 0, 1, 2 \ldots$ labels the states of a coupled system. The first step is to fix nuclei at their instantaneous positions $\{\mathbf{R}\}$ and define the eigenvalues $\epsilon_i(\{\mathbf{R}\})$ and wavefunctions $\psi_i(\{\mathbf{r}\} : \{\mathbf{R}\})$ for the electrons. In this sense, eigenvalues and wavefunctions of electrons depends parametrically upon nuclear positions $\{\mathbf{R}\}$ and the Schrödinger equation for electrons can be written as:

$$\hat{H}_e(\{\mathbf{R}\})\psi_i(\{\mathbf{r}\} : \{\mathbf{R}\}) = \epsilon_i(\{\mathbf{R}\})\psi_i(\{\mathbf{r}\} : \{\mathbf{R}\}). \tag{A.3}$$

[1] It is implicitly assumed that the system is electroneutral.

For each nuclear configuration $\{\mathbf{R}\}$ wavefunctions $\psi_i(\{\mathbf{r}\} : \{\mathbf{R}\})$ span the entire state space of electrons. Accordingly, each wavefunction for the coupled system can be written as a linear combination of electronic wavefunctions with expansion coefficients depending upon nuclear positions as parameters:

$$\Psi_s(\{\mathbf{r}, \mathbf{R}\}) = \sum_j \chi_{sj}(\{\mathbf{R}\})\psi_j(\{\mathbf{r}\} : \{\mathbf{R}\}). \tag{A.4}$$

In order to find equations for $\chi_{si}(\{\mathbf{R}\})$ we need to insert expansion (A.4) into (A.2), multiply on the left by $\psi_i^*(\{\mathbf{r}\} : \{\mathbf{R}\})$ and integrate over all electron positions $\{\mathbf{r}\}$. Then, applying the orthogonality condition for the electronic states $\langle\psi_i|\psi_j\rangle = \delta_{ij}$ we get:

$$\left[\hat{T}_N + \epsilon_i(\{\mathbf{R}\}) - E_s\right] \chi_{si}(\{\mathbf{R}\}) = \sum_j \Lambda_{ij}\chi_{sj}(\{\mathbf{R}\}). \tag{A.5}$$

where the matrix elements of *the non-adiabatic operator* are given by $\Lambda_{ij}(\{\mathbf{R}\}) = \alpha_{ij}(\{\mathbf{R}\}) + \beta_{ij}(\{\mathbf{R}\})$ where

$$\begin{aligned} \alpha_{ij} &= \sum_J \frac{1}{M_J} \int \mathrm{d}^3\{\mathbf{r}\}\psi_i^*(\{\mathbf{r}\} : \{\mathbf{R}\})\big(\nabla_J\psi_j(\{\mathbf{r}\} : \{\mathbf{R}\})\big)\nabla_J, \\ \beta_{ij} &= \sum_J \frac{1}{2M_J} \int \mathrm{d}^3\{\mathbf{r}\}\psi_i^*(\{\mathbf{r}\} : \{\mathbf{R}\})\big(\nabla_J^2\psi_j(\{\mathbf{r}\} : \{\mathbf{R}\})\big). \end{aligned} \tag{A.6}$$

The adiabatic or Born-Oppenheimer approximation [182] is to ignore the *off-diagonal terms* of the non-adiabatic operator $\hat{\Lambda}$, i.e. the terms which include wavefunctions of different electronic states. In other words, electrons remain in a given state as the nuclei move. There is no net energy transfer between nuclear and electronic degrees of freedom. In addition to this, as the electronic wavefunctions are normalized and consequently $\nabla_J \langle\psi_i|\psi_i\rangle = 0$, it is easy to show that the diagonal terms of α vanish, $\alpha_{ii} = 0$. Moreover, the diagonal terms of matrix β can be grouped with $\epsilon_i(\{\mathbf{R}\})$ into a modified potential for nuclei $\tilde{\epsilon}_i(\{\mathbf{R}\}) = \epsilon_i(\{\mathbf{R}\}) + \beta_{ii}(\{\mathbf{R}\})$. Hence, in the adiabatic approximation, the motion of nuclei are governed by a purely nuclear equation for each electronic state i,

$$\left[-\sum_J \frac{\nabla_J^2}{2M_J} + \tilde{\epsilon}_i(\{\mathbf{R}\})\right]\chi_{ni}(\{\mathbf{R}\}) = E_{ni}\chi_{ni}(\{\mathbf{R}\}), \tag{A.7}$$

where $n = 0, 1, 2, \ldots$ labels the nuclear states. Within the adiabatic approximation, the system is decoupled but the price is that the full state space is restricted to *a direct product* of the nuclear and electronic state subspaces, that is $\mathcal{S} = \mathcal{S}_N \otimes \mathcal{S}_e$. In other words, as nuclei are frozen in their instantaneous positions, the evolution of electronic states is confined to a fixed Born-Oppenheimer surface. Actually, the

exact wavefunction for the electronic-nuclear system is an appropriate linear combination of the products belonging to different Born-Oppenheimer surfaces. Physically, this means that when the nuclei are in motion, the electronic-nuclear system cannot be strictly confined to a given adiabatic surface. Still, this approximation works well except for cases where there is (near) degeneracy of the electronic states. When there is a gap in the electronic spectrum much larger than the typical energies for nuclear motion then the nuclear excitation spectrum is well determined by the adiabatic terms. Though, one must be careful when dealing with metals which lacks an energy gap or molecules whose electronic transition states become degenerate. For in-depth coverage of this topic, we refer to [181].

Appendix B

Electronic bands of graphene in tight-binding approach

This appendix is a complement to Chapter 3. Within the tight-binding model, we will derive the expressions for the bands near the Fermi level, π bands, which are responsible for many distinct electronic properties of graphene.

B.1 Tight-binding model

The eigenstates for electrons in crystals, as explained in Chapter 2, are described by Bloch functions with periodicity of the crystal lattice. The Bloch functions are constructed from the atomic orbitals $\phi_i(\mathbf{r})$ as follows

$$\Phi_{i,\mathbf{k}}(\mathbf{r}) = \frac{1}{\sqrt{N}} \sum_{\mathbf{R}} e^{\mathrm{i}\mathbf{k}\cdot\mathbf{R}} \phi_i(\mathbf{r} - \mathbf{R}) \tag{B.1}$$

where N is the total number of unit cells in the crystal, $\mathbf{R}$ are lattice vectors and i labels atomic orbitals in the unit cell. If we have n relevant orbitals, the wavefunction for electrons in crystal can be represented as a linear combination of Bloch functions,

$$\psi_{j,\mathbf{k}}(\mathbf{r}) = \sum_{i=1}^{n} C_{ji}(\mathbf{k}) \Phi_{i,\mathbf{k}}(\mathbf{r}). \tag{B.2}$$

The coefficients $C_{ji}(\mathbf{k})$ are to be determined from the variational principle (1.11),

$$\varepsilon_j(\mathbf{k}) = \frac{\sum_{i,l=1}^{n} C_{ji}^* C_{jl} \langle \Phi_i | \hat{H} | \Phi_l \rangle}{\sum_{i,l=1}^{n} C_{ji}^* C_{jl} \langle \Phi_i | \Phi_l \rangle} = \frac{\sum_{i,l=1}^{n} C_{ji}^* C_{jl} H_{il}(\mathbf{k})}{\sum_{i,l=1}^{n} C_{ji}^* C_{jl} S_{il}(\mathbf{k})}, \tag{B.3}$$

where $\hat{H}$ is the crystal hamiltonian, $H_{il}(\mathbf{k}) = \langle \Phi_i | \hat{H} | \Phi_l \rangle$ are elements of *the transfer integral matrix* $\mathcal{H}$ and $S_{il}(\mathbf{k}) = \langle \Phi_i | \Phi_l \rangle$ are the elements of *the overlap integral matrix* $\mathcal{S}$.

For a given $\mathbf{k}$, by varying $\varepsilon_j(\mathbf{k})$ with respect to C^*_{jm} (which are also $\mathbf{k}$ dependent), the local minimum condition yields

$$\frac{\partial \varepsilon_j(\mathbf{k})}{\partial C^*_{jm}} = \frac{\sum_l^n H_{ml} C_{jl}}{\sum_{i,l}^n S_{il} C^*_{ji} C_{jl}} - \frac{\sum_{i,l}^n H_{il} C^*_{ji} C_{jl} \sum_l^n S_{ml} C_{jl}}{\left(\sum_{i,l}^n S_{il} C^*_{ji} C_{jl}\right)^2} = 0. \tag{B.4}$$

From expressions (B.2) and (B.3) we obtain

$$\sum_{l=1}^{n} H_{ml} C_{jl} = \varepsilon_j \sum_{l=1}^{n} S_{ml} C_{jl},\ m = 1, 2, \ldots, n \quad \Leftrightarrow \quad [\mathcal{H} - \varepsilon_j(\mathbf{k})\mathcal{S}]\mathcal{C}_j = 0, \tag{B.5}$$

where we have introduced a column vector $\mathcal{C}_j = (C_{j1}, \ldots, C_{jn})^T$. The energies $\varepsilon_j(\mathbf{k})$ can be obtained from the condition that the determinant for the homogeneous system of equations (B.5) must be zero,

$$\det[\mathcal{H} - \varepsilon_j(\mathbf{k})\mathcal{S}] = 0. \tag{B.6}$$

The equation (B.6) is called *secular equation*. It is an equation of degree n, thus its solution gives all n eigenvalues $\varepsilon_j(\mathbf{k})$, $j = 1, 2, \ldots, n$ for a given $\mathbf{k}$.

B.2 π bands of graphene

Graphene elementary cell contains two atoms, A and B (Fig. 3.2a). Thus we need to include two $2p_z$ atomic orbitals in the tight-binding for the π bands, one for each atom. The band energy is obtained from the secular equation of the system,

$$\begin{pmatrix} H_{AA}(\mathbf{k}) & H_{AB}(\mathbf{k}) \\ H_{BA}(\mathbf{k}) & H_{BB}(\mathbf{k}) \end{pmatrix} \begin{pmatrix} \psi_{A,\mathbf{k}} \\ \psi_{B,\mathbf{k}} \end{pmatrix} = \varepsilon(\mathbf{k}) \begin{pmatrix} S_{AA}(\mathbf{k}) & S_{AB}(\mathbf{k}) \\ S_{BA}(\mathbf{k}) & S_{BB}(\mathbf{k}) \end{pmatrix} \begin{pmatrix} \psi_{A,\mathbf{k}} \\ \psi_{B,\mathbf{k}} \end{pmatrix}. \tag{B.7}$$

The matrix elements of $\mathcal{H}$ and $\mathcal{S}$ must be calculated for each $\mathbf{k}$ from expressions

$$\begin{aligned}
H_{AA}(\mathbf{k}) &= \frac{1}{N} \sum_{i,j=1}^{N} \mathrm{e}^{\mathrm{i}\mathbf{k}(\mathbf{R}_{A,j} - \mathbf{R}_{A,i})} \langle \phi_A(\mathbf{r} - \mathbf{R}_{A,i}) | \hat{H} | \phi_A(\mathbf{r} - \mathbf{R}_{A,j}) \rangle, \\
H_{AB}(\mathbf{k}) &= \frac{1}{N} \sum_{i,j=1}^{N} \mathrm{e}^{\mathrm{i}\mathbf{k}(\mathbf{R}_{B,j} - \mathbf{R}_{A,i})} \langle \phi_A(\mathbf{r} - \mathbf{R}_{A,i}) | \hat{H} | \phi_B(\mathbf{r} - \mathbf{R}_{B,j}) \rangle, \\
S_{AA}(\mathbf{k}) &= \frac{1}{N} \sum_{i,j=1}^{N} \mathrm{e}^{\mathrm{i}\mathbf{k}(\mathbf{R}_{A,j} - \mathbf{R}_{A,i})} \langle \phi_A(\mathbf{r} - \mathbf{R}_{A,i}) | \phi_A(\mathbf{r} - \mathbf{R}_{A,j}) \rangle, \\
S_{AB}(\mathbf{k}) &= \frac{1}{N} \sum_{i,j=1}^{N} \mathrm{e}^{\mathrm{i}\mathbf{k}(\mathbf{R}_{B,j} - \mathbf{R}_{A,i})} \langle \phi_A(\mathbf{r} - \mathbf{R}_{A,i}) | \phi_B(\mathbf{r} - \mathbf{R}_{B,j}) \rangle.
\end{aligned} \tag{B.8}$$

The rest of the matrix elements related to $(B.8)$ as $H_{BB} = H_{AA}$, $S_{BB} = S_{AA}$, $H_{BA} = H^*_{AB}$ and $S_{BA} = S^*_{AB}$.

The expression for H_{AA} in (B.8) includes a double summation over all the sites of the A sublattice. In *the approximation of the nearest neighbors* all the terms in H_{AA} must vanish, except those which contain the orbitals from the same site, i.e. those for which $i = j$. The reason is that the nearest neighbors to the atoms from the sublattice A are from the sublattice B (see Fig. (3.2a)). Hence, H_{AA} will not depend on $\mathbf{k}$ and can be found as follows

$$H_{AA} \approx \frac{1}{N}\sum_{i=1}^{N} \langle \phi_A(\mathbf{r}-\mathbf{R}_{A,i})|\hat{H}|\phi_A(\mathbf{r}-\mathbf{R}_{A,i})\rangle \approx \frac{1}{N}\sum_{i=1}^{N} \epsilon_{2p} = \epsilon_{2p} \tag{B.9}$$

where ϵ_{2p} is nearly equal to the energy of the free $2p_z$ orbital.[1] Similarly, as overlap of the atomic orbitals from the different A sites is negligible, the diagonal elements of the matrix $\mathcal{S}$ will contain only the terms for which $i = j$

$$S_{AA} \approx \frac{1}{N}\sum_{i=1}^{N} \langle \phi_A(\mathbf{r}-\mathbf{R}_{A,i})\big|\phi_A(\mathbf{r}-\mathbf{R}_{A,i})\rangle = 1, \tag{B.10}$$

as atomic orbitals are orthonormal.

The $\mathbf{k}$ dependence of $\varepsilon(\mathbf{k})$ comes from the off-diagonal matrix elements H_{AB} and S_{AB}. In the nearest neighbor approximation, for every atom A (i.e. for every i in the sum (B.8)) there are three nearest neighbors from the sublattice B (Fig. 3.2a). Their positions relative to the atom A are

$$\boldsymbol{\delta}_1 = \left(0, \frac{a}{\sqrt{3}}\right), \quad \boldsymbol{\delta}_2 = \left(\frac{a}{2}, -\frac{a}{2\sqrt{3}}\right), \quad \boldsymbol{\delta}_3 = \left(-\frac{a}{2}, -\frac{a}{2\sqrt{3}}\right). \tag{B.11}$$

Neglecting all the other terms, the expressions for H_{AB} and S_{AB} become

$$\begin{aligned} H_{AB}(\mathbf{k}) &\approx \frac{1}{N}\sum_{i=1}^{N}\sum_{l=1}^{3} \mathrm{e}^{\mathrm{i}\mathbf{k}\cdot\boldsymbol{\delta}_l} \langle \phi_A(\mathbf{r}-\mathbf{R}_{A,i})|\hat{H}|\phi_B(\mathbf{r}-\mathbf{R}_{B,l})\rangle = -\gamma f(\mathbf{k}), \\ S_{AB}(\mathbf{k}) &\approx \frac{1}{N}\sum_{i=1}^{N}\sum_{l=1}^{3} \mathrm{e}^{\mathrm{i}\mathbf{k}\cdot\boldsymbol{\delta}_l} \langle \phi_A(\mathbf{r}-\mathbf{R}_{A,i})|\phi_B(\mathbf{r}-\mathbf{R}_{B,l})\rangle = s f(\mathbf{k}), \end{aligned} \tag{B.12}$$

where $\gamma = -\langle \phi_A(\mathbf{r}-\mathbf{R}_{A,i})|\hat{H}|\phi_B(\mathbf{r}-\mathbf{R}_{B,l})\rangle$ and $s = \langle \phi_A(\mathbf{r}-\mathbf{R}_{A,i})|\phi_B(\mathbf{r}-\mathbf{R}_{B,l})\rangle$ are *transfer* and *overlap integrals*, respectively, which can be determined from *ab initio* calculations. All the $\mathbf{k}$-dependence of energy bends originates from the complex function which can be easily calculated from (B.11)

$$f(\mathbf{k}) = \sum_{l=1}^{3} \mathrm{e}^{\mathrm{i}\mathbf{k}\boldsymbol{\delta}_l} = \mathrm{e}^{\mathrm{i}k_y a/\sqrt{3}} + 2\cos\left(\frac{k_x a}{2}\right)\mathrm{e}^{-\mathrm{i}k_y a/2\sqrt{3}}. \tag{B.13}$$

[1] ϵ_{2p} is not strictly equal to the energy of the free $2p_z$ orbital as the hamiltonian $\hat{H}$ contains also the crystal potential.

Transfer and overlap integral matrix are

$$\mathcal{H} = \begin{pmatrix} \epsilon_{2p} & -\gamma f(\mathbf{k}) \\ -\gamma f^*(\mathbf{k}) & \epsilon_{2p} \end{pmatrix}, \qquad \mathcal{S} = \begin{pmatrix} 1 & sf(\mathbf{k}) \\ sf^*(\mathbf{k}) & 1 \end{pmatrix}. \tag{B.14}$$

Secular equation for this system of equations

$$\big(\varepsilon(\mathbf{k}) - \epsilon_{2p}\big)^2 - \big((E - \epsilon_{2p})s + \epsilon_{2p}s + \gamma\big)^2 |f(\mathbf{k})|^2 = 0 \tag{B.15}$$

yields the solution - the energy dispersion of π band ($-$ sign) and π^* band ($+$ sign) of graphene within the tight-binding model

$$\varepsilon_{\pm}(\mathbf{k}) = \frac{\epsilon_{2p} \pm \gamma |f(\mathbf{k})|}{1 \mp s|f(\mathbf{k})|}. \tag{B.16}$$

π bands along the high symmetry directions of BZ are presented in Fig. B.1.

In a like manner the σ bands of graphene can be obtained if we include from orbitals $2s$, $2p_x$ and $2p_y$. As elementary cell contains two atoms, the six σ bands can be obtained from the 6×6 transfer and overlap integral matrices. Solution of this problem can be found in [85], p. 29-33.

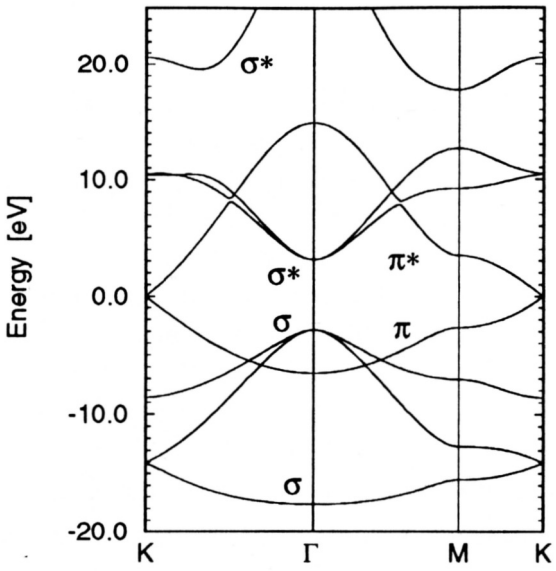

Figure B.1: Energy bands of graphene calculated within the tight-binding model. Parameters used in calculations are given in Table 2.1 of [85].

Appendix C

Computational details

Here we gather the computational details which are common for all DFT calculations that yielded the results presented in Chapters 4–6.

Atomistic structures considered in this work, that is pristine 2D crystals as well as 2D crystals with atoms and/or molecules/clusters adsorbed on their surface, are set up using the Atomic Simulation Environment (ASE) [183]. This is a set of tools and Python modules for setting up, manipulating, running, visualizing and analyzing atomistic simulations.

DFT calculations are carried out using GPAW code [17] based on the real-space projector augmented wave method [63, 66]. The basics of PAW method can be found in Chapter 2. The wavefunctions, i.e. Kohn-Sham orbitals, within this approach are represented on a real space grid with the spacing of 0.15 Å.

The convergence criteria during the self-consistency cycle are as follows: the energy between the last three consecutive iterations changes less than 0.5 meV, the change in integrated absolute value of electron density is less than 0.0001 electrons per valence electron and the integrated value of the square of residuals of the Kohn-Sham equations is less than $1.0 \times 10^{-6}\,\mathrm{eV}^2$ per valence electron. Eigenstates are converged up to the 1×10^{-7} eV. During the self-consistency cycle, we used the Pulay scheme [184, 185] to construct the input electron density for the next iteration by mixing the densities from several previous iterations. To improve the convergence, we used the smearing of the occupation numbers according to Fermi-Dirac distribution, with smaller temperatures in the range of $0.01 - 0.03$ eV for spin-polarized calculations (as magnetic moments are sensitive to smearing) and larger temperatures of $0.05 - 0.1$ eV for non-magnetic structures.

The exchange and correlation effects in the electron gas are treated within the generalized-gradient approximation using the parameterization provided by Perdew, Burke, and Ernzerhof (PBE) [186]. The GGA approximation as well as this particular parametrization of XC functional are explained in Chapter 1. The exceptions

for usage of PBE functional were systems which contain two or more layers that are close to each other, e.g. bilayer graphene whose intercalation with calcium is studied in Chapter 4. In cases like this the van der Waals interaction between layers, not included in standard GGA approximations, becomes essential. Thus we used the optB88-vdW functional which combines the opt-B88 exchange functional form with the vdW functional approach [187, 145].

The geometry optimization was performed by means of Broyden-Fletcher-Goldfarb-Shanno (BFGS) algorithm [180] assuming that the equilibrium structure was found when the maximal atomic forces were smaller than 0.05 eV/Å.

In order to simulate the adsorption of adatom or cluster on 2D crystal surfaces we used the supercell approach with imposed periodic boundary condition within the crystal plane and open boundary conditions in the perpendicular direction with at least 8 Å of vacuum on each side of the surface. Equlibrium lattice constants of 2D crystals are calculated with PBE functional by fitting the total energy dependence on lattice constant to the Birch-Murnaghan equation of state [188, 189, 190]. Sampling of the BZ are done according to the Monkhorst-Pack scheme [47], using $n_x \times n_y \times 1$ grid. The convergence of relevant physical quantities such as atomic positions, binding energies, spin magnetic moments, charge transfer etc. with the number of k-points were tested for each structure before the final choice of k-grid was made. The k-grid used for the self-consistent total energy calculations and structure optimization was refined when DOS or electronic bands are calculated.

The first-principles computation of realistic materials' properties in the supercell approach is numerically demanding due to a large number of atoms in the unit cell. Hence, access to high-performance computing (HPC) facilities is essential. Fulfilling these requirements, we appreciated the HPC resources of BESKOW supercomputer at The PDC Center for High Performance Computing of the KTH Royal Institute of Technology in Sweden, of ARCHER supercomputer of the UK National Supercomputing Service, United Kingdom, and of the PARADOX-IV supercomputer at the Scientific Computing Laboratory of the Institute of Physics in Belgrade, Serbia.

Bibliography

[1] K. S. Novoselov, A. K. Geim, S. V. Morozov, D. Jiang, Y. Zhang, S. V. Dubonos, et al., Electric field effect in atomically thin carbon films, *Science*, **306**, 5696 (2004).

[2] A. K. Geim and I. V. Grigorieva, Van der Waals heterostructures, *Nature* **499**, 419 (2013).

[3] G. E. Moore, Cramming more components onto integrated circuits, *IEEE Solid-State Circuits Society Newsletter* **11**, 33–35 (2006). (reprinted from Electronics **38**, 8 (1965))

[4] K. S. Kim, Y. Zhao, H. Jang, S. Y. Lee, J. M. Kim, K. S. Kim, et al., Large-scale pattern growth of graphene films for stretchable transparent electrodes, *Nature* **457**, 706 (2009).

[5] M. Bernardi, M. Palummo, and J. C. Grossman, Extraordinary sunlight absorption and one nanometer thick photovoltaics using two-dimensional monolayer materials, *Nano Lett.* **13**, 3664–3670 (2013).

[6] J. M. B. Lopes dos Santos, N. M. R. Peres, and A. H. Castro Neto, Graphene bilayer with a twist: electronic structure, *Phys. Rev. Lett.* **99**, 256802 (2007).

[7] V. M. Pereira and A. H. Castro Neto, Strain engineering of graphene's electronic structure, *Phys. Rev. Lett.* **103**, 046801 (2009).

[8] K.-A. N. Duerloo, Y. Li, and E. J. Reed, Structural phase transitions in two-dimensional Mo- and W-dichalcogenide monolayers, *Nat. Commun.* **5**, 4214 (2014).

[9] P. Hohenberg and W. Kohn, Inhomogeneous electron gas, *Phys. Rev* **136**, B864–B871 (1964).

[10] W. Kohn and L. J. Sham, Self-consistent equations including exchange and correlation effects, *Phys. Rev.* **140**, A1133–A1138 (1965).

[11] J. Kang, W. Liu, D. Sarkar, D. Jena, and K. Banerjee, Computational study of metal contacts to monolayer transition-metal dichalcogenide semiconductors, *Phys. Rev. X* **4**, 031005 (2014).

[12] Y. Xu, C. Cheng, S. Du, J. Yang, B. Yu, J. Luo, et al., Contacts between two- and three-dimensional materials: ohmic, Schottky, and p-n heterojunctions, *ACS Nano* **10**, 4895–4919 (2016).

[13] B. Radisavljević, A. Radenović, J. Brivio, V. Giacometti, and A. Kis, Single-layer MoS_2 transistors, *Nat. Nanotech.* **6**, 147 (2011).

[14] A. N. Enyashin, L. Yadgarov, L. Houben, I. Popov, M. Weidenbach, R. Tenne, et al., New route for stabilization of 1T-WS_2 and MoS_2 phases, *J. Phys. Chem. C* **115**, 24586–24591 (2011).

[15] G. Gao, Y. Jiao, F. Ma, Y. Jiao, E. Waclawik, and A. Du, Charge mediated semiconducting-to-metallic phase transition in molybdenum disulfide monolayer and hydrogen evolution reaction in new 1T' phase, *J. Phys. Chem. C* **119**, 13124–13128 (2015).

[16] P. E. Blöchl, C. J. Först, and J. Schimpl, The projector augmented-wave method: ab-initio molecular dynamics with full wave functions, *Bull. Mater. Sci.* **26**, 33–41 (2003).

[17] J. Enkovaara et al., Electronic structure calculations with GPAW: a real-space implementation of the projector augmented-wave method, *J. Phys. Condens. Matter* **22**, 253202 (2010).

[18] M. Born and K. Huang, *Dynamical Theory of Crystal Lattices* (Oxford: Oxford University Press, 1954).

[19] G. Wannier, Dynamics of band electrons in electric and magnetic fields, *Rev. Mod. Phys.* **34**, 645 (1962).

[20] G. Nenciu, Dynamics of band electrons in electric and magnetic fields: rigorous justification of the effective hamiltonians, *Rev. Mod. Phys.* **63**, 91 (1991).

[21] D. R. Hartree, The wave mechanics of an atom with non-Coulombic central field: parts I, II, III, *Proc. Cambridge Phil. Soc.* **24**, 89,111,426 (1928).

[22] V. Fock, Näherungsmethode zur Lösung des quantenmechanischen Mehrkörperproblems, *Z. Phys.* **61**, 126 (1930).

[23] J. C. Slater, A simplification of the Hartree-Fock method, *Phys. Rev.* **81**, 385–390 (1951).

[24] I. N. Levine, *Quantum Chemistry* (Upper Saddle River, New Jersey: Prentice-Hall, 2000).

[25] R. M. Martin, *Electronic structure : basic theory and practical methods* (Cambridge, New York: Cambridge University Press, 2004).

[26] L. H. Thomas, Inhomogeneous electron gas, *Proc. Cambridge Phil. Roy. Soc.* **23**, 542–548 (1927).

[27] E. Fermi, Un metodo statistico per la determinazione di alcune priorieta dell'atome, *Rend. Accad. Naz. Lincei* **6**, 602–607 (1927).

[28] R. M. Dreizler and E. K. U. Gross, *Density Functional Theory* (Berlin: Springer Verlag, 1990).

[29] M. Levy, Universal variational functionals of electron densities, first-order density matrices, and natural spin-orbitals and solution of the V-representability problem, *Proc. Natl. Acad. Sci. U.S.A.* **76**, 6062–6065 (1979).

[30] C. Fiolhais, F. Nogueira, and M. Marques, *A Primer in Density Functional Theory* (Berlin: Springer, 2003).

[31] W. Koch and M. C. Holthausen, *A Chemists' Guide to Density Functional Theory* (Weinheim: Wiley-VCH, 2001).

[32] V. Magnasco, Chapter 16 – Post-Hartree-Fock methods, in *Elementary Molecular Quantum Mechanics (Second Edition)*, 681–722 (V. Magnasco, ed., Oxford: Elsevier, second edn., 2013).

[33] N. W. Ashcroft and N. D. Mermin, *Solid State Physics* (Philadelphia: Saunders College, 1976).

[34] E. P. Wigner, On the interaction of electrons in metals, *Phys. Rev.* **46**, 1002–1011 (1934).

[35] M. Gell-Mann and K. A. Brueckner, Correlation energy of an electron gas at high-density, *Phys. Rev.* **106**, 364 (1957).

[36] J. P. Perdew and A. Zunger, Self-interaction correction to density-functional approximations for many-electron systems, *Phys Rev. B* **23**, 5048 (1981).

[37] D. M. Ceperley and B. J. Alder, Ground state of the electron gas by a stochastic method, *Phys. Rev. Lett.* **45**, 566–569 (1980).

[38] F. Herman, J. P. Van Dyke, and I. B. Ortenburger, Improved statistical exchange approximation for inhomogeneous many-electron systems, *Phys. Rev. Lett.* **22**, 807–811 (1969).

[39] P. S. Svendsen and U. von Barth, Gradient expansion of the exchange energy from second-order density response theory, *Phys. Rev. B* **54**, 17402–17413 (1996).

[40] J. P. Perdew and K. Burke, Comparison shopping for a gradient-corrected density functional, *Int. J. Quant. Chem.* **57**, 309–319 (1996).

[41] J. P. Perdew, K. Burke, and M. Ernzerhof, Generalized gradient approximation made simple, *Phys. Rev. Lett.* **77**, 3865–3868 (1996).

[42] F. Bloch, Über die Quantenmechanik der Elektronen in Kristallgittern, *Z. Phys.* **52**, 555 (1928).

[43] M. Tinkham, *Group Theory and Quantum Mechanics* (Dover Books on Chemistry and Earth Sciences, Dover Publications, 2003).

[44] C. Bradley and A. Cracknell, *The Mathematical Theory of Symmetry in Solids: Representation Theory for Point Groups and Space Groups.* (EBSCO ebook academic collection, OUP Oxford, 2010).

[45] R. A. Evarestov and V. P. Smirnov, Special points of the brillouin zone and their use in the solid state theory, *Physica Status Solidi (B)* **119**, 9–40 (1983).

[46] A. Baldereschi, Mean-value point in the Brillouin zone, *Phys. Rev. B* **7**, 5212–5215 (1973).

[47] H. J. Monkhorst and J. D. Pack, Special points for Brillouin-zone integrations, *Phys. Rev. B* **13**, 5188–5192 (1976).

[48] G. Gilat, Methods of Brillouin zone integration, *Methods Comput. Phys.* **15**, 317–70 (1976).

[49] L. Kleinman, Error in the tetrahedron integration scheme, *Phys. Rev. B* **28**, 1139–1141 (1983).

[50] O. Jepsen and O. K. Andersen, No error in the tetrahedron integration scheme, *Phys. Rev. B* **29**, 5965–5965 (1984).

[51] P. E. Blöchl, O. Jepsen, and O. K. Andersen, Improved tetrahedron method for Brillouin-zone integrations, *Phys. Rev. B* **49**, 16223–16233 (1994).

[52] C. G. Broyden, A class of methods for solving nonlinear simulataneous equations, *Math. Comput.* **19**, 577–593 (1965).

[53] P. Bendt and A. Zunger, New approach for solving the density-functional self-consistent-field problem, *Phys. Rev. B* **26**, 3114–3137 (1982).

[54] G. P. Srivastava, Broyden's method for self-consistent field convergence acceleration, *J. Phys. A* **17**, L317 (1984).

[55] K. Lejaeghere, G. Bihlmayer, T. Björkman, P. Blaha, S. Blügel, V. Blum, et al., Reproducibility in density functional theory calculations of solids, *Science* **351**, 6280 (2016).

[56] J. C. Slater, Wave function in a periodic potential, *Phys. Rev.* **51**, 846–851 (1937).

[57] J. Korringa, On the calculation of the energy of a Bloch wave in a metal, *Physica* **13**, 392 (1947).

[58] W. Kohn and N. Rostocker, Solution of the Schrödinger equation in periodic lattices with an application to metallic lithium, *Phys. Rev.* **94**, 1111 (1954).

[59] O. K. Andersen, Comments on the KKR wavefunctions: extension of the spherical exapansion beyound the mufffin tins, in *Computational Methods in Band Theory*, p. 178 (P. M. Marcus, J. F. Janak, and A. R. Williams, eds., New York: Plenum, 1971).

[60] O. K. Andersen, Linear methods in band theory, *Phys. Rev. B* **12**, 3060–3083 (1975).

[61] D. R. Hamann, M. Schlüter, and C. Chiang, Norm-conserving pseudopotentials, *Phys. Rev. Lett.* **43**, 1494–1497 (1979).

[62] M. T. Yin and M. L. Cohen, Theory of static structural properties, crystal stability, and phase transformations: Application to Si and Ge, *Phys. Rev. B* **26**, 5668–5687 (1982).

[63] P. E. Blöchl, Projector augmented-wave method, *Phys. Rev. B* **50**, 17953–17979 (1994).

[64] G. Kresse and D. Joubert, From ultrasoft pseudopotentials to the projector augmented-wave method, *Phys. Rev. B* **59**, 1758–1775 (1999).

[65] P. E. Blöchl, J. Kästner, and C. J. Först, *Electronic Structure Methods: Augmented Waves, Pseudopotentials and The Projector Augmented Wave Method*, pp. 93–119 (Dordrecht: Springer Netherlands, 2005).

[66] C. Rostgaard, The projector augmented-wave method, *arXiv:0910.1921* (2009).

[67] P. P. Ewald, Die Berechnung optischer und electrostatischer Gitterpotentiale, *Ann.der Physik* **64**, 253 (1921).

[68] M. Marsman and G. Kresse, Relaxed core projector-augmented-wave method, *The Journal of Chemical Physics* **125**, 104101 (2006).

[69] D. Vanderbilt, Soft self-consistent pseudopotentials in a generalized eigenvalue formalism, *Phys. Rev. B* **41**, 7892 (1990).

[70] S. C. Watson and E. A. Carter, Spin-dependent pseudopotentials, *Phys. Rev. B* **58**, R13309–R13313 (1998).

[71] C. G. Van de Walle and P. E. Blöchl, First-principles calculations of hyperfine parameters, *Phys. Rev. B* **47**, 4244–4255 (1993).

[72] N. Mounet, M. Gibertini, P. Schwaller, D. Campi, A. Merkys, A. Marrazzo, et al., Two-dimensional materials from high-throughput computational exfoliation of experimentally known compounds, *Nat. Nanotechnol.* **13**, 246–252 (2018).

[73] K. F. Mak, C. Lee, J. Hone, J. Shan, and T. F. Heinz, Atomically thin MoS_2: A new direct-gap semiconductor, *Phys. Rev. Lett.* **105**, 136805 (2010).

[74] A. Castellanos-Gomez, L. Vicarelli, E. Prada, J. O. Island, K. L. Narasimha-Acharya, S. I. Blanter, et al., Isolation and characterization of few-layer black phosphorus, *2D Mater.* **1**, 025001 (2014).

[75] H. J. Conley, B. Wang, J. I. Ziegler, R. F. Haglund, S. T. Pantelides, and K. I. Bolotin, Bandgap engineering of strained monolayer and bilayer MoS_2, *Nano Lett.* **13**, 3626–3630 (2013).

[76] A. S. Rodin, A. Carvalho, and A. H. Castro Neto, Strain-induced gap modification in black phosphorus, *Phys. Rev. Lett.* **112**, 176801 (2014).

[77] H. L. Zhuang, M. D. Johannes, A. K. Singh, and R. G. Hennig, Doping-controlled phase transitions in single-layer MoS_2, *Phys. Rev. B* **96**, 165305 (2017).

[78] A. H. Castro Neto, F. Guinea, N. M. R. Peres, K. S. Novoselov, and A. K. Geim, The electronic properties of graphene, *Rev. Mod. Phys.* **81**, 109–162 (2009).

[79] H. Boehm, A. Clauss, G. Fischer, and U. Hofmann, Dünnste kohlenstoff-folien, *Z. Naturforschg.* **17b**, 150–153 (1962).

[80] N. Mermin, Crystalline order in two dimensions, *Phys. Rev.* **176**, 250–254 (1968).

[81] E. McCann, *Electronic properties of monolayer and bilayer graphene*, in Graphene Nanoelectronics, NanoScience and Technology, pp. 237–275 (Raza H. ed., Springer, Berlin, Heidelberg Nano Science and Technology, 2012)

[82] C. Lee, X. Wei, J. W. Kysar, and J. Hone, Measurement of the elastic properties and intrinsic strength of monolayer graphene, *Science* **321**, 385–388 (2008).

[83] T. Ando, T. Nakanishi, and R. Saito, Berry's phase and absence of back scattering in carbon nanotubes, *J. Phys. Soc. Jpn.* **67**, 2857–2862 (1998).

[84] J.-N. Fuchs, Dirac fermions in graphene and analogues: magnetic field and topological properties, *arxiv:1306.0380* (2013).

[85] R. Saito, G. Dresselhaus, and M. S. Dresselhaus, *Physical properties of carbon nanotubes* (Imperial College Press, 1998).

[86] S. J. Brun and M. R. Thomsen, *Electronic and optical properties of graphene and graphene antidot structures*, (Master's thesis, Aalborg University, 2013).

[87] M. Kuisma, J. Ojanen, J. Enkovaara, and T. T. Rantala, Kohn-Sham potential with discontinuity for band gap materials, *Phys. Rev. B* **82**, 115106 (2010).

[88] P. Miró, M. Audiffred, and T. Heine, An atlas of two-dimensional materials, *Chem. Soc. Rev.* **43**, 6537–6554 (2014).

[89] J. P. Perdew, Density functional theory and the band gap problem, *Int. J. Quantum Chem.* **28**, 497–523 (1985).

[90] M. Staedele, M. Moukara, J. A. Majewski, P. Vogl, and A. Gorling, Exact exchange Kohn-Sham formalism applied to semiconductors, *Phys. Rev. B* **59**, 10031–10043 (1999).

[91] C. R. Dean, L. Wang, P. Maher, C. Forsythe, F. Ghahari, Y. Gao, et al., Hofstadter's butterfly and the fractal quantum hall effect in moiré superlattices, *Nature* **497**, 598 (2013).

[92] P. W. Bridgman, Two new modification of phosphorus, *J. Am. Chem. Soc.* **36**, 1344–1363 (1914).

[93] R. W. Keyes, The electrical properties of black phosphorus, *Phys. Rev.* **92**, 580–584 (1953).

[94] L. Li, Y. Yu, G. J. Ye, Q. Ge, X. Ou, H. Wu, et al., Black phosphorus field-effect transistors, *Nat. Nanotechnol.* **9**, 372 (2014).

[95] H. Liu, A. T. Neal, Z. Zhu, Z. Luo, X. Xu, D. Tománek, et al., Phosphorene: An unexplored 2D semiconductor with a high hole mobility, *ACS Nano* **8**, 4033–4041 (2014).

[96] S. Das, W. Zhang, M. Demarteau, A. Hoffmann, M. Dubey, and A. Roelofs, Tunable transport gap in phosphorene, *Nano Lett.* **14**, 5733–5739 (2014).

[97] V. Tran, R. Soklaski, Y. Liang, and L. Yang, Layer-controlled band gap and anisotropic excitons in few-layer black phosphorus, *Phys. Rev. B* **89**, 235319 (2014).

[98] P. Chen, N. Li, X. Chen, W.-J. Ong, and X. Zhao, The rising star of 2D black phosphorus beyond graphene: synthesis, properties and electronic applications, *2D Mater.* **5**, 014002 (2017).

[99] A. A. Kistanov, Y. Cai, K. Zhou, S. V. Dmitriev, and Y.-W. Zhang, Large electronic anisotropy and enhanced chemical activity of highly rippled phosphorene, *J. Phys. Chem. C* **120**, 6876–6884 (2016).

[100] H. Şahin, S. Cahangirov, M. Topsakal, E. Bekaroglu, E. Akturk, R. T. Senger, et al., Monolayer honeycomb structures of group-IV elements and III-V binary compounds: First-principles calculations, *Phys. Rev. B* **80**, 155453 (2009).

[101] T.-Y. Lü, X.-X. Liao, H.-Q. Wang, and J.-C. Zheng, Tuning the indirect–direct band gap transition of SiC, GeC and SnC monolayer in a graphene-like hon-

eycomb structure by strain engineering: a quasiparticle GW study, *J. Mater. Chem.* **22**, 10062–10068 (2012).

[102] T. Susi, V. Skákalová, A. Mittelberger, P. Kotrusz, M. Hulman, T. J. Pennycook, et al., Computational insights and the observation of SiC nanograin assembly: towards 2D silicon carbide, *Sci. Rep.* **7**, 4399 (2017).

[103] R. G. Dickinson and L. Pauling, The crystal structure of molybdenite, *J. Am. Chem. Soc.* **45**, 1466–1471 (1923).

[104] J. Wilson and A. Yoffe, The transition metal dichalcogenides discussion and interpretation of the observed optical, electrical and structural properties, *Adv. Phys.* **18**, 193–335 (1969).

[105] S. Manzeli, D. Ovchinnikov, D. Pasquier, O. V. Yazyev, and A. Kis, 2D transition metal dichalcogenides, *Nat. Rev. Mater.* **2**, 17033 (2017).

[106] M. Chhowalla, H. S. Shin, G. Eda, L.-J. Li, K. P. Loh, and H. Zhang, The chemistry of two-dimensional layered transition metal dichalcogenide nanosheets, *Nat. Chem.* **5**, 263 (2013).

[107] R. Gordon, D. Yang, E. D. Crozier, D.-T. Jiang, and R. F. Frindt, Structures of exfoliated single layers of WS_2, MoS_2, and $MoSe_2$ in aqueous suspension, *Phys. Rev. B* **65**, 125407 (2002).

[108] B. Sipos, A. F. Kusmartseva, A. Akrap, H. Berger, L. Forró, and E. Tutis, From Mott state to superconductivity in 1T-TaS_2, *Nat. Mater.* **7**, 960 (2008).

[109] K. Rossnagel, On the origin of charge-density waves in select layered transition-metal dichalcogenides, *J. Phys. Condens. Matter* **23**, 213001 (2011).

[110] A. Kuc, N. Zibouche, and T. Heine, Influence of quantum confinement on the electronic structure of the transition metal sulfide TS_2, *Phys. Rev. B* **83**, 245213 (2011).

[111] T. Cao, G. Wang, W. Han, H. Ye, C. Zhu, J. Shi, et al., Valley-selective circular dichroism of monolayer molybdenum disulphide, *Nat. Commun.* **3,** 887 (2012).

[112] H. Zeng, J. Dai, W. Yao, D. Xiao, and X. Cui, Valley polarization in MoS_2 monolayers by optical pumping, *Nat. Nanotechnol.* **7**, 490 (2012).

[113] K. F. Mak, K. He, J. Shan, and T. F. Heinz, Control of valley polarization in monolayer MoS_2 by optical helicity, *Nat. Nanotechnol.* **7**, 494 (2012).

[114] M. Kertesz and R. Hoffmann, Octahedral vs. trigonal-prismatic coordination and clustering in transition-metal dichalcogenides, *J. Am. Chem. Soc.* **106**, 3453–3460 (1984).

[115] F. A. Rasmussen and K. S. Thygesen, Computational 2D materials database: Electronic structure of transition-metal dichalcogenides and oxides, *J. Phys. Chem. C* **119**, 13169–13183 (2015).

[116] R. Bissessur, M. G. Kanatzidis, J. L. Schindler, and C. R. Kannewurf, Encapsulation of polymers into mos2 and metal to insulator transition in metastable MoS_2, *J. Chem. Soc., Chem. Commun.*, 1582–1585 (1993).

[117] G. Eda, H. Yamaguchi, D. Voiry, T. Fujita, M. Chen, and M. Chhowalla, Photoluminescence from chemically exfoliated MoS_2, *Nano Lett.* **11**, 5111–5116 (2011).

[118] G. Eda, T. Fujita, H. Yamaguchi, D. Voiry, M. Chen, and M. Chhowalla, Coherent atomic and electronic heterostructures of single-layer MoS_2, *ACS Nano* **6**, 7311–7317 (2012).

[119] P. Ganal, W. Olberding, T. Butz, and G. Ouvrard, Soft chemistry induced host metal coordination change from octahedral to trigonal prismatic in 1T-TaS_2, *Solid State Ion.* **59**, 313–319 (1993).

[120] J. Wilson, F. D. Salvo, and S. Mahajan, Charge-density waves and superlattices in the metallic layered transition metal dichalcogenides, *Adv. Phys.* **24**, 117–201 (1975).

[121] A. H. Castro Neto, Charge density wave, superconductivity, and anomalous metallic behavior in 2D transition metal dichalcogenides, *Phys. Rev. Lett.* **86**, 4382–4385 (2001).

[122] J. Heising and M. G. Kanatzidis, Exfoliated and restacked MoS_2 and WS_2: Ionic or neutral species? Encapsulation and ordering of hard electropositive cations, *J. Am. Chem. Soc.* **121**, 11720–11732 (1999).

[123] A. Splendiani, L. Sun, Y. Zhang, T. Li, J. Kim, C.-Y. Chim, et al., Emerging photoluminescence in monolayer MoS_2, *Nano Lett.* **10**, 1271–1275 (2010).

[124] H. M. Hill, A. F. Rigosi, K. T. Rim, G. W. Flynn, and T. F. Heinz, Band alignment in MoS_2/WS_2 transition metal dichalcogenide heterostructures probed by scanning tunneling microscopy and spectroscopy, *Nano Lett.* **16**, 4831–4837 (2016).

[125] F. Xia, V. Perebeinos, Y.-m. Lin, Y. Wu, and P. Avouris, The origins and limits of metal-graphene junction resistance, *Nat. Nanotechnol.* **6**, 179 (2011).

[126] Z. Zhou, F. Gao, and D. W. Goodman, Deposition of metal clusters on single-layer graphene/Ru(0001): Factors that govern cluster growth, *Surf. Sci.* **604**, L31–L38 (2010).

[127] L. Schlapbach and A. Züttel, Hydrogen-storage materials for mobile applications, *Nature* **414**, 353–358 (2001).

[128] T. Yildirim and S. Ciraci, Titanium-decorated carbon nanotubes as a potential high-capacity hydrogen storage medium, *Phys. Rev. Lett.* **94**, 175501 (2005).

[129] T. Yildirim, J. Íñiguez, and S. Ciraci, Molecular and dissociative adsorption of multiple hydrogen molecules on transition metal decorated C_{60}, *Phys. Rev. B* **72**, p. 153403, Oct 2005.

[130] Z. M. Ao, Q. Jiang, R. Q. Zhang, T. T. Tan, and S. Li, Al doped graphene: A promising material for hydrogen storage at room temperature, *J. Appl. Phys.* **105**, 074307 (2009).

[131] Q. Sun, Q. Wang, P. Jena, and Y. Kawazoe, Clustering of Ti on a C_{60} surface and its effect on hydrogen storage, *J. Am. Chem. Soc.* **127**, 14582–14583 (2005).

[132] P. Krasnov, F. Ding, A. Singh, and B. I. Yakobson, Clustering of Sv on SWNT and reduction of hydrogen uptake: Ab-initio all-electron calculations, *J. Phys. Chem. C* **111**, 11 (2007).

[133] K. T. Chan, J. B. Neaton, and M. L. Cohen, First-principles study of metal adatom adsorption on graphene, *Phys. Rev. B* **77**, 235430 (2008).

[134] A. Pulido, M. Boronat, and A. Corma, Theoretical investigation of gold clusters supported on graphene sheets, *New J. Chem.* **35**, 2153–2161 (2011).

[135] M. Caragiu and S. Finberg, Alkali metal adsorption on graphite: a review, *J. Phys. Condens. Matter* **17**, R995–R1024 (2005).

[136] R. Bader, *Atoms in Molecules: A Quantum Theory* (International series of monographs on chemistry, Clarendon Press, 1990).

[137] R. Zan, U. Bangert, Q. Ramasse, and K. S. Novoselov, Metal-graphene interaction studied via atomic resolution scanning transmission electron microscopy, *Nano Lett.* **11**, 1087–1092 (2011).

[138] H. Lee, J. Ihm, M. L. Cohen, and S. G. Louie, Calcium-decorated graphene-based nanostructures for hydrogen storage, *Nano Lett.* **10**, 793–798 (2010).

[139] C. Cazorla, S. A. Shevlin, and Z. X. Guo, First-principles study of the stability of calcium-decorated carbon nanostructures, *Phys. Rev. B* **82**, 155454 (2010).

[140] M. Khantha, N. A. Cordero, L. M. Molina, J. A. Alonso, and L. A. Girifalco, Interaction of lithium with graphene: An ab initio study, *Phys. Rev. B* **70**, 125422 (2004).

[141] A. M. Garay-Tapia, A. H. Romero, and V. Barone, Lithium adsorption on graphene: From isolated adatoms to metallic sheets, *J. Chem. Theory Comput.* **8**, 1064–1071 (2012).

[142] M. Liu, A. Kutana, Y. Liu, and B. I. Yakobson, First-principles studies of Li nucleation on graphene, *J. Phys. Chem. Lett.* **5**,1 1225–1229 (2014).

[143] S. Stavrić, Density functional theory study of adsorption of metals on graphene (Master's thesis, University of Belgrade, Faculty of Physics, 2014).

[144] R. Xiao, D. Fritsch, M. D. Kuz'min, K. Koepernik, H. Eschrig, M. Richter, et al., Co dimers on hexagonal carbon rings proposed as subnanometer magnetic storage bits, *Phys. Rev. Lett.* **103**, 187201 (2009).

[145] J. Klimeš, D. R. Bowler, and A. Michaelides, Chemical accuracy for the van der Waals density functional, *J. Phys. Cond. Matter* **22**, 022201 (2009).

[146] S. P. Koenig, N. G. Boddeti, M. L. Dunn, and J. S. Bunch, Ultrastrong adhesion of graphene membranes, *Nat. Nanotechnol.* **6**, 543 (2011).

[147] X. Li, J. Wu, N. Mao, J. Zhang, Z. Lei, Z. Liu, et al., A self-powered graphene-MoS_2 hybrid phototransistor with fast response rate and high on–off ratio, *Carbon* **92**, 126–132 (2015).

[148] W. J. Yu, Y. Liu, H. Zhou, A. Yin, Z. Li, Y. Huang, et al., Highly efficient gate-tunable photocurrent generation in vertical heterostructures of layered materials, *Nat. Nanotechnol.* **8**, 952 (2013).

[149] K. Chang, W. Chen, L. Ma, H. Li, H. Li, F. Huang, et al., Graphene-like MoS_2/amorphous carbon composites with high capacity and excellent stability as anode materials for lithium ion batteries," *J. Mater. Chem.* **21**, 6251–6257 (2011).

[150] Q. Sun, Y. Dai, Y. Ma, T. Jing, W. Wei, and B. Huang, Ab initio prediction and characterization of Mo_2C monolayer as anodes for lithium-ion and sodium-ion batteries, *J. Phys. Chem. Lett.* **7**, 937–943 (2016).

[151] S. Stavrić, Z. S. Popović, and Ž. Šljivančanin, Understanding trends in lithium binding at two-dimensional materials, *Phys. Rev. Mater.* **2**, 114007 (2018).

[152] Y. Xie, M. Naguib, V. N. Mochalin, M. W. Barsoum, Y. Gogotsi, X. Yu, et al., Role of surface structure on Li-ion energy storage capacity of two-dimensional transition-metal carbides, *J. Am. Chem. Soc.* **136**, 6385–6394 (2014).

[153] Q.-F. Li, C.-G. Duan, X. G. Wan, and J.-L. Kuo, Theoretical prediction of anode materials in Li-ion batteries on layered black and blue phosphorus, *J. Phys. Chem. C* **119**, 8662–8670 (2015).

[154] T. Hu and J. Hong, First-principles study of metal adatom adsorption on black phosphorene, *J. Phys. Chem. C* **119**, 8199–8207 (2015).

[155] Y. Ding and Y. Wang, Structural, electronic, and magnetic properties of adatom adsorptions on black and blue phosphorene: A first-principles study, *J. Phys. Chem. C* **119**, 10610–10622 (2015).

[156] R. J. Baierle, C. J. Rupp, and J. Anversa, Alkali (Li, K and Na) and alkali-earth (Be, Ca and Mg) adatoms on SiC single layer, *Appl. Surf. Sci.* **435**, 338–345 (2018).

[157] Y. Zhou and C. Geng, A MoO_2 sheet as a promising electrode material: ultrafast Li-diffusion and astonishing Li-storage capacity, *Nanotechnology* **28**, 105402 (2017).

[158] C. C. Leong, H. Pan, and S. K. Ho, Two-dimensional transition-metal oxide monolayers as cathode materials for Li and Na ion batteries, *Phys. Chem. Chem. Phys.* **18**, 7527–7534 (2016).

[159] W. A. Saidi, Trends in the adsorption and growth morphology of metals on the MoS_2(001) surface, *Cryst. Growth Des.* **15**, 3190–3200 (2015).

[160] D. Nasr Esfahani, O. Leenaerts, H. Sahin, B. Partoens, and F. M. Peeters, Structural transitions in monolayer MoS_2 by lithium adsorption, *J. Phys. Chem. C* **119**, 10602–10609 (2015).

[161] Ž. Šljivančanin and M. Belić, Graphene/MoS_2 heterostructures as templates for growing two-dimensional metals: Predictions from ab initio calculations, *Phys. Rev. Materials* **1**, 044003 (2017).

[162] A. K. Geim and K. S. Novoselov, The rise of graphene, *Nat. Mater* **6**, 183 (2007).

[163] K. Bolotin, K. Sikes, Z. Jiang, M. Klima, G. Fudenberg, J. Hone, et al., Ultrahigh electron mobility in suspended graphene, *Solid State Commun.* **146**, 351–355 (2008).

[164] Y. B. Z. M. Y. Han, B. Ozyilmaz and P. Kim, Energy band gap engineering of graphene nanoribbons, *Phys. Rev. Lett.* **98**, 206805 (2007).

[165] X. Li, X. Wang, L. Zhang, S. Lee, and H. Dai, Chemically derived, ultrasmooth graphene nanoribbon semiconductors, *Science* **319**, 1229–1232 (2008).

[166] F. Xia, D. B. Farmer, Y.-m. Lin, and P. Avouris, Graphene field-effect transistors with high on/off current ratio and large transport band gap at room temperature, *Nano Lett.* **10**, 715–718 (2010).

[167] S. Lebègue and O. Eriksson, Electronic structure of two-dimensional crystals from ab initio theory, *Phys. Rev. B* **79**, 115409 (2009).

[168] K. S. Novoselov, D. Jiang, F. Schedin, T. J. Booth, V. V. Khotkevich, S. V. Morozov, and A. K. Geim, Two-dimensional atomic crystals, *Proc. Natl. Acad. Sci. U.S.A.* **102**, 10451–10453 (2005).

[169] S. Ghatak, A. N. Pal, and A. Ghosh, Nature of electronic states in atomically thin MoS_2 field-effect transistors, *ACS Nano* **5**, 7707–7712 (2011).

[170] A. L. Efros, F. G. Pikus, and G. G. Samsonidze, Maximum low-temperature mobility of two-dimensional electrons in heterojunctions with a thick spacer layer, *Phys. Rev. B* **41**, 8295–8301 (1990).

[171] B. Radisavljević and A. Kis, Mobility engineering and a metal-insulator transition in monolayer MoS_2, *Nat. Mater.* **12**, 815 (2013).

[172] N. F. Mott, *Metal-insulator transitions* (Taylor Francis, Barnes Noble Books London, New York, 1974).

[173] A. Punnoose and A. M. Finkel'stein, Metal-insulator transition in disordered two-dimensional electron systems, *Science* **310**, 289–291 (2005).

[174] S. Bertolazzi, J. Brivio, and A. Kis, Stretching and breaking of ultrathin MoS_2, *ACS Nano* **5**, 9703–9709 (2011).

[175] Y.-C. Lin, D. O. Dumcenco, Y.-S. Huang, and K. Suenaga, Atomic mechanism of the semiconducting-to-metallic phase transition in single-layered MoS_2, *Nat. Nanotechnol.* **9**, 391 (2014).

[176] H.-P. Komsa, J. Kotakoski, S. Kurasch, O. Lehtinen, U. Kaiser, and A. V. Krasheninnikov, Two-dimensional transition metal dichalcogenides under electron irradiation: Defect production and doping, *Phys. Rev. Lett.* **109**, 035503 (2012).

[177] M. Kan, J. Y. Wang, X. W. Li, S. H. Zhang, Y. W. Li, Y. Kawazoe, et al., Structures and phase transition of a MoS_2 monolayer, *J. Phys. Chem. C* **118**, 1515–1522 (2014).

[178] X. Wang, X. Shen, Z. Wang, R. Yu, and L. Chen, Atomic-scale clarification of structural transition of MoS_2 upon sodium intercalation, *ACS Nano* **8**, 11394–11400 (2014).

[179] L. Ci, L. Song, C. Jin, D. Jariwala, D. Wu, Y. Li, et al., Atomic layers of hybridized boron nitride and graphene domains, *Nat. Mater.* **9**, 430 (2010).

[180] D. C. Liu and J. Nocedal, On the limited memory BFGS method for large-scale optimization, *Math. Prog.* **45**, 503 (1989).

[181] G. Grosso and G. Parravicini, *Solid State Physics* (Elsevier Science, 2000).

[182] M. Born and J. R. Oppenheimer, Zur quantentheorie der molekeln, *Ann. Physik* **84**, 457 (1927).

[183] A. H. Larsen, J. J. Mortensen, J. Blomqvist, I. E Castelli, R. Christensen, M. Dułak, et al., The atomic simulation environment—a python library for working with atoms, *J. Phys. Condens. Matter* **29**, 273002 (2017).

[184] P. Pulay, Convergence acceleration of iterative sequences. the case of SCF iteration, *Chem. Phys. Lett.* **73**, 393–398 (1980).

[185] G. Kresse and J. Furthmüller, Efficient iterative schemes for ab initio total-energy calculations using a plane-wave basis set, *Phys. Rev. B* **54**, 11169–11186 (1996).

[186] J. Perdew, K. Burke, and M. Ernzerhof, Generalized gradient approximation made simple, *Phys. Rev. Lett.* **77**, 3865–3868 (1996).

[187] D. C. Langreth, B. I. Lundqvist, S. D. Chakarova-Käck, V. R. Cooper, M. Dion, P. Hyldgaard, et al., A density functional for sparse matter, *J. Phys. Condens. Matter* **21**, 084203 (2009).

[188] F. D. Murnaghan, The compressibility of media under extreme pressures *Proc. Natl. Acad. Sci. U.S.A.* **30**, 244–247 (1944).

[189] F. Birch, Finite elastic strain of cubic crystals, *Phys. Rev.* **71**, 809–824 (1947).

[190] M. Hebbache and M. Zemzemi, Ab initio study of high-pressure behavior of a low compressibility metal and a hard material: osmium and diamond, *Phys. Rev. B* **70**, 224107 (2004).

Biografija autora i lista publikacija

Srđan Stavrić je rođen 31.03.1990. godine u Zaječaru. Osnovnu školu "Desanka Maksimović" pohađao je i završio u rodnom gradu. Gimnaziju u Zaječaru, prirodno-matematički smer, završava 2009. godine kao nosilac Vukove diplome i đak generacije. Tokom osnovne i srednje škole pokazao je veliko interesovanje za fiziku iz koje se takmičio i osvojio brojne nagrade na republičkim i (tadašnjim) saveznim takmičenjima. Od drugog razreda gimnazije stipendista je "Fondacije za razvoj naučnog i umetničkog podmlatka" pri Ministarstvu za nauku.

Fizički fakultet Univerziteta u Beogradu, smer Teorijska i eksperimentalna fizika, upisuje 2009. godine. Diplomirao je septembra 2013. godine sa prosečnom ocenom 9,92/10,0 i iste godine upisao master studije Fizičkog fakulteta, smer Teorijska i eksperimentalna fizika. Ovaj stepen studija završava sa prosečnom ocenom 10,0 septembra 2014. godine, uspešno odbranivši master tezu pod nazivom *Ispitivanje adsorpcije metala na grafenu pomoću teorije funkcionala gustine* rađenu pod mentorstvom dr Željka Šljivančanina, naučnog savetnika Instituta za nuklearne nauke "Vinča" (INN "Vinča"). Za navedeni master rad autoru je Fizički fakultet dodelio nagradu "Prof. dr Ljubomir Ćirković" za najbolji master rad u akademskoj 2014/2015. godini. Tokom studija bio je stipendija grada Zaječara, a na završnoj godini osnovnih kao i tokom master studija stipendista fondacije "Dositeja" pri Ministarstvu omladine i sporta.

U periodu od marta 2014. do oktobra 2015. godine Srđan je bio zaposlen na Katedri za fiziku Rudarsko-geološkog fakulteta, najpre kao saradnik u nastavi a potom i kao asistent. U INN "Vinča" se zapošljava oktobra 2015. godine kao istraživač-pripravnik da bi 2017. godine bio izabran u zvanje istraživača-saradnika. U periodu 2014-2019. godine učestvovao je u nastavi na Fizičkom fakultetu na predmetima Laboratorija fizike 1 i 2, kao i u izvođenju računskih vežbi iz Teorije kondenzovanog stanja (kurs su predavali dr Mihajlo Vanević i dr Darko Tanasković).

Doktorske studije fizike na Fizičkom fakultetu, uža naučna oblast Fizika kondenzovane materije i statistička fizika, upisuje oktobra 2014. godine. Doktorsku tezu pod nazivom "First-principles study of the structural and electronic properties of metals adsorbed on two-dimensional materials" izrađuje u periodu 2014-2019. godine pod mentorstvom dr Željka Šljivančanina, naučnog savetnika INN "Vinča". Tokom ovog perioda svoj naučni rad koji se tiče strukturnih, elektronskih i magnetnih osobina nanostruktura metala adsorbovanih na dvodimenzionalnim materijalima, predstavlja na više konferencija i letnjih škola u Italiji, Španiji, Nemačkoj, Danskoj i Austriji. Po zaposlenju u INN "Vinča" angažovan je na projektu Ministarstva prosvete, nauke i tehnološkog razvoja pod nazivom *Elektronske, transportne i optičke osobine nanofaznih materijala* pod rukovodstvom dr Radomira Žikića sa Instituta za fiziku u Zemunu. Pored nacionalne saradnje, u periodu 2014-2017. godine Srđan je bio

angažovan na međunarodnom projektu *Growth, Characterization and Modeling of Magnetic Nanostructures at Surfaces* pod rukovodstvom prof. dr Haralda Bruna sa EPFL-a u Lozani. U okviru ovog projekta izučavane su magnetne nanostrukture obrazovane na dvodimenzionalnim materijalima i površinama kristala, koje se smatraju vrlo obećavajućim u konstrukciji nove generacije hard diskova sa znatno većim kapacitetom od postojećih. Projekat je finansiran od strane Švajcarske nacionalne naučne fondacije i predstavlja međunarodnu saradnju tri grupe – grupe profesora Bruna, grupe dr Željka Šljivančanina iz INN "Vinča" (čiji je autor član), kao i grupe dr Radomira Žikića sa Instituta za fiziku u Zemunu.

Lista publikacija

Srđan Stavrić je objavio četiri naučna članka u recenziranim međunarodnim časopisima, od kojih se dva (1. i 4. sa liste) tiču ove doktorske teze, a rezultati objavljeni u njima su u velikoj meri predstavljeni i u samoj tezi. Naučni članci su ovde navedeni hronološkim redosledom:

4. **S. Stavrić**, Z. S. Popović, and Ž. Šljivančanin, "Understanding trends in lithium binding at two-dimensional materials", *Phys. Rev. Materials* **2**, 114007, (2018).

3. A. Singha, F. Donati, F. D. Natterer, C. Wäckerlin, **S. Stavrić**, Z. S. Popović, Ž. Šljivančanin, F. Patthey, and H. Brune, "Spin excitations in a 4f–3d heterodimer on MgO", *Phys. Rev. Lett.* **121**, 257202 (2018).

2. E. Fernandes, F. Donati, F. Patthey, **S. Stavrić**, Ž. Šljivančanin, and H. Brune, "Adsorption sites of individual metal atoms on ultrathin MgO(100) films", *Phys. Rev. B* **96**, 045419, (2017).

1. **S. Stavrić**, M. Belić, and Ž. Šljivančanin, "Planar versus three-dimensional growth of metal nanostructures at graphene", *Carbon* **96** (2016), 216-222.

Прилог 1.

Изјава о ауторству

Име и презиме аутора **Срђан Ставрић**

Број индекса **8002/2014**

Изјављујем

да је докторска дисертација под насловом

First-principles study of the structural and electronic properties of metals adsorbed at two-dimensional materials

(**Ab initio *истраживање структурних и електронских особина метала адсорбованих на дводимензионалним материјалима***)

- резултат сопственог истраживачког рада;
- да предложена дисертација у целини ни у деловима није била предложена за добијање било које дипломе према студијским програмима других високошколских установа;
- да су резултати коректно наведени и
- да нисам кршио ауторска права и користио интелектуалну својину других лица.

Потпис аутора

У Београду, 16.09.2019.

Прилог 2.

Изјава о истоветности штампане и електронске верзије докторског рада

Име и презиме аутора **Срђан Ставрић**

Број индекса **8002/2014**

Студијски програм **Физика – Физика кондензоване материје**

Наслов рада ***First-principles study of the structural and electronic properties of metals adsorbed at two-dimensional materials*** (**Ab initio** ***истраживање структурних и електронских особина метала адсорбованих на дводимензионалним материјалима***)

Ментор **др Жељко Шљиванчанин**

Потписани **Срђан Ставрић**

Изјављујем да је штампана верзија мог докторског рада истоветна електронској верзији коју сам предао за објављивање на порталу **Дигиталног репозиторијума Универзитета у Београду.**

Дозвољавам да се објаве моји лични подаци везани за добијање академског звања доктора наука, као што су име и презиме, година и место рођења и датум одбране рада.

Ови лични подаци могу се објавити на мрежним страницама дигиталне библиотеке, у електронском каталогу и у публикацијама Универзитета у Београду.

Потпис докторанда

У Београду, 16.09.2019,

Прилог 3.

Изјава о коришћењу

Овлашћујем Универзитетску библиотеку „Светозар Марковић“ да у Дигитални репозиторијум Универзитета у Београду унесе моју докторску дисертацију под насловом:

First-principles study of the structural and electronic properties of metals adsorbed at two-dimensional materials (**Ab initio *истраживање структурних и електронских особина метала адсорбованих на дводимензионалним материјалима***)

која је моје ауторско дело.

Дисертацију са свим прилозима предао/ла сам у електронском формату погодном за трајно архивирање.

Моју докторску дисертацију похрањену у Дигитални репозиторијум Универзитета у Београду могу да користе сви који поштују одредбе садржане у одабраном типу лиценце Креативне заједнице (Creative Commons) за коју сам се одлучио/ла.

1. Ауторство

2. Ауторство - некомерцијално

3. Ауторство – некомерцијално – без прераде

4. Ауторство – некомерцијално – делити под истим условима

5. Ауторство – без прераде

6. Ауторство – делити под истим условима

(Молимо да заокружите само једну од шест понуђених лиценци, кратак опис лиценци дат је на полеђини листа).

Потпис докторанда

У Београду, 16.09.2019.

1. **Ауторство** - Дозвољавате умножавање, дистрибуцију и јавно саопштавање дела, и прераде, ако се наведе име аутора на начин одређен од стране аутора или даваоца лиценце, чак и у комерцијалне сврхе. Ово је најслободнија од свих лиценци.

2. **Ауторство – некомерцијално**. Дозвољавате умножавање, дистрибуцију и јавно саопштавање дела, и прераде, ако се наведе име аутора на начин одређен од стране аутора или даваоца лиценце. Ова лиценца не дозвољава комерцијалну употребу дела.

3. **Ауторство - некомерцијално** – без прераде. Дозвољавате умножавање, дистрибуцију и јавно саопштавање дела, без промена, преобликовања или употребе дела у свом делу, ако се наведе име аутора на начин одређен од стране аутора или даваоца лиценце. Ова лиценца не дозвољава комерцијалну употребу дела. У односу на све остале лиценце, овом лиценцом се ограничава највећи обим права коришћења дела.

4. **Ауторство - некомерцијално** – делити под истим условима. Дозвољавате умножавање, дистрибуцију и јавно саопштавање дела, и прераде, ако се наведе име аутора на начин одређен од стране аутора или даваоца лиценце и ако се прерада дистрибуира под истом или сличном лиценцом. Ова лиценца не дозвољава комерцијалну употребу дела и прерада.

5. **Ауторство – без прераде**. Дозвољавате умножавање, дистрибуцију и јавно саопштавање дела, без промена, преобликовања или употребе дела у свом делу, ако се наведе име аутора на начин одређен од стране аутора или даваоца лиценце. Ова лиценца дозвољава комерцијалну употребу дела.

6. **Ауторство - делити под истим условима**. Дозвољавате умножавање, дистрибуцију и јавно саопштавање дела, и прераде, ако се наведе име аутора на начин одређен од стране аутора или даваоца лиценце и ако се прерада дистрибуира под истом или сличном лиценцом. Ова лиценца дозвољава комерцијалну употребу дела и прерада. Слична је софтверским лиценцама, односно лиценцама отвореног кода.